TÉCNICO LISBOA

Characterization and Design of PV solar Cells that Absorb Ultraviolet, Visible and Infrared Light

Sara Manuel Nunes Bernardes

Thesis to obtain the Master of Science Degree in

Electrical and Computer Engineering

Supervisors: Prof. João Paulo Neto Torres
Prof. Carlos Alberto Ferreira Fernandes

Examination Committee

Chairperson: Prof. Francisco André Corrêa Alegria
Supervisor: Prof. João Paulo Neto Torres
Member of the Committee: Prof. Maria João Marques Martins

September 2020

To my Father, for the best pieces of life advice,
and to my Mother, for the copious amount of support and inspiration.

Declaration

I declare that this document is an original work of my own authorship and that it fulfills all the requirements of the Code of Conduct and Good Practices of the Universidade de Lisboa.

Acknowledgments

I would like to start by acknowledging both my supervisor professors, especially Prof. João Torres for his support, useful insight, and continuous reassuring. I also thank my colleagues for helping me writing this thesis, and for always having my back.

To the "AA" friend group, thank you for all the motivational, free of judgment, support and all the rants about our beloved university. I thank you all for making these long years as enjoyable as possible. I doubt I would still be a sane (questionable) person if we had not been together in the same boat. Proper respects for a special group of you: Sara, for always, always being there to put up with my rage fits, for enduring my stupidity and for always believing in me; Rita, for all the unexpected and unusual pep talks; Sofia, for organizing the best dinners and always being able to make me laugh with her way of living under a rock; Madalena, for all of your fellow nerdom and with whom I can have all of my fangirl moments without looking stupid; Carolina, for being my very first friend in college, your sacrifice will not be forgotten; Sebastião, for your merry-go-round personality and, of course, for making the best “petiscos”. To all of you that were not mentioned, know that was just because I could not conjure a catchy phrase to put next to your name. That, and I would run out of space.

To my hometown friends, I also thank you for your companionship, for being able to distract me with your stupidity when no one else could. I will not disclosure your names, otherwise, you would be embarrassed. For those of you who can read, know that you all are very much appreciated.

Last but not least, the final acknowledgments go to my family. To all my uncles, aunts and cousins, thank you for encouraging me. Ending with the most important people in my life: firstly, my grandparents, Olga and José, for their patience, and for always being there for me throughout all my life; and finally to both my parents, Ludgero and Minda, for being two of the most intelligent people that I know of. My father, for being a grounded, pragmatic person, responsible for my pursue of Electrical Engineering; and my mother, for being a strong, passionate person, in whom I can always confide, and for having the continuous belief that I am capable of everything, even when I think I am not.

With the “I’d like to thank the academy” moment over, I just wanted to finish this by saying:

To each and every one of you – I could not have done this without you. Thank you.

Abstract

The world is witnessing a tide of change in the photovoltaic industry like never before; we are far from the solar cells of ten years ago that only had 15-18% efficiency. More and more, multi-junction technologies seem to be the future for photovoltaics, already hitting the mark of 30% under 1-sun. This master's thesis focuses especially on a state-of-the-art triple-junction solar cell, the GaInP/GaInAs/Ge lattice-matched, that is currently being used in most satellites and concentrator photovoltaic systems.

The three subcells are first analyzed individually and then the whole cell is put together and simulated. The typical figures-of-merit are extracted; all the $I - V$ curves obtained are presented, along with the external quantum efficiencies. A study on how temperature affects the cell was done, given its relevance when talking about space.

An overall optimization of the cell is also elaborated. In this study, the cell's thickness and doping are changed so that maximum efficiency can be reached. Graphic plots for better understanding of how varying both these properties affect efficiency are provided.

Keywords

Photovoltaics; Solar Cells; Space; Concentrator Photovoltaics; GaInP/GaInAs/Ge; Multi-Junction; Triple-Junction.

Resumo

O mundo está a testemunhar uma maré de mudança na indústria fotovoltaica como nunca antes vista; as células de há dez anos atrás que apenas obtinham 15-18% de eficiência já nos são distantes. Cada vez mais, o futuro dos fotovoltaicos parece passar por tecnologias de multi-junção, com estas já passando a recorde dos 30% sob 1-sol. Este trabalho foca-se especialmente numa célula tripla-junção que já é estado-da-arte em alguns ramos, GaInP/GaInAs/Ge lattice-matched, usada principalmente em satélites e concentradores fotovoltaicos.

As três sub-células são analisadas individualmente primeiro, construindo-se depois a célula no seu todo e simulando-a de seguida. Os parâmetros específicos da célula são retirados; as curvas $I - V$ obtidas são apresentadas, em conjunto com as eficiências quânticas externas. Um estudo em como a temperatura afecta a célula foi feito, tendo em conta a sua relevância quando falamos de missões espaciais.

Também foi realizada uma optimização global da célula no seu todo. Neste estudo, a grossura e os valores de "doping" da célula foram alterados para se atingir a eficiência máxima. Gráficos que ajudam a melhor perceber em como ambas estas propriedades afectam a célula são apresentados.

Palavras Chave

Fotovoltaico; Células Solares; Espaço; Concentradores Fotovoltaicos; GaInP/GaInAs/Ge; Multi-Junção; Tripla-Junção.

Contents

List of Figures

List of Tables

Acronyms

PV	photovoltaic
MJ	multi-junction
NASA	National Aeronautics and Space Administration
TJ	triple-junction
SJ	single-junction
SEP	solar electric propulsion
LEO	low-Earth orbits, < 1000km
MEO	mid-Earth orbits, ~ 2000 to 12000km
GEO	geosynchronous orbits, 35780km
CPV	Concentrator Photovoltaic
QE	Quantum Efficiency
EQE	External Quantum Efficiency
EHP	electron-hole pair
AR	anti-reflection
STC	Standard Test Conditions
LM	Lattice-matched
MJSC	multi-junction solar cell
HIHT	high intensity high temperature
LILT	low intensity low temperature

CHAPTER 1

Introduction

1.1 Motivation

In the modern world, it is well known that electricity is a key asset to the mass population – it is present in the most varied aspects of people's lives, which makes it one of the most important factors in a country's economic and technological development. The electric power consumption of the world has been constantly rising since 1970 and according to the US Department of Energy, it is expected to increase by 44% from 2006 to 2030 [1]. It is widely known that fossil fuels are still at the forefront of the global energy production (around 80%), which raises several alarms since fossil fuels are one of the most prominent causes of environmental degradation. There is also the fact that the continuous fluctuation in fuel prices does not make this type of production sustainable in the long run.

There is then a growing crisis in the energy sector, and it is already one of the major issues of modernized countries, driving researchers all across the globe to propose new energetic solutions to meet the ever-challenging world's energy demands. In the present time, the alternative seems to be the renewable energy sources and in particular, solar energy, due to its enormous potential; it is known that the energy that the sun delivers every second has the order of magnitude of 10^{26}J – this means that, in two days, the sun has delivered to earth more than all the energy that the world's crude oil reserves are capable of producing [2].

The photovoltaic industry has been able to provide positive feedback to all the challenges that it has faced over the years and it has been growing since the last decade at a low but steady pace. For the future, the prospect is good – as the price of fossil fuels continues to rise, in the next decade or two, it is very probable to have solar power as a primary and efficient power source.

1.2 Topic Overview

The theory behind photovoltaic systems, in a nutshell, is having one semiconductor material to which we add a small number of impurities. These impurities are known as dopants and change the material conductivity by orders of magnitude making the photovoltaic effect possible and thus the generation of direct current. The most common cells used in these systems are still based on crystalline silicon, being it single crystalline (c-Si) or Polycrystalline (p-Si). These pioneer cells are part of the first generation of photovoltaics and are normally called Si-wafer technology. The second technology of PV[1] is made of thin-film cells composed of materials such as the Amorphous Silicon (a-Si) and Cadmium Telluride (CdTe). Both these generations are commercially mature and reach maximum efficiencies that go from 12.2% to 25%.

This work will be focusing on a special set of solar cells that already belong to the third generation of photovoltaics, known for implementing MJ[2] technology. These cells are made of III-V semiconductors (their composition is made of elements in groups III and V of the Periodic Table) and are capable of reaching some of the highest efficiencies observed in the photovoltaic industry to this day. This is due to the efficient use of the light's spectrum – by stacking different subcells made with III-V semiconductors on top of each other, each one having a higher bandgap than the one below it and thus absorbing light from a spectral range nearest to its bandgap, the overall efficiency is boosted significantly. The main suppliers of III-V solar cells in the market in the present day are Spectrolab, Emcore and Azur Space.

1.3 Objectives

The main aim of this thesis is to study III-V solar cell technology by trying to deliver a model that can simulate the behavior of the state-of-the-art GaInP/GaInAs/Ge triple-junction cell. The model should be able to characterize the cell, extracting its most relevant figure-of-merit, such as the $I - V$ characteristic, including major parameters such as the short-circuit current and open-circuit voltage, the fill-factor, and, naturally, the efficiency. While doing this, the model should also deliver accurate results, which will then be compared with the ones obtained in the most recent published research.

Since there was no opportunity to try and have a prototype of these cells in the laboratory for experimental testing, the results are verified by comparing them to the ones already published by credible journals in the field of photovoltaics.

With the model established, an optimization of the studied cell is intended, in order to reach the maximum efficiency possible and to understand how certain properties influence the cell's behavior.

[1] photovoltaic
[2] multi-junction

1.4 Thesis Outline

The thesis is divided into the introductory chapter, this one, and another four major chapters, along with three appendices.

The second chapter is the State-of-the-Art chapter, in which is discussed the fields of application of the III-V solar technology, along with why III-V cells are so crucial in those fields. The chapter also provides a somewhat extensive analysis of the perks of III-V solar tandem cells, studying the design of the latest technologies used in III-V photovoltaics.

The third chapter includes the basic theoretical concepts that serve as the foundation for most of the notions discussed in this work, providing useful insight for the reader. The chapter is divided into two large sections: the first one being *Semiconductors*, in which the basic physics of semiconductors are presented; and the second one, *Fundamentals of solar cells*, which, like the name suggests, includes an analysis of the most elementary concepts of solar cells.

The fourth chapter Simulations is divided into three sections: the first is used for providing a background of the simulation software that was used and discussing some of its basic functions; in the second one all the materials' properties that were used for simulation are presented; and the third and final one, all of the simulation results are displayed, followed by with their necessary observations.

The fifth and final chapter is reserved for the conclusions that could be drawn from the obtained results. In order to do this, a critical analysis of the achieved results is made. A section that focuses on possible future works with the purpose of improving this work is also presented.

The three appendixes are Appendix A, consisting in a brief review on *Semiconductor Junctions*, in which the operation method of p-n junctions is examined; Appendix B, a table of constants pertinent for this work; and finally, Appendix C, which contains the source code that was run for the simulation of the cell.

CHAPTER 2

State of the Art

2.1 Fields of application of III-V multi-junction solar cells

The III-V multi-junction cells are being used in the most varied fields of application, given their high-efficiency behavior. In the context of this work, the most important are the space applications, such as satellites and space vehicles (Figure 2.1a), and terrestrial concentrator systems (Figure 2.1b).

To be able to test solar cells in these two very different conditions, the use of different reference spectra is necessary, as it is explained in section 3.2.1.

In these fields, record efficiencies of 35.8% (AM0 spectrum, $1\,\mathrm{sun}$) [3] and 46% (AM1.5d spectrum, $508\,\mathrm{suns}$) [4] were already achieved, and researchers are currently trying to optimize the cell structure with aim of further improving these performances.

2.1.1 Space applications

At the time this work is being written, the III-V MJ solar cells are the state-of-the-art for satellites and space vehicles, having substantially replaced silicon cells on satellite launches [5]. The reason has to do with the fact that these cells have particular characteristics that make them suitable for the space environment, such as high reliability, high power-to-mass ratio $(\mathrm{W\,kg^{-1}})$, excellent radiation resistance, and a small temperature coefficient [6].

In this section, the unique aspects required to operate in the demanding space environment will be presented, as well as how the III-V tandem[1] cells have changed the conjecture of photovoltaic usage in the infinite void above – the outer space.

[1] another word for multi-junction

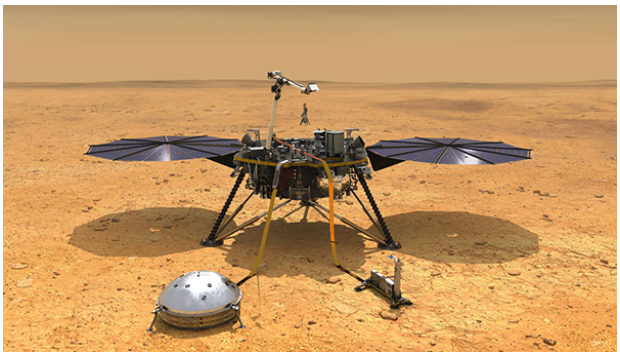

(a)

(b)

Figure 2.1: Some examples of solar cells use in space and terrestrial applications: (a) NASA's InSight Lander robot, powered by solar energy, already owning the off-world record of power generation. (b) A HCPV parabolic system that uses high-efficiency multi-junction modules by Solartron Energy Systems.

2.1.1.A High Radiation Exposure

One important aspect is the spectral radiation that is at one's disposal in space. Whereas in Earth we have a protecting set of layers made of gas particles commonly known as the atmosphere, in space, nothing is filtering the radiation. In addition to that, in space, the shielding effects of the Earth's magnetic field are no longer available, which means that there are high-energy electrons and protons in abundance. That is why space solar cells have to be equipped to contend with these external factors that can damage the efficiency of the cell arrays and limit the duration of the semiconductor materials.

This is valid for mid-Earth orbit (MEO) missions, on which cells must pass the Van Allen radiation belts and thus are exposed to harsher doses of radiation. It is because of occurrences like this being quite often in space, that there were established two different definitions for cell efficiency [7]; the beginning-of-life (BOL) efficiency, measured directly after cell production, and the end-of-life (EOL) efficiency, measured at the end of the space missions.

A high EOL efficiency is of paramount importance when talking about the weight and cost of the all system since these two are intrinsically connected when the launch of a spacecraft is involved. For instance, the launch cost of satellites in the LEO[2] is around $11000\,\$\,\mathrm{kg}^{-1}$ and for GEO[3] is up to $66000\,\$\,\mathrm{kg}^{-1}$ [7]. This leads to another important aspect of spacecraft design that relates to weight, called the power-to-mass ratio.

2.1.1.B Power-to-mass ratio

As of now, the leading space solar cells are the triple-junction GaInP/GaInAs/Ge with an efficiency of $28-30\%$ (AM0) [8], that can reach a specific power of $360-500\,\mathrm{W\,kg}^{-1}$ [9]. This meets the requirements

[2] low-Earth orbits, <1000km
[3] geosynchronous orbits, 35780km

of not only many near to Earth missions but also the NASA[4] Office of Space Science (OSS) missions that utilize SEP[5] and require high specific power values. Some examples are missions that are conducted in harsher environments, such as with low solar intensity and low temperature (LILT) conditions, or high solar intensity and high temperature (HIHT) conditions and high radiation exposure [10].

Hence, a very important asset that III-V MJ cells offer, regarding space applications, is a higher power-to-mass ratio $(\mathrm{W\,kg^{-1}})$, where the cost factor is determined by $€\,\mathrm{kg^{-1}}$ and not $€\,\mathrm{W_p^{-1}}$ as it is in terrestrial applications [6].

2.1.1.C Temperature

Another important topic is the amplitude of temperatures that may be experienced in deep space. In the cosmos, particles of gas are sparse, and so, it is challenging to warm up anything by heat-transfer, unless under direct contact with sunlight. This also means that objects irradiate their heat very quickly into their surroundings, allowing abrupt changes in temperature to take place in this environment.

The solar intensity observed in orbit around the Earth will vary with its own elliptic orbit around the sun, reaching temperatures that go from $20\,°\mathrm{C}$ to $85\,°\mathrm{C}$. The average sun intensity in the orbit around Mercury is almost double that the one at Earth, translating into very high-temperature ranges, whereas around Jupiter's orbit, temperatures reach $-125\,°\mathrm{C}$, which means the PV equipment has to be prepared to face these circumstances.

The factor temperature is of utmost importance regarding solar cells, given that it affects several parameters, such as the short-circuit current or the open-circuit voltage, as it is stated in section 3.2.4.

Since the efficiency of power conversion is inversely proportional to temperature, it is useful to have a measure of how much the temperature will affect the performance of the cell – this is called the temperature coefficient. When operating under the AM0 spectrum (used for simulation of space conditions, please refer to Chapter 3, section 3.2.1 for information about the different spectra available), the normalized temperature coefficients of silicon-based cells are in the range of $-3 \times 10^{-3}\ /\,°\mathrm{C}$ to $-5 \times 10^{-3}\ /\,°\mathrm{C}$, while tandem cells of GaAs/Ge the have a lower (in module) temperature coefficient of approximately $-2 \times 10^{-3}\ /\,°\mathrm{C}$ for high temperatures [11].

2.1.1.D Thin-film technology

Diminishing the weight and volume of a space cell array is of paramount importance in space cell production and has been an on-going challenge for most spacecraft companies. As it was mentioned in section 2.1.1.B, some NASA missions, such as MEO[6] and GEO, require high specific power $(\mathrm{W\,kg^{-1}})$ and power density $(\mathrm{W\,m^{-2}})$ values. With these goals in mind, the thin-film technology was created,

[4] National Aeronautics and Space Administration
[5] solar electric propulsion
[6] mid-Earth orbits, ~ 2000 to 12000km

making lightweight, flexible, and high-efficiency cells a reality. In Spectrolab, the triple-junction GaInP/GaInAs/Ge cells with an area of $26.6\,\mathrm{cm}^2$ and a thickness of $50\mu\mathrm{m}$ were already demonstrated [12]. These cells' coupons showed an efficiency of 28% under AM0 illumination, and under a flexibility test ($50\mathrm{mm}$ curvature radius) continued showing nominal performance. The thin-cells also achieved a specific power of $500\,\mathrm{W\,kg}^{-1}$ (with the best cell reaching $1500\,\mathrm{W\,kg}^{-1}$) and a power density of $325\,\mathrm{W\,m}^{-2}$, which is a comparable behavior to standard rigid III-V multi-junction cells.

2.1.2 Terrestrial Concentrator Systems

On Earth, the implementation of III-V flat-plate modules, like the ones present in space applications, would represent a heavy production price, with the cost of a 40% efficiency III-V concentrator cell being at $10\,\$\,\mathrm{cm}^{-2}$ [13]. The way that PV manufacture companies found to counter this aspect was to make use of concentrator solar systems (CPV), in which the irradiance is augmented into a concentration of $400\,\mathrm{suns}$ or greater ($1\,\mathrm{sun}$ is the equivalent to the standard illumination under AM1.5). This reduces the required semiconductor area in order to achieve an acceptable cost of energy production.

These CPV systems work through the use of mirrors and lenses that allow for direct sunlight to be concentrated hundreds of times on photovoltaic cells. Typically, these PV cells are high-efficiency and most of these systems are high-concentration PV systems (HCPV), operating at high concentration factors, that go from $500\,\mathrm{suns}$ to $1000\,\mathrm{suns}$.

The most used type of PV cells for HPCV systems are the III-V solar cells since the amount of useful light that these cells are capable of absorbing is very high and their high-efficiency can be maintained in high concentration levels above $1000\,\mathrm{suns}$. This makes them the go-to technology for HCPV systems, with the achievement of a 3-junction GaInP/GaInAs/Ge concentrator metamorphic cell being the first solar cell technology to pass the benchmark of efficiency over 40% [14].

Despite that, there are still some adaptations that are necessary when using one-sun devices in terrestrial concentrator systems.

2.1.2.A The terrestrial spectrum

When operating under terrestrial conditions, there are numerous factors to be taken into consideration, such as the weather and varying sunlight intensity as a function of time. Consequently, optimum cell design is an aspect of significant importance to the CPV system configuration.

As stated in section 2.1.1, in space applications, cells are exposed to high-energy light. In a terrestrial CPV module, the equipment will no longer be under the AM0 spectrum and so high-energy light is no longer available. The relevant spectrum for CPV multi-junction cell design is then the AM1.5d, having less of the blue component compared to the AM1.5G, leading to a different optimum bandgap

combination. It also affects cell thickness – the common terrestrial concentrator top subcell thickness will have to be greater than the space subcell by a factor of two [15].

Regarding the sensitivity to particular wavelengths, it was already said in section 1.2, that the triple-junction GaInP/GaInAs/Ge absorbs light from a wide range of the sunlight spectrum.

As it is shown in the work of Cotal et al. [16], when under the AM1.5d spectrum (irradiance of $0.09\,\mathrm{W\,cm^{-2}}$), this same cell is capable of absorbing $0.0862\,\mathrm{W\,cm^{-2}}$, which corresponds to 96% of the total irradiance. It is also demonstrated that thickness plays a major part regarding the QE[7] of each subcell – for thicker emitters, there is a decrease of the QE, specifically for the blue component of light.

2.1.2.B Concentration versus Efficiency

Making use of the relations between the current and voltage in an ideal solar cell, we can predict how varying the concentration will affect the open-circuit voltage (V_{oc}) and the short-circuit current (I_{sc}) of the solar cell.

Recurring to what it is explained in section 3.2.3.A, one can see that when increasing the I_{sc} due to the increase of the incident light irradiance (concentration level) and assuming the saturation current I_0 remains constant, the V_{oc} will increase logarithmically by several kT/q factors. When working with multi-junction cells connected in series, every subcell will add to the increase in V_{oc} with concentration, increasing the fill-factor (FF) of the cell, leading to a rise in efficiency.

So, according to this, one could assume the higher the concentration, the higher the efficiency of a III-V concentrator solar cell. However, in reality, solar cells are not ideal and so there are losses that need to be taken into consideration, namely the series and shunt resistances not being ideal and therefore generating power losses (refer to section 3.2.3.C for a description of the 1D5P model for solar cells).

This will have a dominant impact on efficiency and will create a different shape for the $I-V$ characteristic of the cell, diminishing the FF and thus diminishing the efficiency. The greater the concentration level, the greater the impact on the efficiency; e.g. for a 3-junction GaInP/GaInAs/Ge a difference in the series resistance from zero to $R_s = 0.1\,\Omega$ results in the FF being reduced from 90% to 87%, at $83\,\mathrm{suns}$, and from 90% to 71% at $500\,\mathrm{suns}$ [16].

Therefore, the series and shunt resistances are adapted to operate under high concentration levels so that the losses can be negligible, to an extent. For every concentrator solar cell, there is a concentration limit for which the efficiency will start to drop.

There are studies being conducted in order to combine the rise in efficiency due to the voltage increase, and the efficiency depletion due to parasitic losses. These studies mainly use cells with a high number of junctions (3- to 6-junctions), since these devices are capable of operating at low-current and thus have fewer power losses.

[7] Quantum Efficiency

The demonstration of this reduction in the FF and efficiency for the single-junction GaAs solar cell can be found in the work of Steiner et al. [17]. In the same work, three tests were made; three optimized grids for concentrations of $C = 100$, $C = 450$ and $C = 1000$, which showed a maximum efficiency of 29.09% for a concentration of $450\,\mathrm{suns}$.

2.2 III-V Solar Cell Design

The main aim of this work is to study a III-V multi-junction solar cell, and so it is important to know the fundamentals behind its design, given that they can differ quite a bit from the usual single-junction cell. Is has been stated that III-V MJ cells are top performers when compared with SJ[8] cells, and that is because the latter have their efficiency limited *a priori*, as it is going to be discussed in further in section 2.2.1.

2.2.1 Bandgap versus efficiency

Considering a single-junction solar cell with bandgap W_G, only photons with energy W_{ph} higher or equal to W_G are absorbed. Although, if the photon energy is higher than the bandgap, $W_{ph} > W_G$, there is an excess of energy that will be lost as heat, a phenomenon also known as thermalization losses. This excess of energy is as higher as the photon energy and as lower as the energy that will be effectively transformed into electric current. This implies that the device operates at maximum efficiency when $W_{ph} = W_G$, which taking into account the wide-ranging spectrum of sunlight, translates into rather limited overall efficiencies.

Theoretically, this problem has a simple resolution; instead of trying to convert the maximum energy possible with just one bandgap value, one could just try to divide the sunlight spectrum into several spectral sections and associate a subcell, with an adjusted bandgap value, to each one of these sections. This way, every subcell would be tuned to absorb light in a specific region of the spectrum. This concept can be viewed as the crown jewel achievement of multi-junction manufacture.

2.2.1.A Spectral splitting approaches

As stated previously, the solution is to resort to subcells adjusted to the incident photon's energy. However, there could be some different approaches to this problem. One comes from a rather intuitive concept, present in everyone's mind, concerning the splitting of the spectrum, which consists in the use of a prism in order to separate a beam of white light into several different photon energies. Subcells with different bandgaps would be arranged spatially so that each one could absorb the respective photons

[8] single-junction

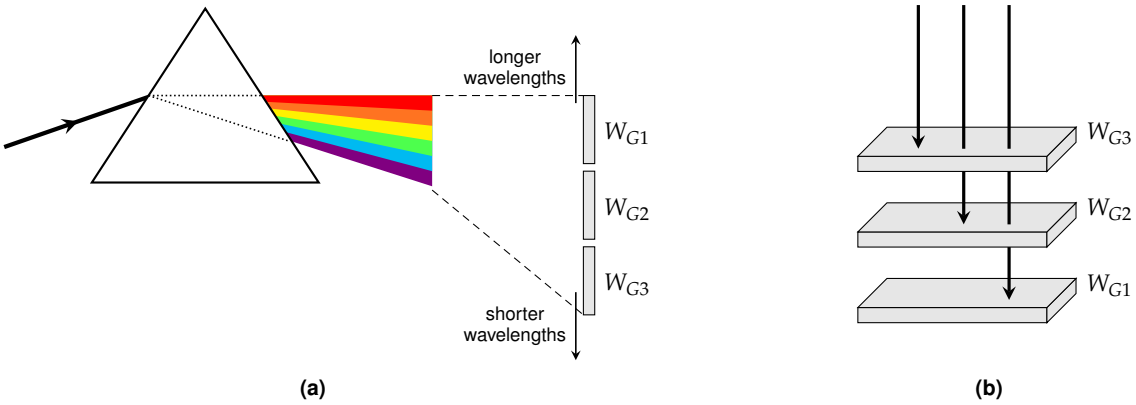

Figure 2.2: Spectral splitting approaches: (a) Spatial distribution, with the use of a prism, and (b) Stacked distribution of a 3-junction cell.

of different wavelengths. This method is illustrated in Figure 2.2a, and although it may be recognized as one of the most famous album covers in history, in CPV[9] systems it is referred to as spatial spectrum distribution.

Even though this may sound simple, in practical terms, it is a quite complex approach. The optical properties behind it, as well as the mechanic difficulties, make it, more often than not, an unattractive method for spectral splitting. One approach that is broadly utilized today is the stacked distribution. In this method, subcells are stacked on top of each other as their bandgap progressively increases, so that the subcell with lower bandgap is placed in the bottom of the cell and the one with a higher bandgap is placed on the top.

The reason behind this placement is to make the high energy photons be absorbed right on the subcells with higher bandgaps, leaving the low energy photons to the subsequent low bandgap cells, as shown in Figure 2.2b. In the case of a TJ[10] solar cell, the subcell on top will absorb photons with energy $h\nu > W_{G3}$, the subcell in the middle will absorb photons with energy between $W_{G2} < h\nu < W_{G3}$, and lastly, the bottom subcell will absorb photons with energy $W_{G1} < h\nu < W_{G2}$. It is, then, essential that the bandgaps descend from top to bottom, so that the photons are efficiently distributed throughout the stack.

2.2.1.B Optimal bandgap combination

The use of III-V semiconductors in the production of MJ cells provides a high versatility in bandgap combinations for each subcell, that, depending on how they are implemented, can show great efficiency. With this in mind, Fraunhofer ISE developed the etaOpt software, which is capable of computing cell efficiencies based on how many p–n junctions they have, and what their bandgap values are. In Figure

[9]Concentrator Photovoltaic
[10]triple-junction

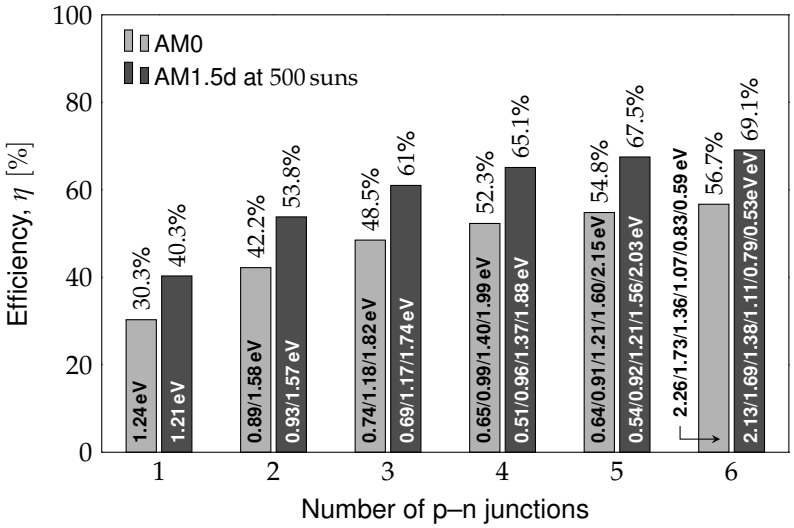

Figure 2.3: Maximum efficiencies for both space applications (AM0 spectrum) and concentrator systems (AM1.5d spectrum at 500 suns). Computed with etaOpt software. (Original image is from [6], p. 444)

2.3 are shown some optimal bandgap combinations for several numbers of p–n junctions, along with their efficiencies, for both space and terrestrial concentrator applications. It is clear that the efficiency increases with the number of p–n junctions, however, the surplus in efficiency decreases with the number of subcells.

2.2.2 Bandgap versus Lattice Constant

It has already been seen that searching for the optimal bandgap combination can be an arduous, yet rewarding mission. However, the choice of bandgap does not fall only in choosing appropriate values for each spectrum region – it also falls in the choice of a lattice constant, which is another characteristic property of semiconductors.

When analyzing the structure of a multi-junction solar cell, if the materials all have, approximately, the same lattice constant, one says that the cell is *lattice-matched* (LM). On the other hand, if they have different lattice constants we say that the cell is *lattice-mismatched* or *metamorphic* (MM).

This is particularly important given that the more the lattice-constants of the stacked layers differ from one another, the more probable is the creation of dislocations, that can ruin the quality of the material. Therefore, the production of metamorphic cells has to be considered carefully as appropriate strategies must be taken into consideration.

The TJ cell $Ga_{0.5}In_{0.5}P/Ga_{0.99}In_{0.01}As/Ge$ is a representation of a lattice-matched cell, since the materials all have practically the same lattice constant. This is illustrated in Figure 2.4, in which one can see the line that indicates the lattice-matched $Ga_{0.5}In_{0.5}P/Ga_{0.99}In_{0.01}As/Ge$ solar cell with detail, and next to it the relation between the bandgap and lattice constant for several compound III-V semiconductors.

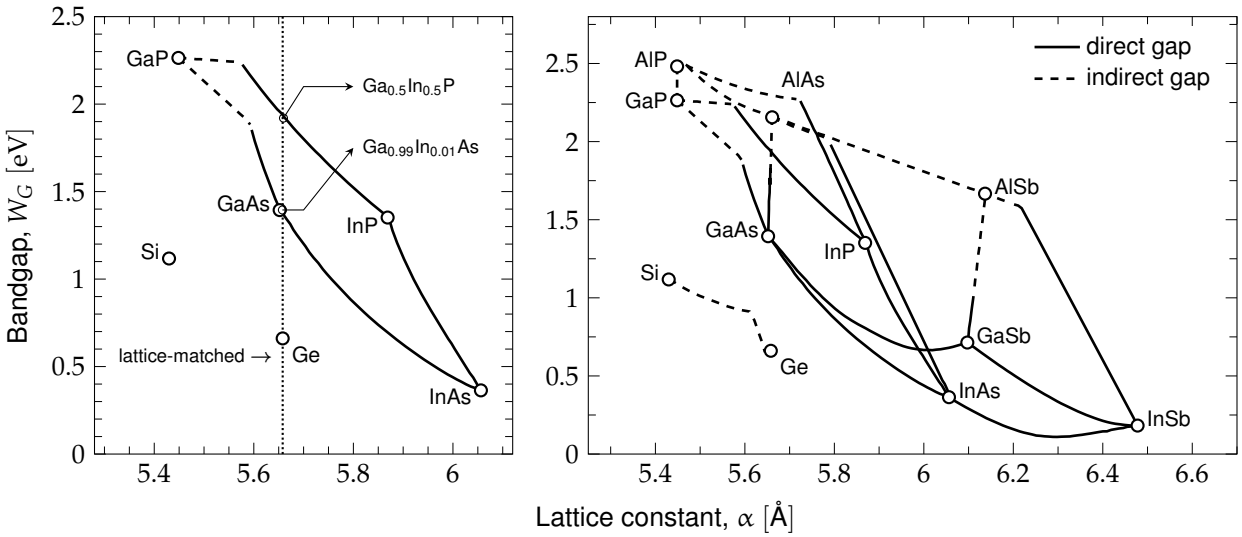

Figure 2.4: Bandgap as a function of the lattice constant for several III-V semiconductors. In the first plot, the line that represents the lattice-matched $Ga_{0.5}In_{0.5}P/Ga_{0.99}In_{0.01}As/Ge$ is displayed.

2.3 III-V Solar Cells Structures

Several approaches to III-V solar cell production continue to be researched, with some of them showing great potential in terms of the cost-efficiency relationship, such is the case of III-V growth on Si. Regarding high-efficiency values, right now III-V cells with more than three junctions are already capable of $1\,\mathrm{sun}$ efficiencies of more than 38% [4].

However, in the context of this work, it seems only relevant discussing the approaches in which GaInP/GaInAs/Ge solar cells are utilized. The most relevant examples are the lattice-matched triple-junction and the upright metamorphic structures [16], which will be the main focus of this thesis.

2.3.1 Lattice-matched triple-junction

The lattice-matched TJ $Ga_{0.5}In_{0.5}P/Ga_{0.99}In_{0.01}As/Ge$ is currently the state-of-the-art III-V solar cell for space as well as terrestrial concentrator applications [8]. All the subcells have approximately the same lattice constant, assuring that no dislocations are created between the materials and thus facilitating good material quality.

This cell consists of three p–n junctions made from GaInP, GaInAs, and Ge, stacked in series, each subcell with a bandgap higher than the one below it, as it was explained in section 2.2.1. It is on the surface of the top cell that light will fall on the device. Each subcell is connected by tunnel junctions (see Chapter 6, section 6.1.2 for an extensive review on this subject) with low resistance and high

optical transmissivity coefficients. A schematic of a typical lattice-matched GaInP/GaInAs/Ge solar cell is shown in Figure 2.5a.

This cell already demonstrated a $1\,\mathrm{sun}$ efficiency of 32.0% under the AM1.5G spectrum [14], which shows that the technology is well matured. Nonetheless, this cell does not split the spectrum in an optimal manner, resulting in excessive current in the bottom Ge cell. One solution to this issue is to increase the absorption in the upper cells, resulting in less current discrepancy.

2.3.2 Upright metamorphic growth

As was just mentioned, a surplus current in the bottom cell is verified in the lattice-matched TJ cell given the difference between the bandgaps of the middle $(1.42\,\mathrm{eV})$ and the bottom $(0.66\,\mathrm{eV})$ cells. One way to mitigate this issue is to lower the bandgaps of the top and middle cells by increasing the In composition in both $Ga_xIn_{1-x}P$ and $Ga_xIn_{1-x}As$ materials. However, lowering the bandgap of both these materials implies a lattice constant increase, as one can observe in Figure 2.4. As it was previously stated in section 2.2.2, the use of lattice-mismatched materials in monolithic structures results in

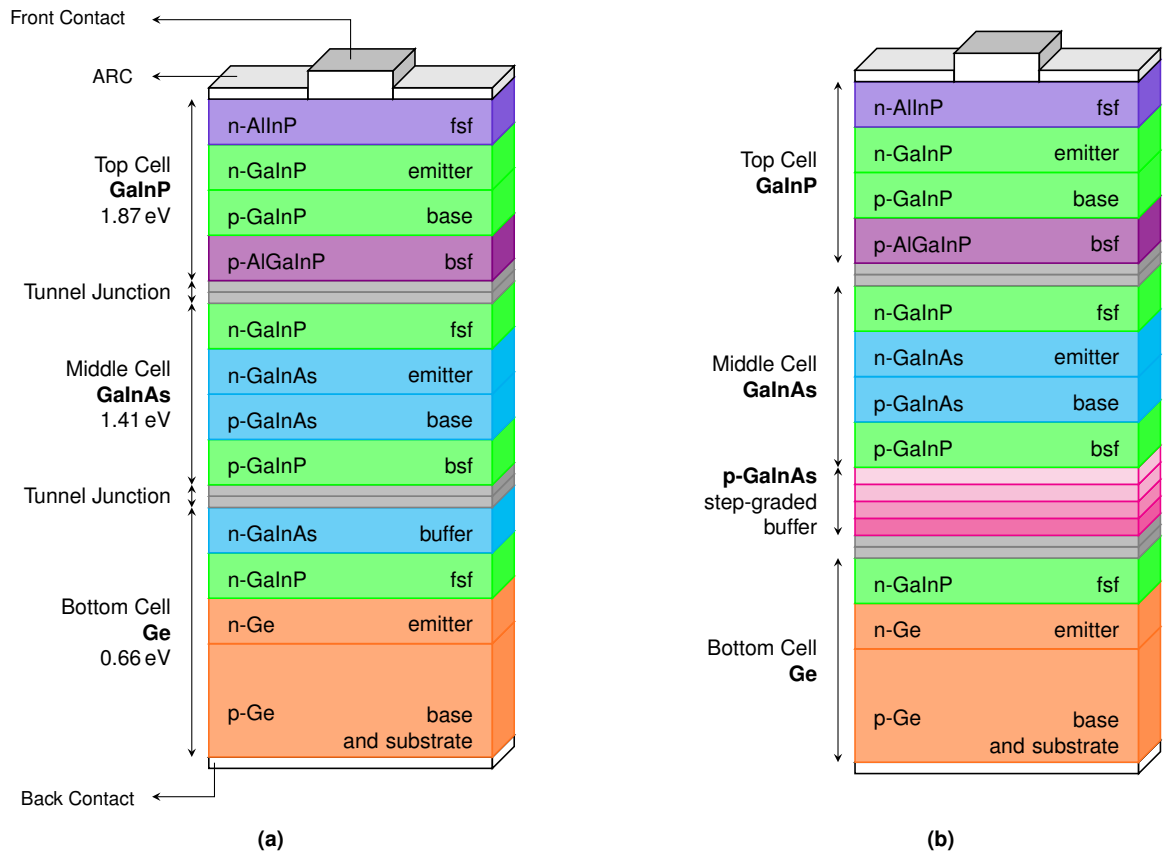

Figure 2.5: Schematic cross-sections of the TJ $Ga_{0.5}In_{0.5}P/Ga_{0.99}In_{0.01}As$/Ge cell: (a) lattice-matched, and (b) upright metamorphic approaches.

dislocations that harm material quality, and so special tactics are required. In the case of the upright metamorphic TJ cell, one of those tactics is implementing a GaInAs graded buffer between the middle and bottom cells, so that the lattice constant is increased gradually and thus minimize the dislocations. A regular structure approach for a TJ GaInP/GaInAS/Ge cell is shown in Figure 2.5b.

CHAPTER 3

Theoretical Concepts

3.1 Semiconductors

Semiconductors are at the basis of all electronics devices due to their versatility since their properties can be changed to fit multiple purposes – the one that this thesis will focus on is energy conversion.

Since this work is focused on the modeling of a MJ solar cell, a comprehensive and detailed study of the various properties of semiconductors is required in order to understand how they can influence several aspects of the cells – and how adjustments can be made in order to improve the overall model and obtain the best results possible.

3.1.1 Semiconductor materials

Semiconductor materials can be composed of atoms from different groups in the Periodic Table and according to each group, certain properties can change.

Semiconductor materials are either from group IV, a combination of elements from either groups II and VI or from groups III and V, the latter being the kind of materials this work will focus on the most. These materials are called III-V semiconductors.

The most liable semiconductors right now are silicon (Si) and germanium (Ge), both in group IV of the Periodic Table. In Figure 3.1, it is possible to see the most common semiconductor materials (in red) and in what groups are they inserted.

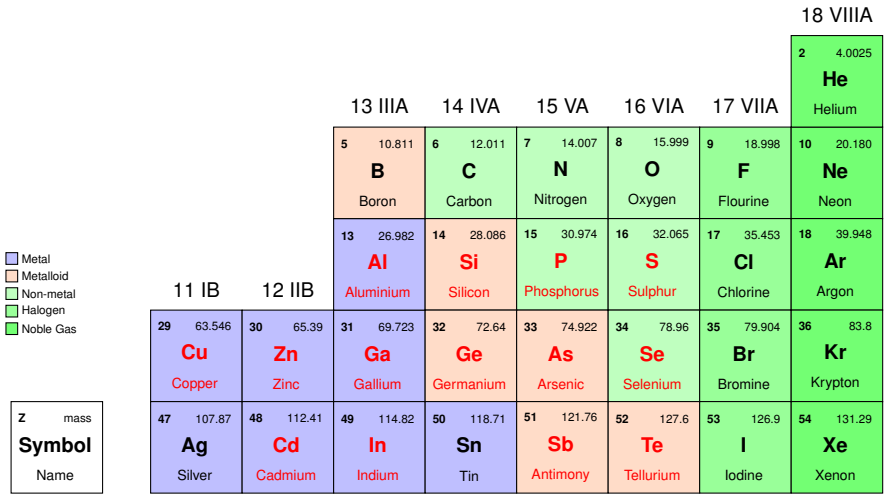

Figure 3.1: Fraction of the Periodic Table; the most common semiconductor materials are represented in red. Original image from [18].

3.1.2 Conduction

At the temperature of 0K, the absolute zero, all the electrons in the atom are tightly held, being "stuck" in their covalent bonds and so cannot take part in any energy flow. However, this changes as the temperature rises – the heat will increase the energy of valent electrons[1] and some of them "break free" of their bonded structure, becoming *free electrons* and are responsible for conducting current. As a result, we say the conductivity rises with temperature (up to a certain point).

When electrons "break free" of their covalent bonds, it is said that they leave a positive charge where they used to be, appearing as if covalent bonds are "moving" through the crystal lattice. These positive charges are also known as *holes* and their charge value is equal to the absolute value of the electron's charge. Electrons and holes together form what is called a *electron-hole pair* (EHP). Since both these particles, electrons and holes, are the main participants in the conduction of current, they are given the name of *charge carriers* or simply *carriers*.

Electrons are quantum particles and can only exist in discrete values of energy; these possible states are called *energy levels* (Figure 3.2). Since these states are quantified, the electron cannot be between two energy levels; whether the electron is at a low energy state or has gained the minimum energy required to transition to a higher energy state. When this transition happens, from one orbit of a lower (or higher) energy level, the electron emits (or absorbs) energy (Figure 3.3).

However, when talking about a material, there is more than one atom to be considered; for a solid with N atoms, each level of energy will have to accommodate the electrons of the N atoms and so each level will have to spread in N levels of energy. These levels will then be grouped together and form what

[1] Valent electrons are electrons that exist in the outermost orbit – the valence shell.

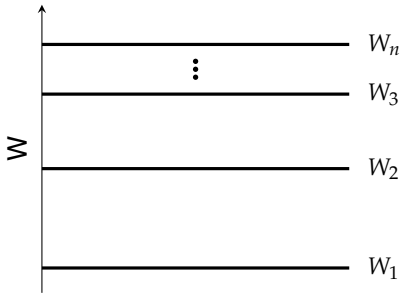

Figure 3.2: Quantified energy levels for an electron in a single atom.

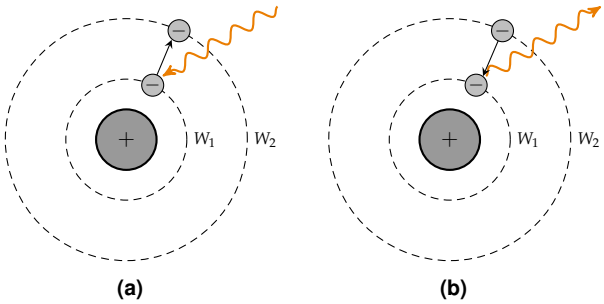

Figure 3.3: Transition between levels: (a) lower to higher (absorption of energy); (b) higher to lower (emission of energy).

is called an *energy band*.

3.1.3 Bandgap

Free electrons are in high energy states and exist in the *conduction band*. Electrons that are "bound" are said to be in low energy states and belong in the *valence band*. The difference between the conduction band and valence band energies is called *energy bandgap* or just *bandgap* W_G, and one can write that $W_G = W_C - W_V$. The bandgap consists in the energy that one electron has to gain in order to "break free" and transit to a higher energy state. Electrons cannot exist in the bandgap and so this band is also called the forbidden band in opposite to the allowed bands, where electrons can take place, such as the conduction and valence bands.

It is the value of the bandgap that distinguishes metals, semiconductors, and insulators. In metals, there is no bandgap and electrons move freely from one band to another. Materials with the bandgap superior to $4.5\,\mathrm{eV}$ are typically called insulators. In the middle, with properties that allow them to act as metals (conductors) or insulators, are the semiconductors (Figure 3.4).

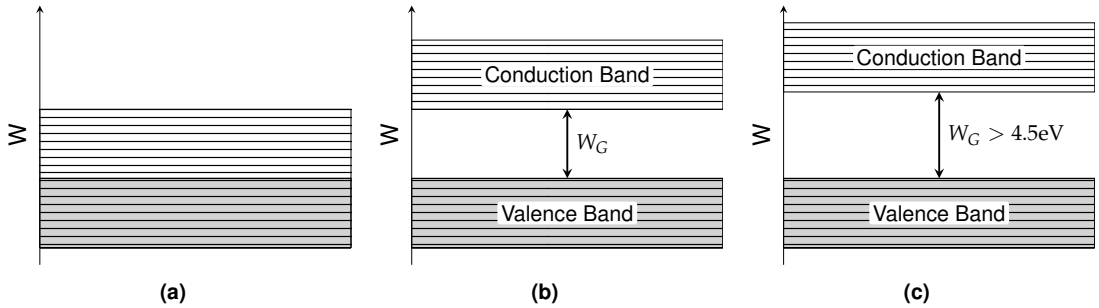

Figure 3.4: Band diagrams for several types of materials: (a) Metals; (b) Semiconductors and (c) Insulators.

3.1.4 Band structure

In order to characterize the type of band alignment, one must resort to the free electron's kinetic energy (W_k) since it is common to assume that its potential energy is zero. The kinetic energy of the electron will be given by:

$$W_k = \frac{p^2}{2m_0}, \tag{3.1}$$

in which p is the electron's momentum and m_0 is the electron's rest mass, $m_0 = 9.11 \times 10^{-31}\mathrm{kg}$.

It is this relation $W(p)$ that will allow dividing semiconductors into two different categories: *direct-gap semiconductors* and *indirect-gap semiconductors*. In the direct-gap semiconductors, the minimum of the conduction band and the maximum of the valence band energies are associated with the same value of momentum. In the indirect-gap semiconductors, the conduction band's minimum and the valence band's maximum exist in different values of the momentum. Both of these concepts are illustrated in Figure 3.5.

Having this difference established is important since when working with *compound semiconductors* there are certain properties that will vary differently if the compounds are direct gap or indirect gap semiconductors as it will be further discussed in section 3.1.5.A.

3.1.5 Compound semiconductors

Compound semiconductors are made of two or more elements from different groups of the Periodic Table. They are divided into binary, ternary, or quaternary compounds depending on how many elements they possess.

The ternary compounds are obtained by adding two binary semiconductors together; adding the binary compounds AB and CB where (A, B) belong in the same group, the ternary compound $A_xC_{1-x}B$ is obtained, in which x is the concentration of the A element in relation to C and its value varies from

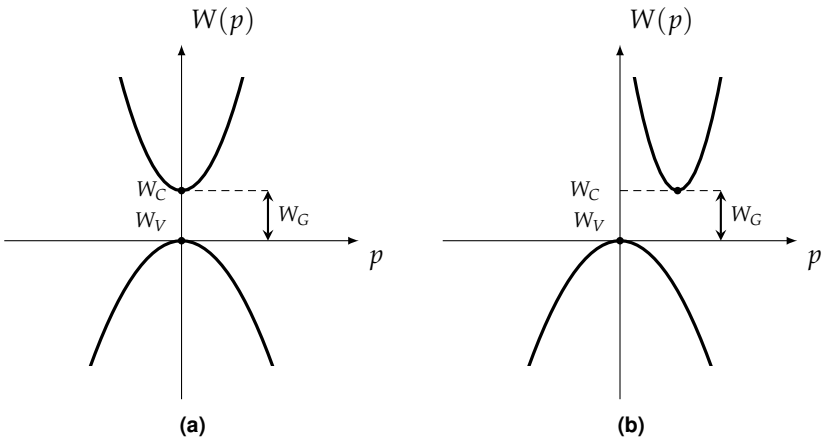

Figure 3.5: Energy vs. momentum for: (a) direct gap semiconductors; (b) indirect gap semiconductors.

$0 \leq x \leq 1$.

Finally, there are the quaternary compounds that are derived from four binary compounds; AC, AD, BC and BD where (A, B) and (C, D) belong to the same Periodic Table group. All together, they form the quaternary compound $A_xB_{1-x}C_yD_{1-y}$ in which y is a parameter similar to x and represents the concentration of the C element in relation to D.

In this work, two important III-V ternary compounds will be extensively mentioned: indium gallium phosphide ($Ga_xIn_{1-x}P$), made of the two binaries gallium phosphide (GaP) and indium phosphide (InP); and indium gallium arsenide ($Ga_xIn_{1-x}As$), made of gallium arsenide (GaAs) and indium arsenide (InAs).

3.1.5.A Property variation with composition

The properties of the compound semiconductors will depend on the binaries' properties that originated them. This dependency relates to the composition x, sometimes linearly. Some of the properties that are known to have a linear variation are the lattice constant (α) or the relative permittivity (ε_r), whereas the bandgap (W_G), the mobility (μ) and the electron affinity (χ) have a non-linear behavior.

Alas, for a ternary compound, this variation can be expressed as a function of x as follows:

$$\alpha_{A_xB_{1-x}C} = x\alpha_{AC} + (1-x)\alpha_{BC}, \tag{3.2}$$

and an identical expression can be used for quaternary compounds:

$$\alpha_{A_xB_{1-x}C_yD_{1-y}} = xy\alpha_{AC} + x(1-y)\alpha_{AD} + (1-x)y\alpha_{BC} + (1-x)(1-y)\alpha_{BD}. \tag{3.3}$$

In both expressions, the property used for exemplifying was the lattice constant, but the expressions are valid for other properties that have a linear behavior with composition.

In this work, both (3.2) and (3.3) expressions will be extensively used, mostly to calculate the relative permittivity ε_r of all the compound semiconductor materials that will be used.

3.1.5.A.1 Non-linear behavior

As it was already stated, there are some properties of compound semiconductors that do not show a linear behavior as the composition varies. This is particularly relevant since the bandgap W_G and relative permittivity ε_r are important variables in order to build the solar cell model.

When analyzing the bandgap of compound semiconductors, its variation with the composition x depends on the band structure of the binaries that give it origin, like Figure 3.6 suggests.

For the compound $Ga_xIn_{1-x}As$, in which both binaries are direct gap, the evolution of the bandgap with the composition (at 300K) is a parabola like the one shown in Figure 3.6a. For $Ga_xIn_{1-x}P$ however, as InP is direct-gap and GaP is indirect-gap, the graph will be characterized by having two branches, each one associated with the respective binary, as it is illustrated in 3.6b.

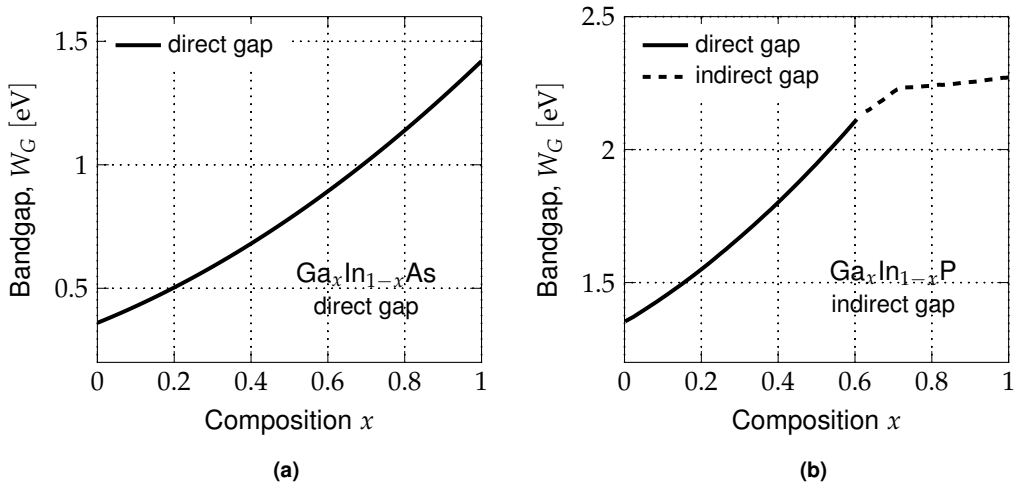

Figure 3.6: Bandgap variation with composition for: (a) GaInAs (original from [19]) and (b) GaInP (adapted from [20]) at 300K.

3.1.6 Intrinsic carrier concentration

A semiconductor is called *intrinsic* when it does not contain any impurities, being only composed with its original atoms. As was stated in section 3.1.2, at $T = 0\text{K}$, there are no free electrons roaming the lattice and so, there are no electron-hole pairs being formed. This changes as temperature rises, $T \neq 0\text{K}$, when electrons start to acquire energy and "escape" their covalent bonds, forming electron-hole pairs. This concept is illustrated in Figure 3.7 for an intrinsic semiconductor from group IV of the Periodic Table, such as Si or Ge.

When $T \neq 0\text{K}$ (Figure 3.7b) it is possible to notice that there is the same number of electrons in the conduction band that of holes in the valence band, since there is a situation of thermodynamic equilibrium. Under this equilibrium, the rate in which both generation and recombination processes happen is equal, thus the number of EHP's remains constant. This translates in the following relation:

$$n_0 = p_0 = n_i, \tag{3.4}$$

in which n_0 is the electron concentration, p_0 the hole concentration and n_i the *intrinsic carrier concentration*. Therefore, the product of electron concentration and hole concentration is constant, translating into the Law of Mass Action:

$$n_0 p_0 = n_i^2. \tag{3.5}$$

The intrinsic carrier concentration is a major characteristic of each semiconductor and has a connection with solar cell efficiency. It also depends on the temperature and the bandgap of the material in

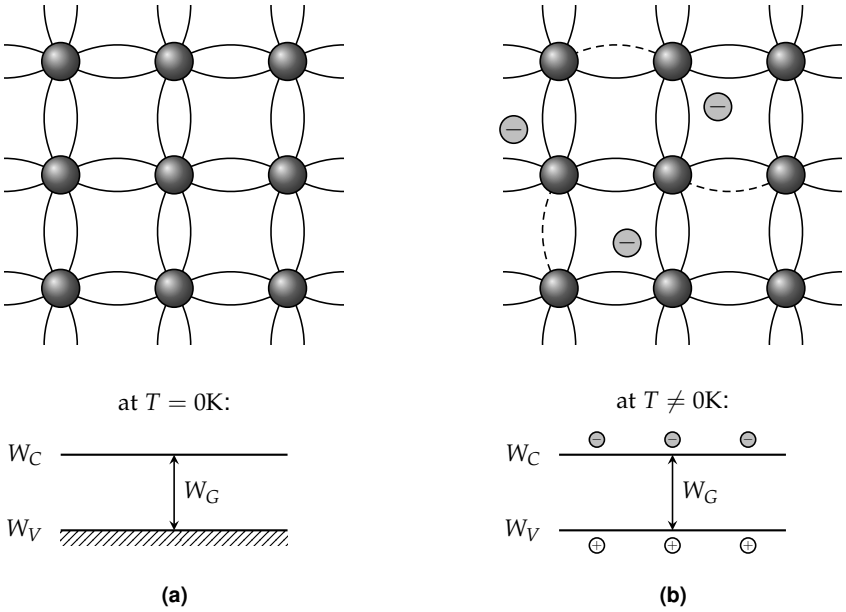

Figure 3.7: Schematic representation of the covalent bonding and the energy band models for an intrinsic Group IV semiconductor: (a) at $T = 0\text{K}$ and (b) at $T \neq 0\text{K}$. The material's atoms are represented in gray. Solid lines represent the covalent bonds and dashed lines are incomplete bonds. Both images were adapted from [21], p. 24.

study, as the following expression shows:

$$n_i \propto T^{3/2} e^{-\frac{W_G}{2kT}}, \tag{3.6}$$

where T is the absolute temperature $[\text{K}]$, W_G the bandgap $[\text{eV}]$ and k the Boltzmann's constant.

3.1.7 Doping

Extrinsic semiconductors are characterized by having other elements in their composition besides their original atoms. Adding these "impurities" is called *doping* and it changes the material electrical properties – this process is very important when discussing solar cell modeling since it allows one to alter certain cell properties depending on the desired performance.

There are two types of extrinsic semiconductors concerning the type of predominant carriers: when the added impurity is the *donor type*, the majority of carriers in the semiconductor are electrons and the material is identified as *n-type*; when the impurity is the *acceptor type*, the majority of carriers are holes and the material is called *p-type*.

In Figure 3.8 is considered a Group IV element doped with a donor impurity from Group V. At the absolute zero, all the four valence electrons from the main element are "trapped" in their covalent bonds, however, since there is one impurity atom with five valence electrons, there is one electron that is not

involved in any covalent bond, and so is roaming trough the lattice with higher energy than the rest. This energy is very close to the one of the conduction band, W_C, that is represented in the bands' model by the state of energy W_D.

Since W_C and W_D are so proximate to each other, at $T \neq 0\text{K}$ the electrons from the donor impurity just need a small quantity of energy in order to become ionized and transit to the conduction band, making the number of electrons in the conduction band much higher than the number of existent holes in the valence band (Figure 3.8b).

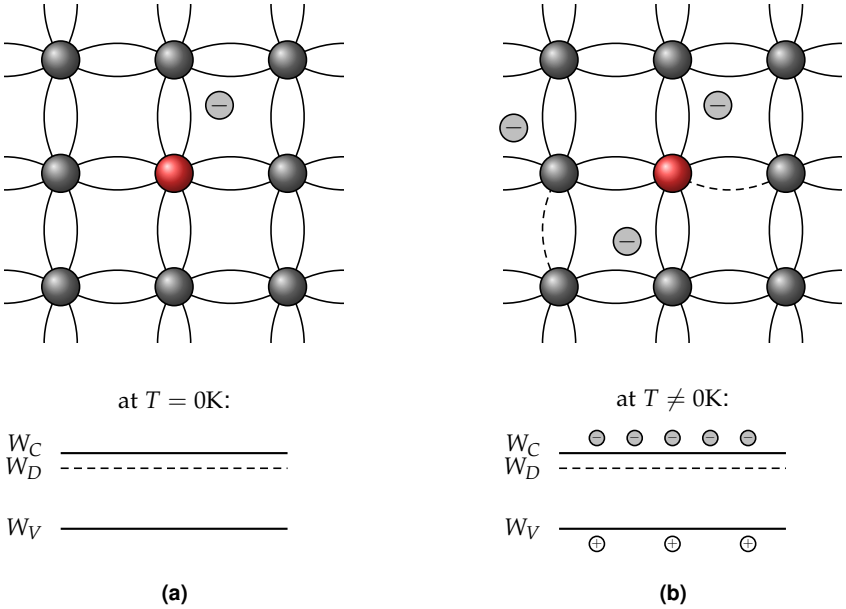

Figure 3.8: Schematic representation of the covalent bonding and the energy band models for a n-type semiconductor: (a) at $T = 0\text{K}$ and (b) at $T \neq 0\text{K}$. The material's atoms are represented in gray and donor impurity atoms in red. Solid lines represent the covalent bonds and dashed lines are incomplete bonds. Both images were adapted from [21], p. 28.

Discussing an acceptor impurity, the line of thought is analogous. In this case, for a Group IV semiconductor, the impurity will be from Group III. Given that the impurity's atom only has three valence electrons, it will result in one incomplete bond and thus, there will be a hole in the lattice. The energy of this hole, W_A, will be very close to the one of the valence band, W_V.

Hence, because of this proximity, a low rise in temperature is enough to ionize the impurities negatively, originating a higher concentration of holes in the valence band than of electrons in the conduction band (Figure 3.9b).

When in equilibrium, the majority carriers' density (electrons (n_0) in n-type materials and holes (p_0) in p-type materials) is equal to the intrinsic carrier concentration plus the density of carriers added by the doping material. Since the latter is several orders of magnitude greater than the intrinsic concentration,

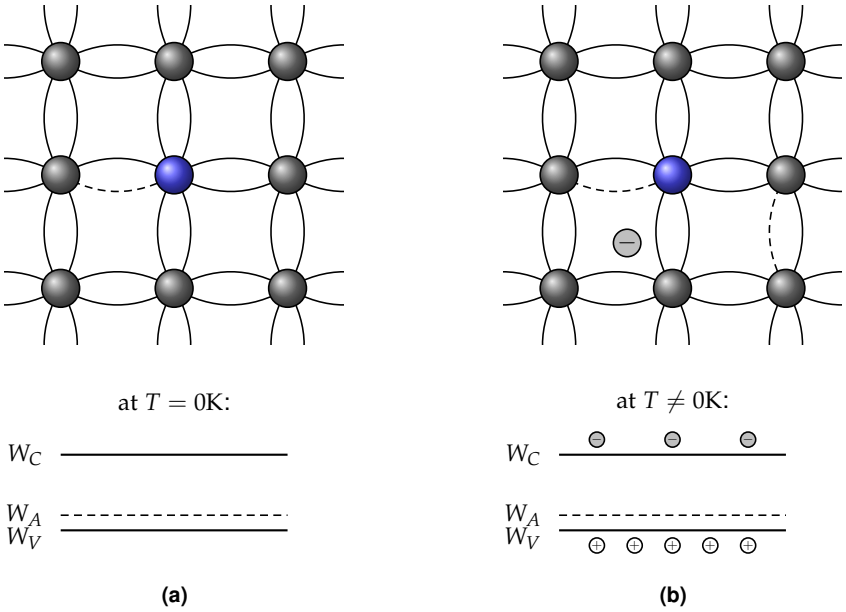

Figure 3.9: Schematic representation of the covalent bonding and energy band models for a p-type semiconductor: (a) at $T = 0$K and (b) at $T \neq 0$K. The material's atoms are represented in gray and acceptor impurity atoms in blue. Solid lines represent the covalent bonds and dashed lines are incomplete bonds. Both images were adapted from [21], p. 29.

and the Law of Mass Action (3.5) is verified, one can say that for:

$$\text{p-type semiconductor:} \quad p_0 = N_a^-, \quad n_0 = \frac{n_i^2}{N_a^-}, \tag{3.7}$$

$$\text{n-type semiconductor:} \quad n_0 = N_d^+, \quad p_0 = \frac{n_i^2}{N_d^+}, \tag{3.8}$$

where N_a^- is the concentration of impurities for acceptors and N_d^+ the concentration of impurities for donors.

Thus, it can be implied that if $N_d^+ - N_a^- > 0, n_0 > p_0$ and it is a n-type semiconductor; similarly, if $N_d^+ - N_a^- < 0, p_0 > n_0$ the semiconductor is p-type. If, by chance, the equation $N_d^+ = N_a^- \Rightarrow n_0 = p_0 = n_i$ is verified in equilibrium, the semiconductor is behaving intrinsically.

It is also important to deduct some important relations in extrinsic semiconductors; in thermodynamic equilibrium, the materials are electrical neutral, which means that the density of positive carriers are equal to the density of negative carriers. Mathematically speaking, one has

$$\rho = 0 = -q(n_0 + N_a^-) + q(p_0 + N_d^+) \Leftrightarrow$$

$$\Leftrightarrow \quad \underbrace{n_0 + N_a^-}_{\text{negative carriers}} \quad = \quad \underbrace{p_0 + N_d^+}_{\text{positive carriers}} \quad . \tag{3.9}$$

In equation (3.9), the first $(n_0 + N_a^-)$ and second $(p_0 + N_d^+)$ terms represent the density of carriers

(electrons and holes, respectively) which are originated by the phenomenon of generation.

3.1.8 Carrier statistics: estimation of *n* and *p* densities

In order to compute the charge carriers' densities, one must take into consideration that electrons and holes are seen as free particles, occupying specific states of energy. One can refer to these possible states as the *density of states* available in the entirety of the semiconductor, which is represented by the function $g(W_k)$. Adding to this, it is also necessary to bear in mind the assumption of a *Fermi-Dirac probability function* that dictates the probability that a state is being occupied by an electron, $f(W)$. Thus, one can say that both carrier densities per unit volume and per unit energy are given by

$$\text{density of electrons:} \quad n(W) = g_C(W)f(W), \tag{3.10}$$

$$\text{density of holes:} \quad p(W) = g_V(W)[1 - f(W)], \tag{3.11}$$

where $g_C(W)$ and $g_V(W)$ are the density of states in the conduction and valence bands, respectively. The function $[1 - f(W)]$ can be perceived as the "vacancy" degree of the available quantic states in the semiconductor.

3.1.8.A The Fermi-Dirac probability function

As it was stated above, the distribution of electrons by the available quantic states obeys the Fermi-Dirac probability function. This happens because, in reality, all the phenomena involving these particles are determined by *Heisenberg's principle of uncertainty* hence the need for probabilistic functions. The Fermi function also abides by Pauli's exclusion principle, which states that it only exists one electron per quantic state, which is can be defined by a determined set of quantum numbers (n, k, l, s).

At the absolute temperature of 0K, the electrons have energies that do not exceed a certain level, designated by the *Fermi level* (W_F). As temperature begins to rise, electrons with higher energies than the Fermi level begin to appear. This evolution is described by the Fermi-Dirac distribution:

$$f(W) = \frac{1}{1 + e^{\frac{W - W_F}{kT}}}, \qquad 0 \leq f(W) \leq 1, \tag{3.12}$$

in which W is the electron energy, W_F the Fermi level, k is the Boltzmann's constant and T the absolute temperature. In Figure 3.10 is shown the plot of $f(n)$ for four different temperatures, n being the transformation $n = W - W_F$.

Regardless of the temperature value, the Fermi function has a value of $f(W) = 1/2$ for the energy equal to the Fermi level $W = W_F$. It has the value of $f(W) = 1$ for values of energy a few times kT below the Fermi level and the value of $f(W) = 0$ for values a few times kT greater than the Fermi level.

One can also simplify expression (3.12) using the Maxwell-Boltzmann approximation, like is shown

in (3.13).

$$W - W_F \gg kT, \qquad f(W) = \frac{1}{1 + e^{\frac{W - W_F}{kT}}} \simeq e^{-\frac{W - W_F}{kT}}. \tag{3.13}$$

This approximation is particularly important for the calculation of the total number of charge carriers in the semiconductor, as will be explained further ahead.

3.1.8.B Density of states

The density of states can be obtained by solving the Schrödinger equation through the infinite potential well model, in which it is assumed that the particles with effective mass m^* can move freely within the two impenetrable boundaries.

Applying the three dimensional model in order to derivate the density of states, one attains the expression for $dN(W_k)$, which represents the number of possible quantic states between the energy levels W_k and $W_k + dW_k$:

$$dN(W_k) = \frac{8\pi V_0}{h^3} m^* \sqrt{2m^* W_k}\, dW_k, \tag{3.14}$$

where V_0 is the assumed volume of the section, h is the Planck's constant and W_k the value of the particle's kinetic energy, which expression is given in (3.1). Thus, the so-called density of states per unit energy is written as

$$g(W_k) = \frac{dN(W_k)}{dW_k} = \frac{8\pi V_0}{h^3} m^* \sqrt{2m^* W_k}. \tag{3.15}$$

Since the particles that are of interest to this work are electrons and holes, the energies to be taken into

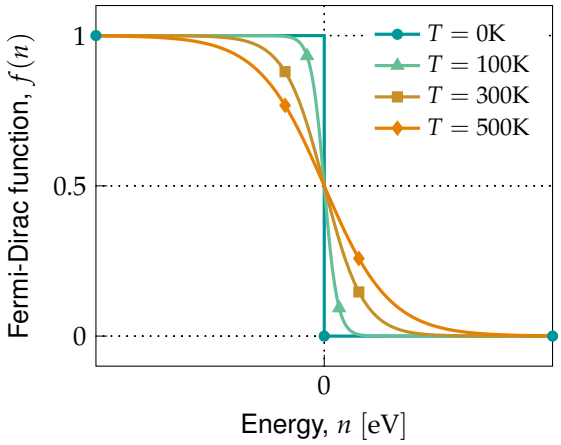

Figure 3.10: The Fermi-Dirac function for several values of temperature.

account are

$$\text{for electrons:} \quad W = W_C + \frac{p^2}{2m_n^*}, \qquad W \geq W_C, \tag{3.16}$$

$$\text{for holes:} \quad W = W_V - \frac{p^2}{2m_p^*}, \qquad W \leq W_C, \tag{3.17}$$

in which m_n^* is the electron's effective mass $(m_n^* = 0.067m_0)$ and m_p^* the hole's effective mass $(m_n^* = 0.5m_0)$. Given that W_k is given by (3.1), the kinetic energy for electrons can be given by $W - W_C$ and for holes $W_V - W$. With this, the expressions for the density of states for both electrons in the conduction band and holes in the valence band are

$$g_C(W) = \frac{8\pi\sqrt{2}V_0}{h^3} m_n^{*3/2} \sqrt{W - W_C}, \tag{3.18}$$

$$g_V(W) = \frac{8\pi\sqrt{2}V_0}{h^3} m_p^{*3/2} \sqrt{W_V - W}. \tag{3.19}$$

One can take both electron density (3.10) and hole density (3.11) expressions, and integrate them, considering the appropriate energy intervals, and thus attaining the expressions for the total number of electrons and holes in the semiconductor:

$$N = \int_{W_C}^{\infty} n(W)dW = \int_{W_C}^{\infty} g_C(W)f(W)dW, \tag{3.20}$$

$$P = \int_{-\infty}^{W_V} p(W)dW = \int_{-\infty}^{W_V} g_V(W)[1 - f(W)]dW, \tag{3.21}$$

substituting $g_C(W)$ and $g_V(W)$ by the expressions previously deducted in (3.18) and (3.19), applying the approximation of Maxwell-Boltzmann (3.13) and, lastly, solving the integrals, one obtains the expressions of both densities $(n = N/V_0,\ p = P/V_0)$ as

$$n = N_C \left(e^{-\frac{W_C - W_F}{kT}} \right), \tag{3.22}$$

$$p = N_V \left(e^{-\frac{W_F - W_V}{kT}} \right), \tag{3.23}$$

where the coefficients N_C and N_V are the *effective density of states* in the conduction and valence bands, respectively, and are defined as

$$N_C = 2\left(\frac{2\pi m_n^* kT}{h^2}\right)^{3/2}, \qquad N_V = 2\left(\frac{2\pi m_p^* kT}{h^2}\right)^{3/2}. \tag{3.24}$$

3.1.9 Carrier transport

The fact that electrons and holes are considered free particles was already mentioned earlier. This means that they are susceptible to the classical processes of *drift* and *diffusion*. Unless the semiconductor is under one of these phenomena, carriers move freely and at random until they collide, be it because of temperature or the collision with atoms, crystal defects, or even with other ions present in

the lattice. It is said then, that there is no net movement of carriers in any direction.

The situations that are of interest regarding solar cells are, naturally, the ones in which an electrical current is being produced. Thus, an extensive study of both drift and diffusion phenomena is essential.

3.1.9.A Transport equations

The drift process happens when the particles present on a semiconductor are subjected to an electrical field. This makes the positively charged particles move in the direction of the applied field and the negatively charged particles move in the opposite direction, creating a current denominated as the *drift current* (I_S). The concept of drift is illustrated in Figure 3.11. To this motion of particles, called the *drift transport*, it is associated an apparently constant *drift velocity* (v_d). Knowing that the drift velocity is directly proportional to the electric field and that $\vec{E} = -\nabla\phi$, one has

$$|\vec{v_\mathrm{d}}| = |\mu\vec{E}| = |\mu\nabla\phi|, \tag{3.25}$$

in which μ is the carrier mobility (further discussed in section 3.1.9.B). Hence, the drift current densities for both electrons and holes are given by

$$\begin{aligned} \vec{J}_n^{\,\mathrm{drift}} &= -qn\vec{v_\mathrm{d}}_n = q\mu_n n\vec{E} = -q\mu_n n\nabla\phi, \\ \vec{J}_p^{\,\mathrm{drift}} &= qp\vec{v_\mathrm{d}}_p = q\mu_p p\vec{E} = -q\mu_p p\nabla\phi. \end{aligned} \tag{3.26}$$

Consequently, the total *drift current density* in the semiconductor is written as

$$\vec{J}_{\mathrm{tot}}^{\,\mathrm{drift}} = \vec{J}_n^{\,\mathrm{drift}} + \vec{J}_p^{\,\mathrm{drift}}, \tag{3.27}$$

$$= q(n\mu_n + p\mu_p)\vec{E}. \tag{3.28}$$

When light irradiates the surface of a solar cell, carriers start to be generated near that surface, creating a carrier concentration gradient throughout the semiconductor. What happens afterward is that

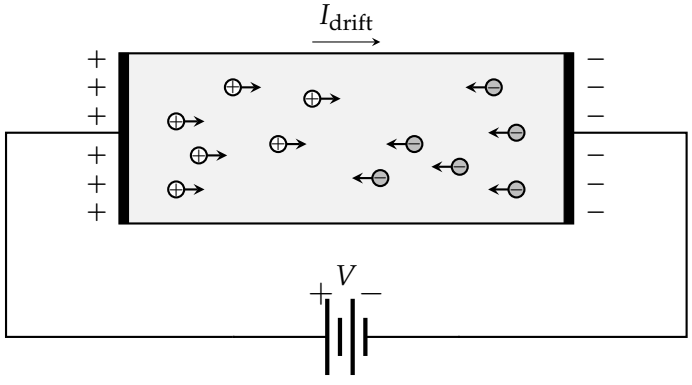

Figure 3.11: Representation of the concept of drift in a semiconductor. Holes move in the direction of the field whilst electrons move in the opposite direction.

carriers start to move from regions of high carrier concentration to regions of low carrier concentration, giving origin to the process denominated as diffusion. This motion results in the creation of electric current, called the *diffusion current* (I_D), as it is shown in Figure 3.12. The diffusion of carriers stops when the concentration is uniform, meaning that carriers will be distributed evenly through space.

In order to evaluate the current density created by diffusion, one can define the *diffusion current density* for both electrons and holes, as follows

$$\begin{aligned} J_n^{\text{diff}} &= qD_n\nabla n, \\ J_p^{\text{diff}} &= -qD_p\nabla p, \end{aligned} \tag{3.29}$$

where D_n and D_p are the diffusion coefficients $[\text{m}^2\ \text{s}^{-1}]$. Using the Einstein relations, that relate the diffusion coefficients with mobilities, one obtains

$$D_n = u_T\mu_n, \qquad D_p = u_T\mu_p, \tag{3.30}$$

in which u_T is the thermal voltage, given by

$$u_T = \frac{kT}{q}, \tag{3.31}$$

in which k is the Boltzmann's constant, T is the absolute temperature and q the electron's charge.

Lastly, having established the current density expressions for both drift and diffusion processes, it is easy to deduct that the total current density for each carrier is given by

$$J_n^{\text{tot}} = J_n^{\text{drift}} + J_n^{\text{diff}}, \tag{3.32}$$

$$J_p^{\text{tot}} = J_p^{\text{drift}} + J_p^{\text{diff}}, \tag{3.33}$$

substituting by the obtained equations 3.26 and 3.29, one attains the expressions that rule carrier transport in a semiconductor, the so-called *transport equations*:

$$\begin{aligned} J_n^{\text{tot}} &= q\mu_n n\nabla\phi + qD_n\nabla n, \\ J_p^{\text{tot}} &= q\mu_p p\nabla\phi - qD_p\nabla p. \end{aligned} \tag{3.34}$$

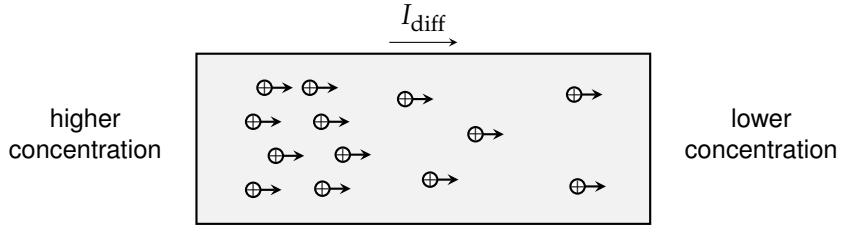

Figure 3.12: Depiction of the phenomenon of diffusion in a semiconductor. Only holes are represented in the Figure. For electrons moving in the same direction, the current would be in inverted.

Another important aspect concerning carrier transport are the evolution of the carriers' densities over time, given by the *continuity equations*. The key factors that have impact in the densities are: the transport processes of drift and diffusion, previously described; and the difference between the generation and recombination rates. Thus, both evolutions for n and p are written as

$$\begin{aligned} \frac{\partial n}{\partial t} &= (G-U)_n + \frac{1}{q}\frac{\partial J_n}{\partial x}, \\ \frac{\partial p}{\partial t} &= (G-U)_p - \frac{1}{q}\frac{\partial J_p}{\partial x}, \end{aligned} \tag{3.35}$$

in which G and U are the generation and recombination terms, respectively.

Bearing in mind that the main aim of this work is the study of solar cells, it is common to assume a steady state and thermal equilibrium. Under these conditions, the carrier densities are the equilibrium carrier concentrations, as it was stated in section 3.1.7. These concentrations do not change over time, therefore one has $\partial n/\partial t = 0$ and $\partial p/\partial t = 0$, giving the following relations

$$\frac{1}{q}\frac{\partial J_n}{\partial x} = -(G-U)_n, \tag{3.36}$$

$$\frac{1}{q}\frac{\partial J_p}{\partial x} = (G-U)_p. \tag{3.37}$$

In conclusion, solving both sets of the transport equations as well as the continuity equations (3.34) and (3.35) gives us a detailed description of semiconductor operation, in particular, if one is interested in obtaining an analytic expression for the current-voltage characteristic when analyzing solar cells.

3.1.9.B Carrier mobility

The notion of *carrier mobility* (μ) $[\mathrm{m^2\,V^{-1}\,s^{-1}}]$ consists in the mean value of the increase in velocity between two consecutive collisions of carriers, in the direction of the applied field when its intensity has the value of $1\ \mathrm{V/m}$. For weak electrical fields, one can say that the carrier mobility is independent of the electric field intensity. The mobilities are different depending on the type of carrier and strongly depend on temperature and on the doping concentration.

The concept of mobility is heavily associated with the drift velocity, since the particles are in the presence of an electric field. When under these circumstances, there is an electric force associated, that can be written as

$$\vec{F}_n = -q\vec{E} \quad \text{for electrons and} \tag{3.38}$$

$$\vec{F}_p = q\vec{E} \quad \text{for holes.} \tag{3.39}$$

As it was seen in the previous section, carriers have random trajectories, accelerating until they collide. The time between two consecutive collisions is defined as the *mean free time*, also known as

scattering time, (τ). In between two collisions, the particles accelerate according to the following relation

$$\vec{v_{\mathrm{d}}} = \frac{\vec{F}}{m^*} t = \frac{\vec{F}}{m^*} \tau. \tag{3.40}$$

Substituting the vector $\vec{F}$ by the expressions (3.38) and (3.39), one has

$$\vec{v_{\mathrm{d}n}} = \frac{-q\tau_n}{m_n^*} \vec{E} \quad \text{for electrons and} \tag{3.41}$$

$$\vec{v_{\mathrm{d}p}} = \frac{q\tau_p}{m_p^*} \vec{E} \quad \text{for holes.} \tag{3.42}$$

Relating these two expressions with equation (3.25), one can attain the expression for both carrier mobilities, given by

$$\mu_n = \frac{q\tau_n}{m_n^*} \quad \text{for electrons and,} \tag{3.43}$$

$$\mu_p = \frac{q\tau_p}{m_p^*} \quad \text{for holes.} \tag{3.44}$$

In Figure 3.13 are shown the hole and electron mobilities as a function of impurity concentration, for both Si and GaAs. It is observable that, independently of the material, the electron mobility is always greater than the hole mobility, $\mu_n > \mu_p$. This is explained by the fact that $\mu \propto {m^*}^{-1}$, as one can deduct by (3.43) and (3.44), and the hole's effective mass is greater than the electron's, $m_p^* > m_n^*$.

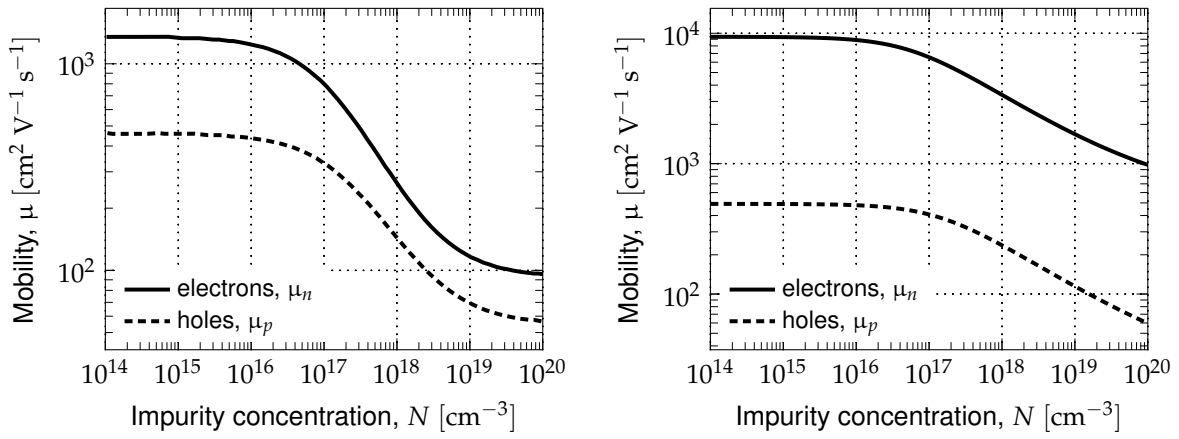

Figure 3.13: Evolution of electron and hole mobilities, at $T = 300\mathrm{K}$, for: (a) Si (in [22], p. 80) and (b) GaAs [23].

With a rise in temperature, the phonon concentration increases, obligating particles to deviate from their original trajectory because of non-uniformities in their passage – this phenomenon is what is called *scattering*. In general, this causes a decline in mobility. However, occasionally, when a semiconductor is heavily doped with impurities, an increase in the low-temperatures range may lead to a rise in mobility, given the fact that there is a decrease in impurity collisions, increasing the scattering time τ and thus increasing mobility μ. All of these effects are shown in Figure 3.14 for both Si and $Ga_{0.47}In_{0.53}As$.

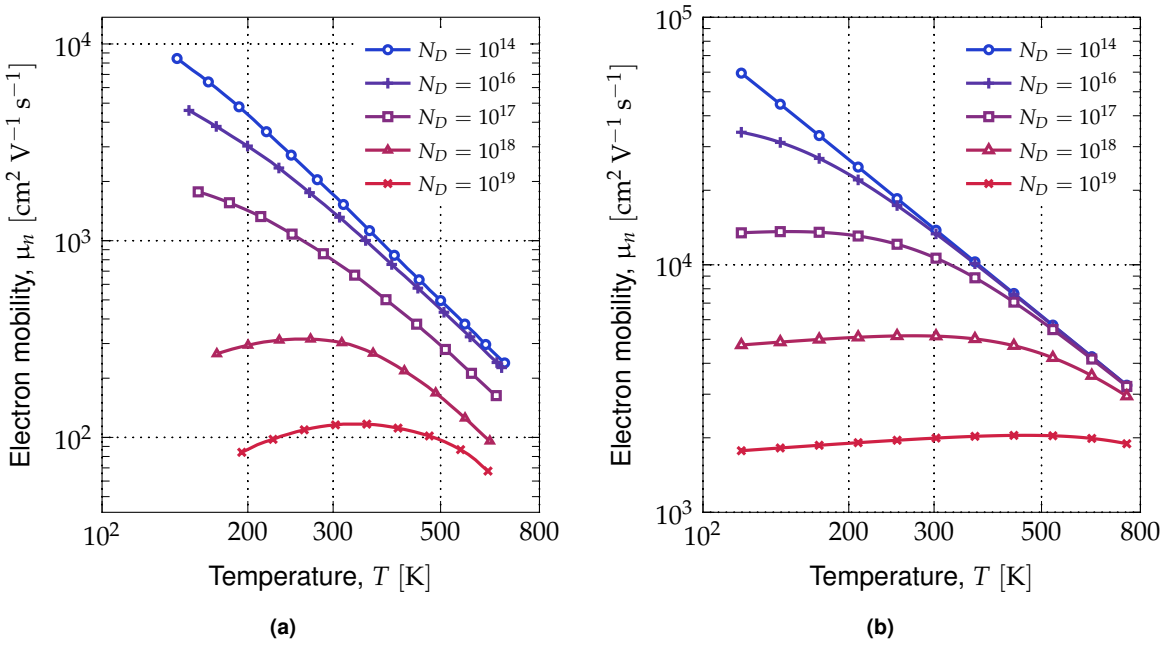

Figure 3.14: Evolutions for electron mobility μ_n as a function of temperature for: (a) n-type Si ([24], p. 222) and (b) n-type $Ga_{0.47}In_{0.53}As$ (fitted curves computed after an empirical low-field model in [23]).

Lastly, another factor that strongly impacts mobility is the impurity concentration in the material. This is due to the fact that the more heavily doped a material is, the more likely that a collision between a carrier and an impurity happens. This reduces the mean free time τ, which in turn reduces the mobility since $\mu \propto \tau$. This is represented in Figure 3.15, where is shown these dependencies for both Si and $Ga_{0.47}In_{0.53}As$.

3.1.10 Carrier generation-recombination processes

As it was already stated in 3.1.2, to a temperature rise it is associated with an increase in the density of charge carriers. This phenomenon is called *generation* and to its inverse process is given the name of *recombination*. In a homogeneous semiconductor at thermodynamic equilibrium, these two mechanisms have equal rates, $G = R$.

These two processes can be classified into *radiative*, in which the transitions to higher or lower levels involve the absorption or emission of a photon, respectively; and *non-radiative*, in which transitions involve energy coming from the lattice in the form of phonons[2].

In the following sections, a detailed definition of the generation-recombination processes will be given, analyzing some pertinent aspects to the simulation of photovoltaic devices, such as the one presented in this work.

[2] a particle analogous to a photon, representing the excitation in a crystal lattice and having the energy of $\hbar\omega$.

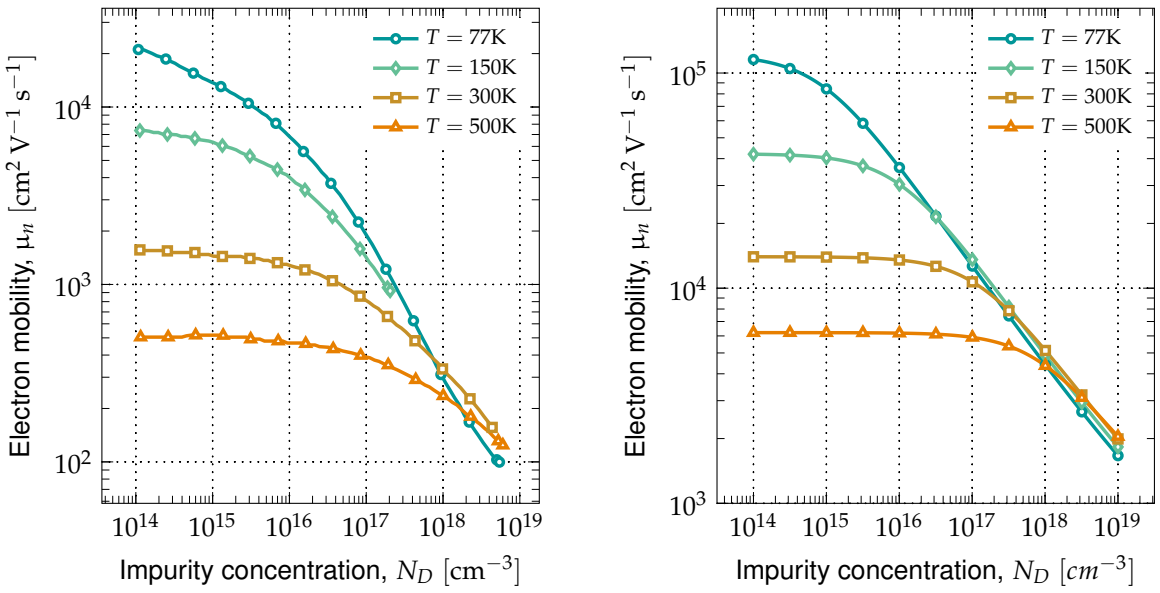

Figure 3.15: Evolutions for electron mobility μ_n as a function of impurity concentrations for: (a) n-type Si ([25]) and (b) n-type $Ga_{0.47}In_{0.53}As$ (fitted curves computed after an empirical low-field model in [23]).

3.1.10.A Generation

The generation process (G) $[\mathrm{m}^{-3}\ \mathrm{s}^{-1}]$ calculates the rate of how many electron-hole pairs are being formed in a volume section of a semiconductor. The principal method of generation in solar cells is the absorption of light through the photoelectric effect.

When a photon hits the surface of a semiconductor material, it will be either reflected, transmitted, or absorbed by the material. The first two processes (reflection and transmission) are considered to be losses since the photon needs to be absorbed to generate power.

The energy of a photon can be calculated through the following relation

$$W_{ph} = h\nu, \tag{3.45}$$

in which h is the Planck's constant and ν is the photon's frequency, that relates with wavelength $\nu = c/\lambda$. With this energy, it is possible to determine what will occur when it falls onto the surface of the semiconductor:

- when $W_{ph} < W_G$, the photon energy is less than the bandgap energy, and so the photon will be transmitted and it will not interact with the semiconductor;
- when $W_{ph} = W_G$, the photon energy is equal to the bandgap energy, resulting in the photon being absorbed efficiently;
- when $W_{ph} > W_G$, the photon energy is greater than the bandgap energy, the photon will be

absorbed however the excess of energy will be dissipated.

The absorption of light in photovoltaic devices will result in a significant increase of photo-generated minority carriers in the semiconductor. In fact, these light-generated minority carriers will be orders of magnitude greater than the already existent minority carriers, thus one can say that the number of minority carriers is approximately the number of photo-generated minority carriers. However, the same does not happen for majority carriers; on the account of doping, the number of majority carriers is immensely higher than the carriers generated by the absorption of light.

3.1.10.A.1 Absorption coefficient

The carrier generation rate in a semiconductor is characterized by the number of electron-hole pairs generated by photon absorption. In a planar section of a thin-layer semiconductor, the generation rate can be given by

$$G(x) = \alpha(\lambda)\phi_0 e^{-\alpha(\lambda)x} \quad [\mathrm{m}^{-3}\,\mathrm{s}^{-1}], \tag{3.46}$$

where ϕ_0 is the photon flux $[\mathrm{m}^{-2}\,\mathrm{s}^{-1}]$ and $\alpha(\lambda)$ $[\mathrm{m}^{-1}]$ is the absorption coefficient on a given wavelength. The absorption coefficient is a characteristic of each semiconductor and a mean to understand how far the light of a specific wavelength can penetrate in the material before it is absorbed. This variable depends on the material and the photon energy that irradiates the material.

In Figure 3.16 are shown a few absorption coefficients for some of the most used materials in solar cell manufacture. It is observable that even when the photon energy is greater than the bandgap, meaning that the photon will be absorbed, the evolution of the absorption coefficient does not have a constant behavior as one could expect. One of the reasons that can explain this is that as the photon's energy becomes greater, the number of electrons that can interact with the photon increases, and so the absorption of photons also increases.

One variable that can be deducted through the absorption coefficient is the absorption depth, which is the inverse of the absorption coefficient $(\alpha^{-1}\ [\mathrm{m}])$, and gives the distance that the photons can traverse into the material before being absorbed. Traditionally, high energy photons have lower absorption depths and the opposite is valid for low energy photons since high energy photons tend to be absorbed near the surface and low energy photons are absorbed throughout the entire material.

3.1.10.B Recombination

With the concept of carrier generation established (see section 3.1.10.A), one must also characterize the inverse phenomenon called *recombination* (R) $[\mathrm{m}^{-3}\,\mathrm{s}^{-1}]$, in which the previously excited electrons recombine with holes making the EHP[3]s disappear. In these transitions from higher into lower energy

[3]electron-hole pair

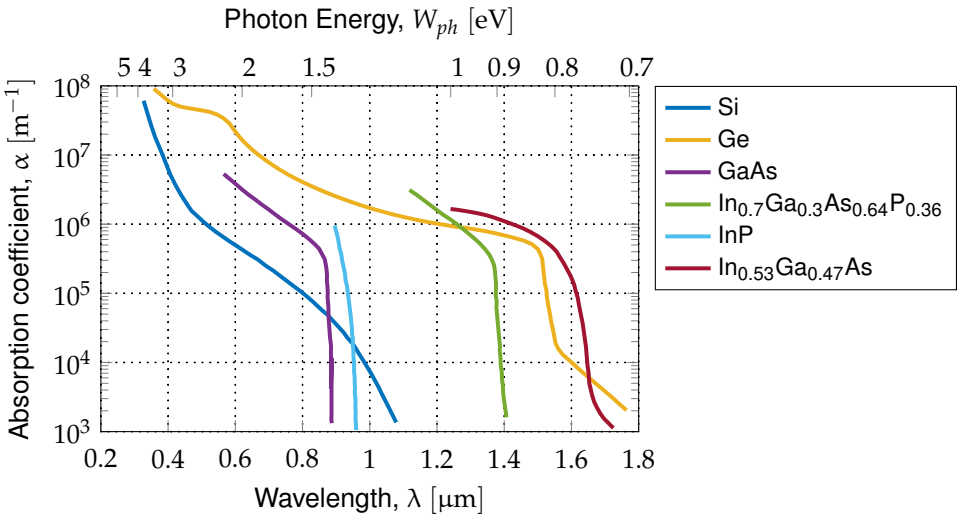

Figure 3.16: Absorption coefficients as a function of wavelength (bottom abscissa axis) or photon energy (top abscissa axis) of several materials used in solar cell manufacture, including III-V materials. Adapted from [26].

states, there is a certain quantum of energy being released, being it in the form of heat or even light (e.g. LED devices).

The process of recombination also varies from material to material, depending on its lifetime and its composition, for example, if it is an intrinsic or extrinsic semiconductor. There are several types of recombination:

- band-to-band or *direct recombination* consists of a radiative process in which the electron recombines with a hole without changing its momentum. This is the dominant way of recombination in direct-gap semiconductors, such as GaAs or InAs.
- band-to-impurity or *indirect recombination* is the main process of recombination in indirect gap semiconductors, like Si or Ge. It occurs due to the intermediate levels close to the band edge in the bandgap that are created by impurities in the crystal lattice. This is often called as the *Shockley-Read-Hall* (SRH) recombination.
- *surface recombination*, as the name suggests, describes the recombination that happens in the surface of the semiconductor as a result of the dangling bonds left by the end of the semiconductor material. In some photovoltaic applications, this is the principal mean of recombination.
- *Auger recombination* which is a three-particle process, where an electron and a hole recombine, kinetically exciting another electron, however, this electron rapidly ends losing its excess of energy to the lattice in the form of phonons. It is a particularly prominent way of recombination in semiconductors with a high carrier concentration, be it by the result of heavy doping of the material or by concentration sunlight (e.g. CPV systems).

3.2 Fundamentals of solar cells

A solar cell is nothing more than a device that converts light energy into electricity. This occurs by means of the photovoltaic effect, where the absorption of light gives origin to an electron-hole pair (as seen in section 3.1.2). This excitation of charge carriers results in their separation, be it by processes of drift or diffusion (see section 3.1.9), and thus creating an electric potential in the device. Therefore, a solar cell is fundamentally a semiconductor diode, that carefully separates charge carriers, converting the energy of the sun into electrical energy. A typical structure of a solar cell that makes use of the p–n junction is illustrated in Figure 3.17.

This semiconductor diode can be defined by certain models and equations, that describe the behavior of a solar cell – it allows one to study certain properties, such as the current-voltage characteristic or cell efficiency, that are of paramount interest when regarding solar cell manufacture.

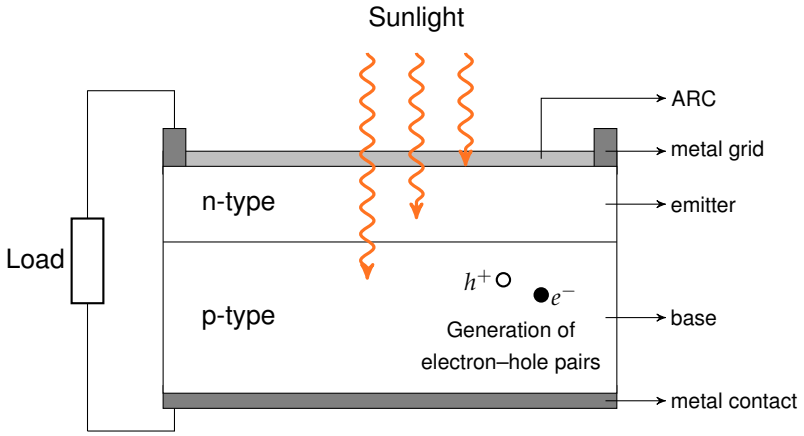

Figure 3.17: Schematic representation of a solar cell, using the p–n junction.

3.2.1 Sunlight spectra

The sun may be one of the greatest sources of energy that is available on our planet – in one day, it irradiates more energy than the world needs in one year. This sunlight can be specified as a function of wavelength, depending on multiple factors, such as altitude, the weather conditions, or the zenith angle (θ_z) that is being considered. This results in several spectral distributions made available by solar simulators, each one relevant for certain photovoltaic applications.

Outside Earth's atmosphere, energy in the form of light falls with a spectral distribution designated *air mass zero* (AM0), mostly used as the reference spectrum for space applications. The AM0 spectrum can be approximated as the one of a blackbody at the absolute temperature of $T = 5777\text{K}$. This approximation is especially accurate in the region of the infrared, as it is shown in Figure 3.18a.

As light approaches the surface of the Earth, some of the radiation located in the ultraviolet and

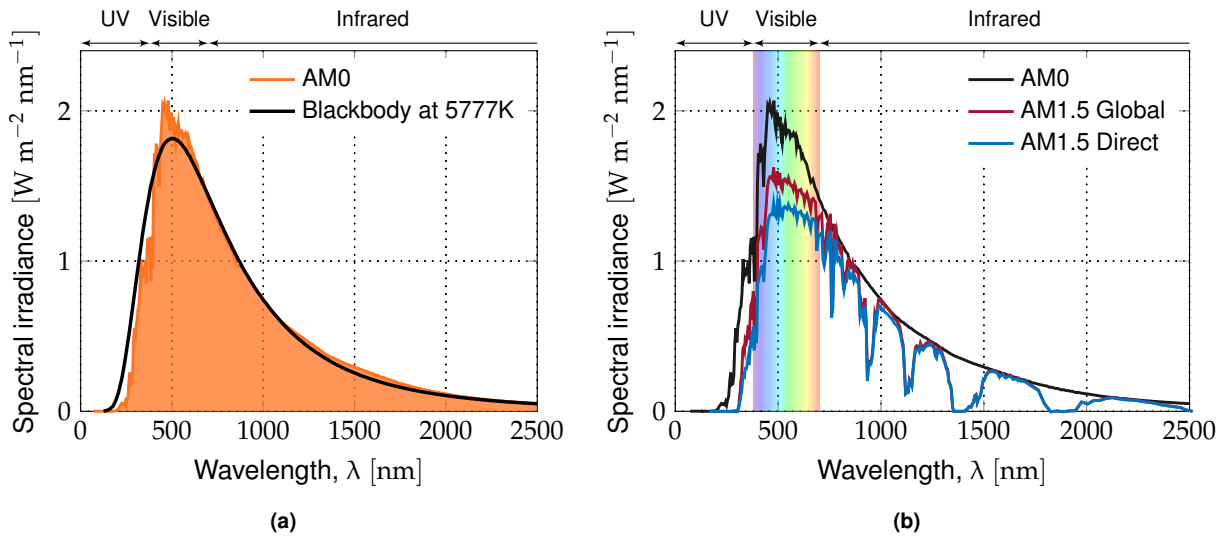

Figure 3.18: Representation of the sun's spectral irradiances: (a) comparison between the emission of a blackbody at $T = 5777\text{K}$ and the solar emission at the top of the atmosphere (AM0); and (b) evolutions of the ASTM G173-03 Reference Spectra distributions (AM0, AM1.5G and AM1.5d), made available by NREL at [27].

visible regions was already absorbed by some of the atmosphere components, attenuating the intensity of the solar spectrum that reaches the Earth. The two most used spectra for terrestrial applications are the *air mass 1.5 global* (AM1.5G), used for flat-plate PV modules, and the *air mass 1.5 direct* (AM1.5d), designed for solar concentrator systems. These two spectra distributions alongside with AM0 are described in Table 3.1 and are represented in Figure 3.18b.

The sunlight spectrum can be divided into three main widely-known wavelength ranges, which will be extensively mentioned in this work. The wide spectrum of sunlight is organized by wavelength range in Table 3.2.

Table 3.1: ASTM G173-03 Reference Spectra, available at [27].

Spectral dist.	Description	Altitude	Zenith θ_z [°]	Incident Power G [W m^{-2}]
AM0	ASTM Standard Extraterrestrial Spectrum	atmosphere	0	1366.1
AM1.5G	ASTM Terrestrial Global 37 Deg. South Facing Tilt	surface	48.2	1000
AM1.5d	ASTM Direct Normal +Circumsolar	surface	48.2	900

Table 3.2: Sunlight spectrum organized by wavelengths. Adapted from [28].

		Range	Description
Ultraviolet (UV)	UVA	$100 - 200\,\text{nm}$	Absorbed by the Earth's atmosphere
	UVB	$280 - 315\,\text{nm}$	90% is absorbed by the Earth's atmosphere
	UVC	$315 - 400\,\text{nm}$	Most of it reaches the terrestrial surface
Visible		$400 - 780\,\text{nm}$	Visible light from violet to red
Infrared (IR)	NIR[a]	$780\,\text{nm} - 3\,\mu\text{m}$	Heat radiation from the sun
	FIR[b]	$3 - 50\,\mu\text{m}$	Heat radiation from several sources other than the sun

[a] Near-Infrared
[b] Far-Infrared

3.2.2 Optical properties

The optical properties of a solar cell are several different aspects that influence the number of photons that can be absorbed by the semiconductor material, and thus also affect the cell's overall efficiency.

When a beam of light falls onto the surface of a semiconductor, depending on its incident angle, the incident photons can either be reflected with an equal angle (Law of refraction: $\theta_i = \theta_r$, where θ_i is the incident angle and θ_r the refracted angle) or they can be refracted (transmitted) inside the material with a smaller angle – this is represented in Figure 3.19 and it is known as the *Snell-Descartes Law*, given by the following expression:

$$\frac{\sin\theta_t}{\sin\theta_i} = \frac{v_2}{v_1} = \frac{n_1}{n_2} = n, \tag{3.47}$$

in which n is the *refractive index*. The refraction index is associated with the material's relative permittivity (ε_r) and with the relative permeability (μ_r), through the following expression

$$n = \sqrt{\varepsilon_r \mu_r}. \tag{3.48}$$

However, when referring to oscillating electromagnetic fields, we have to take into consideration a certain frequency dependence of the polarization, leading to a complex relative permittivity $\underline{\varepsilon}_r$, which in turn implies a complex refractive index $\underline{n}$ that allows for the characterization of losses. The complex refractive index is defined with real and imaginary parts, n and κ, respectively, with the latter being denominated as the *extinction coefficient*, as it is shown below:

$$\underline{n} = n + i\kappa. \tag{3.49}$$

The complex relative permittivity $\underline{\varepsilon}_r$ has real and imaginary parts, ε_r and $\underset{\sim}{\varepsilon}_r$, written as

$$\underline{\varepsilon}_r = \varepsilon_r + i\underset{\sim}{\varepsilon}_r. \tag{3.50}$$

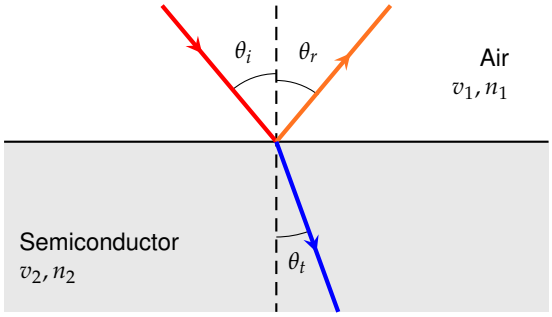

Figure 3.19: Graphic representation of the Snell-Descartes Law and the Law of refraction.

Given that most materials are non-magnetic at optical frequencies, $\mu_r \simeq 1$, and thus one can say that $n = \sqrt{\varepsilon_r}$. Putting together the expressions (3.48), (3.49) and (3.50), one obtains the following relations

$$\underline{\varepsilon}_r = \underline{n}^2 = (n + i\kappa)^2, \tag{3.51}$$

$$\text{where} \quad \varepsilon_r = n^2 - \kappa^2 \tag{3.52}$$

$$\text{and} \quad \underset{\sim}{\varepsilon}_r = 2n\kappa. \tag{3.53}$$

With all of these relations already established, one can now define the relations for the reflection and transmission of light, when it is incident on the boundary of two distinct isotropic media. These relations are denominated as the *Fresnel equations* and can estimate the behavior of the *s-polarized* (electromagnetic field is normal to the plane of incidence) and *p-polarized* (electromagnetic field is parallel to the plane of incidence) electromagnetic waves.

The *reflectivity* (R) (or reflection coefficient) is defined as the portion of the incident power that is reflected from the interface, just as the *transmissivity* (T) (or transmission coefficient), the portion of the incident power that is refracted (transmitted) into the second medium. These two coefficients do not have into consideration attenuation or absorption factors.

Using the Snell's Law, the Law of refraction and considering that the waves' impedances can be determined using just the refractive indexes of both media, one can write the reflectivity R for s-polarized and p-polarized light as

$$R_s = \left| \frac{n_1 \cos\theta_i - n_2 \cos\theta_t}{n_1 \cos\theta_i + n_2 \cos\theta_t} \right|^2 \tag{3.54}$$

$$\text{and} \quad R_p = \left| \frac{n_1 \cos\theta_t - n_2 \cos\theta_i}{n_1 \cos\theta_t + n_2 \cos\theta_i} \right|^2, \tag{3.55}$$

and the transmissivity T as

$$T_s = 1 - R_s, \tag{3.56}$$

$$T_p = 1 - R_p. \tag{3.57}$$

In the event of a perpendicular (normal) incidence of light, one has that $\theta_i = \theta_r = 0$, and so the both expressions (3.54) and (3.55) transform into

$$R = \left| \frac{n_1 - n_2}{n_1 + n_2} \right|^2 . \tag{3.58}$$

After some mathematical manipulation of the expression above, and Using relation (3.47), one can finally write the reflectivity R as a function of the refractive index n and the extinction coefficient κ, as shown below

$$R = \frac{(n-1)^2 + \kappa^2}{(n+1)^2 + \kappa^2}. \tag{3.59}$$

All of these optical properties become very useful when discussing the absorption of light in a photovoltaic device. Clearly, in this devices, it is of major interest to reduce the portion of light that is reflected from the surface of the solar cell – this is why the vast majority of solar cells in the market today, count with a top thin-layer of a dielectric, commonly called the anti-reflection coating (ARC). This anti-reflection coating is characterized by having a refractive index n_{arc} that follows the relation below

$$n_{\text{arc}} = \sqrt{n_1 n_2}. \tag{3.60}$$

There are other techniques for reducing reflection that use several layers of anti-reflection coating, especially for the case of oblique incidence of light. Some of the most known methods for AR[4] are the use of *microgrooves*, in which the light is redirected between grooves to penetrate the material, and the resort to a metallic layer placed in the bottom of the cell, in which the photons that were not absorbed throughout the cell hit the metallic layer, being reflected back into the cell layers.

3.2.3 Electrical characteristics

For better understanding the behavior of certain electrical properties of a solar cell, one resorts to models that can electrically simulate its behavior.

3.2.3.A The ideal solar cell

The ideal solar cell can be modeled by a current source in parallel with a diode, as represented by the model in Figure 3.20. This model is called the 1D3P (1-Diode 3-Parameters) in which the three parameters are (n, I_0, I_{ph}). The relation between current and voltage can be defined by the equation

$$I = I_{ph} - I_0 \left(e^{\frac{V}{nV_T}} - 1 \right), \tag{3.61}$$

[4] anti-reflection

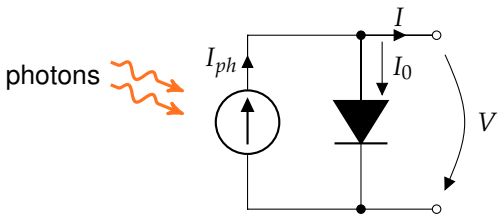

Figure 3.20: Circuit model for an ideal solar cell.

in which I_{ph} is the photovoltaic current, that, in this specific model, is equal to the short-circuit current, $I_{ph} = I_{sc}$, I_0 is the reverse saturation current, V is the voltage, n is the ideality (quality) factor of the diode (ideal diode: $n = 1$, non-ideal diode: $n > 1$) and V_T is the thermal voltage, which expression is given by 3.31. When working under the STC[5] reference conditions, the thermal voltage has a value of $V_T^r = kT^r/q = 0.0257\text{V}$.

The $I - V$ characteristic of the ideal solar cell is exemplified in Figure 3.21a. This curve is an important tool in order to deduct several solar cell parameters, such as the open-circuit voltage V_{oc} and the short-circuit current I_{sc}. The open-circuit voltage V_{oc} can be obtained by substituting the value of the current by zero in equation 3.61. With a little mathematic manipulation, one obtains

$$V_{oc}|_{(I=0)} = nV_T \ln\left(\frac{I_{sc}}{I_0} + 1\right). \tag{3.62}$$

3.2.3.B Maximum Power Point, Fill-factor and Efficiency

The maximum power P_{max} that the cell is capable is producing happens when the voltage and current are equal to V_{mpp} and I_{mpp}, respectively. This point is called the maximum power point and it happens when the power is in its peak, at STC reference conditions, as is shown in Figure 3.21b.

From the concept of *maximum power point* (V_{mpp}, I_{mpp}), it is defined what is called the *fill-factor* FF, defined graphically by being the rectangle under the $I - V$ characteristic with maximum area. It can be given by the following expression

$$FF = \frac{P_{max}}{V_{oc}I_{sc}} = \frac{V_{mpp}I_{mpp}}{V_{oc}I_{sc}} \tag{3.63}$$

Finally, the efficiency of the solar cell can be defined by the relation between the peak power and the irradiance power that is available, and it is written as

$$\eta = \frac{P_p}{AG} = \frac{V_{mpp}I_{mpp}}{AG}, \tag{3.64}$$

where A is the area of the cell and G is the irradiance.

[5]Standard Test Conditions

3.2.3.C Non-ideal model: 1D5P

Alas, in reality, no device has an ideal behavior. There are always losses that must be taken into account when studying circuits, and solar cells are no exception. To simulate the behavior of a solar cell when under realistic conditions, it is usual to rely on solar cell models that can simulate losses. One of those models is the the 1D5P (1-Diode 5-Parameters), represented in Figure 3.23, with the five parameters being n, R_s, R_{sh}, I_0 and I_s.

The relation between current and voltage for this model can be defined by the expression

$$I = I_{sc} - I_0 \left(e^{\frac{V+IR_s}{nV_T}} - 1 \right) - \frac{V + IR_s}{R_{sh}}. \tag{3.65}$$

As one can observe by the expression (3.65), this model resorts to parasitic resistances, a series resistance R_s and a shunt resistance R_{sh}, that reduce the fill-factor, and thus the overall efficiency of the cell. This effect is easily observed by analyzing the $I - V$ characteristic of non-ideal solar cells. The effect of a series resistance can be perceived by varying the value of R_s, maintaining the R_{sh} value constant, as illustrated in Figure 3.23a. Analogously, the effect of a shunt resistance can be noted by varying R_{sh} while maintaining R_s constant, as shown in Figure 3.23b.

3.2.3.D Quantum Efficiency

The quantum efficiency, $\mathrm{QE}(\lambda)$, evaluates a device's sensitivity to light, in the way that it represents the ration of produced electrons by an incident photon of a given wavelength, λ. There are the internal quantum efficiency, $\mathrm{IQE}(\lambda)$, that only considers photons that are not reflected, and so enter the semiconductor material, and the external quantum efficiency, $\mathrm{EQE}(\lambda)$, that takes into account all the incident

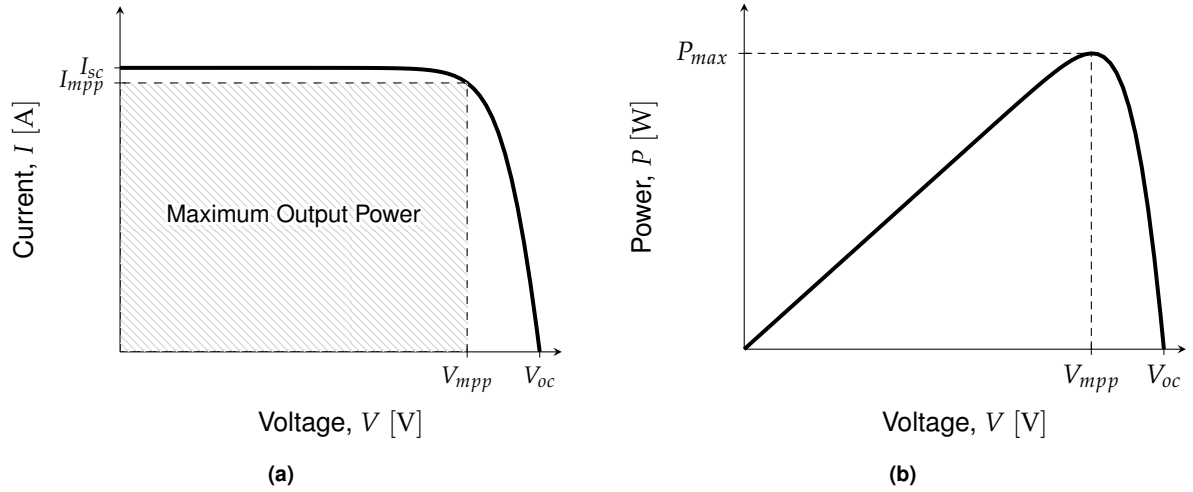

Figure 3.21: Characteristic curves for the 1D3P model and representation of the MPP in: (a) the $I - V$ curve, and (b) the $P - V$ curve.

photons.

Hence, the quantum efficiency of a solar cell can be calculated by the following expression

$$\mathrm{QE}(\lambda) = \frac{N_e}{N_\nu}, \tag{3.66}$$

in which N_e is the number of electrons produced and N_ν is the number of photons absorbed. These two variables can be computed through the expressions

$$\frac{N_e}{t} = \Phi_\xi \frac{\lambda}{hc} \tag{3.67}$$

$$\frac{N_\nu}{t} = \Phi_0 \frac{\lambda}{hc}, \tag{3.68}$$

where t is the time unit $[\mathrm{s}]$, Φ_ξ is the power absorbed in depletion layer $[\mathrm{W}]$, Φ_0 is the incident power $[\mathrm{W}]$, λ is the given wavelength $[\mu\mathrm{m}]$, h is the Planck's constant and c is the speed of light in vacuum. Having the $\mathrm{IQE}(\lambda)$, one can compute the photo-generated current, I_{ph}, in the solar cell, by doing

$$I_{ph} = q \int_\lambda^\Phi \lambda[1 - R(\lambda)] \cdot \mathrm{IQE}(\lambda)\, d\lambda, \tag{3.69}$$

in which Φ is the incident photon flux and $R(\lambda)$ $[\mathrm{A/W}]$ the reflection coefficient.

3.2.3.D.1 Spectral response

The spectral response $\mathrm{SR}(\lambda)$ $[\mathrm{A/W}]$ measures the current generated in the solar cell, I_{ph}, per photon of a given wavelength. It relates to the quantum efficiency trough the expression

$$\mathrm{SR}(\lambda) = \frac{q\lambda}{hc}\mathrm{QE}(\lambda). \tag{3.70}$$

3.2.4 Irradiance and temperature influence

Like any other semiconductor device, solar cells are sensitive to temperature. A temperature rise influences most semiconductor properties, and its effect on solar cells is visible when analyzing the $I - V$ characteristic.

In Figure 3.24a, one can note that when the temperature increases, the open-circuit voltage V_{oc}

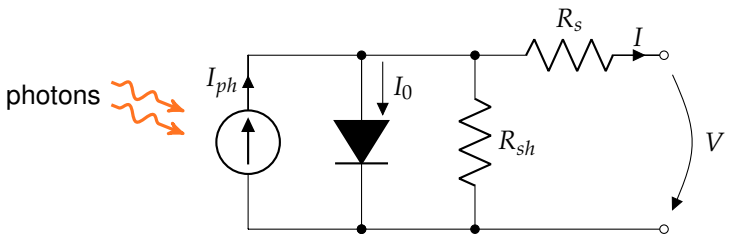

Figure 3.22: Circuit model for a solar cell, including the non-ideal components, R_s and R_{sh}.

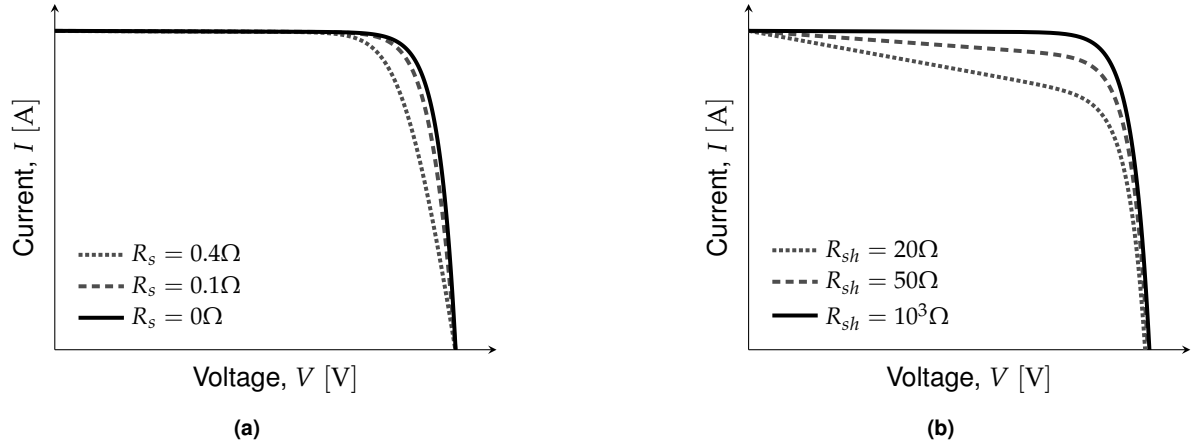

Figure 3.23: The influence of parasitic resistances on $I - V$ curves: (a) for several values of the series resistance, R_s, and (b) for several values of the shunt resistance, R_{sh}.

decreases considerably and the short-circuit current I_{sc} increases insignificantly. With this, it can be easily deduced that the fill-factor decreases, which means that the maximum output power and thus the efficiency also decrease as temperature rises.

As one could expect, the light intensity also plays an important part in influencing the short-circuit current and the open-circuit voltage, and thus the cell efficiency. In solar cell manufacture, one refers to the light intensity that falls on the surface of the solar cell commonly as the number of suns, where the standard intensity is $1000\ \mathrm{W\,m^{-2}}$, also referred as to $1\ \mathrm{sun}$, under the $\mathrm{AM1.5G}$ spectrum. When a PV module is said to operate under $1\ \mathrm{sun}$, it is called a flat plate module, while CPV systems use concentrated sunlight (e.g. some concentrator systems operate at $100\ \mathrm{suns}$).

Analyzing Figure 3.24b, it is noticeable that as irradiance increases, the open-circuit voltage V_{oc} varies slightly, whereas the short-circuit current I_{sc} noticeably increases. Therefore, one can deduct that the output power increases as irradiance increases.

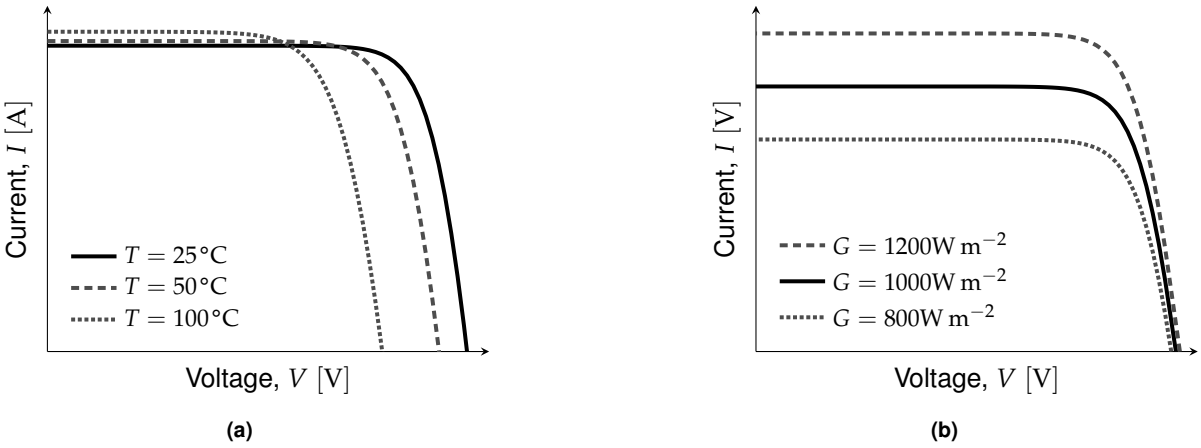

Figure 3.24: Representation of $I - V$ characteristics for: (a) several temperatures, with a constant irradiance value of $1000\mathrm{W\,m^{-2}}$, and (b) several values of irradiance, with a constant temperature of $298.15\mathrm{K}$.

CHAPTER 4

Simulations

4.1 Simulation Software – Silvaco© ATLAS

For the purpose of simulating the III-V solar cell, the software that was chosen was ATLAS, from Silvaco© TCAD simulation applications. ATLAS is a software that enables physically-based 2D and 3D simulations of semiconductor devices by providing a large set of physical models for device simulation. The physical models[1] that ATLAS offers that are most pertinent in the specific case of solar cell analysis, and thus essential for this work, were:

- Drift-diffusion transport models;
- Graded and abrupt heterojunctions;
- Optoelectronic interactions with general ray tracing;
- Stimulated emission and radiation;
- Fermi-Dirac and Boltzmann statistics;
- Heavy doping effects;
- Full acceptor and donor trap dynamics;
- Ohmic, Schottky, and insulating contacts.;
- SRH, radiative, Auger, and surface recombination;
- Impact ionization (local and non-local);
- Floating gates;
- Band-to-band tunneling;

[1] directly taken from ATLAS User's Manual [29], p. 20

- Quantum transport models;
- Thermionic emission currents.

For running ATLAS however, other softwares from Silvaco, the so-called INTERACTIVE TOOLS, are required. These tools have the function of interacting with the Silvaco TCAD applications. In this work, only the ATLAS device simulator was required, nonetheless, Silvaco has other simulators available like ATHENA or VICTORY, each one for different purposes, as it is displayed in Figure 4.1. The INTERACTIVE TOOLS used in this work were DECKBUILD, the run-time editor used for writing the code that runs ATLAS, integrated with an iteration console, and TONYPLOT, which is the interactive visualization tool.

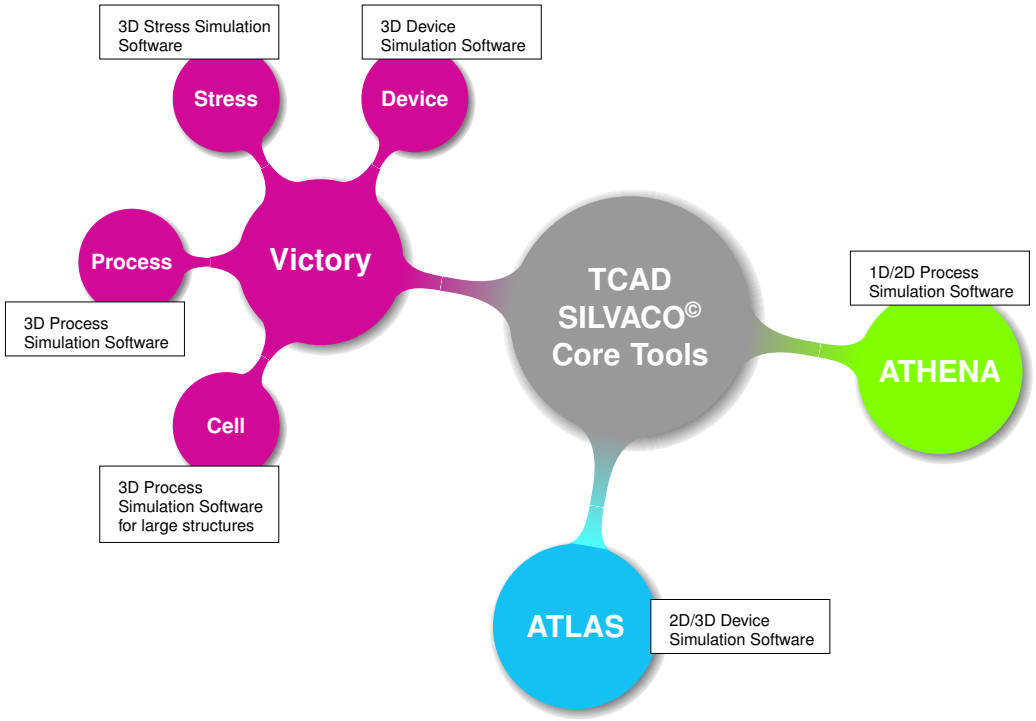

Figure 4.1: Silvaco© TCAD suite of applications for simulation.

4.1.1 Writing an input file in ATLAS

The ATLAS syntax has a variety of commands that belong in specific groups that have to follow a certain order in the file, like Figure 4.2 describes. The input file is nothing more than a sequence of statements, each one identifying a parameter and then setting its value. Values can be real, integer, characters, or logical. The majority of values used for the simulations were either integers or real. The input file has the extension .in and it runs in DECKBUILD.

The input file starts with calling ATLAS with the command `go atlas`, and then the variables statement should come next, with the command `set` followed by the name of the variable with the respective value

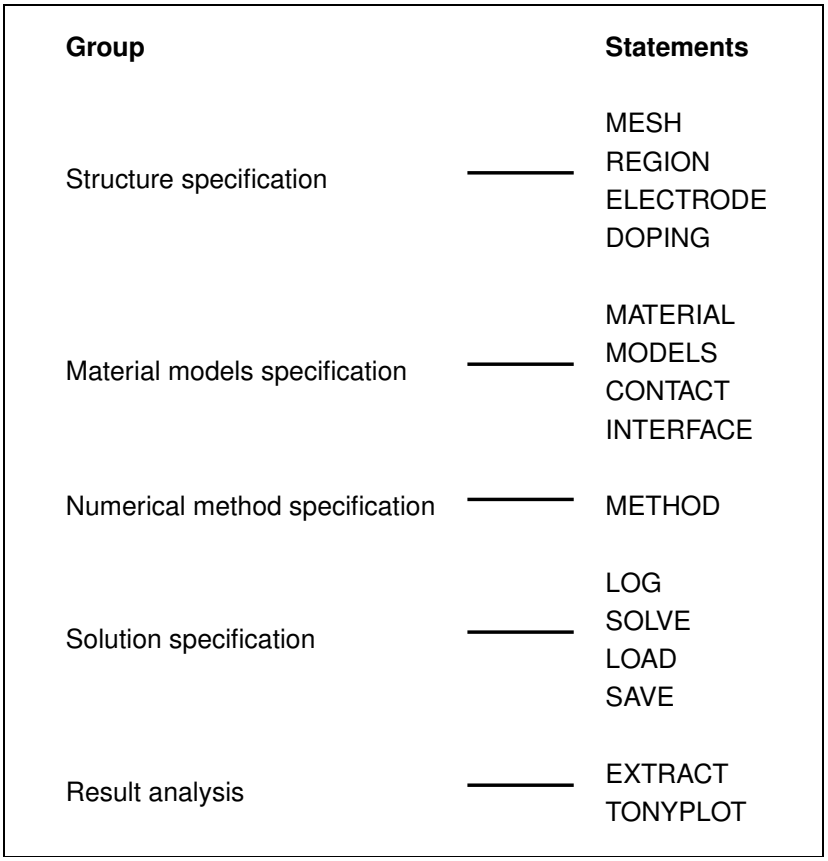

Figure 4.2: Command groups in ATLAS, with the primary statements associated (taken from [29], p. 30).

attribution, so that the file has easy readability. The first lines of the file should have a similar aspect to this:

Listing 4.1: ATLAS syntax example: beginning of the .in file.

```
1 go atlas
2
3 set temperature=300
4 set dop_base=1E17
```

After running ATLAS, the program then expects a sequence of statements for the structure specification. Starting with the mesh used for the simulation of the device under study. In the particular case of this thesis, the device is a solar cell with a considerable amount of layers, each one needing a fine meshing near the junction with the one above and below it. It's also necessary to take a thin mesh around the area where the light beam is going to fall onto the device.

The mesh is done for the x-axis, with the statement `x.mesh loc`, and the y-axis, the statement `y.mesh loc`, for 2D device simulations. The number of divisions for the mesh is specified by the statement `spac`.

The following code describes a device with $1\mu m$ of width (x-axis) and length (z-axis) and $1\mu m$ of height (y-axis), with two layers stacked on top of each other, each one with a thickness of $0.5\mu m$.

Listing 4.2: ATLAS syntax example: MESH definition.

```
mesh width=1      # defining the length

x.mesh loc=0      spac=0.2    # example of X-MESH
x.mesh loc=1      spac=0.2

y.mesh loc=0      spac=0.001
y.mesh loc=0.5    spac=0.1    # Y-MESH 1st layer
y.mesh loc=1      spac=0.1    # Y-MESH 2nd layer
```

An exemplary mesh for the triple-junction LM simulation is shown in Figure 4.3, in which the high line density near critical areas, such as the junctions between two subcells, is fairly visible. Mesh grids influence the accuracy, time, and convergence of the simulation, and so have to establish a compromise between the number of generated nodes and computational power.

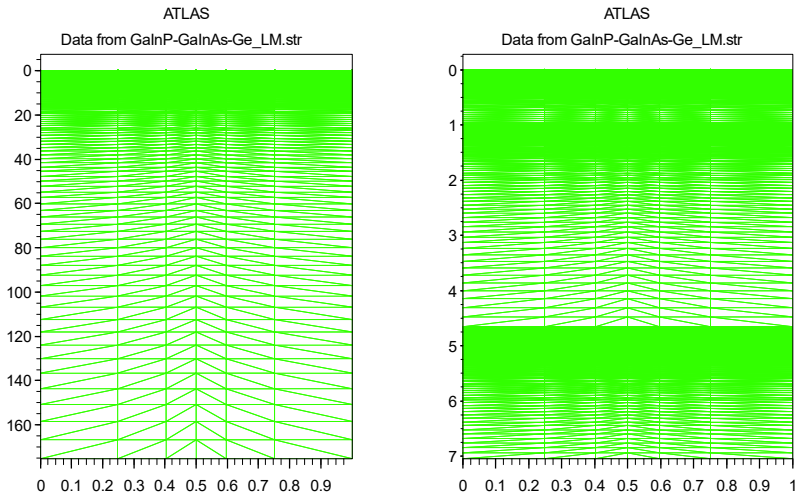

Figure 4.3: MESH utilized for the stacked cell simulation: (a) entire mesh and (b) zoomed out, so that top and middle cell meshes can be distinguished. Both the x- and y-axis are in microns.

After defining the mesh, the program expects the statements of region, electrodes and doping, in that particular order. Picking up the example of Listing 4.2, let one define the two layers, one being the p-region and one the n-region, with the cathode on top of the n-region and cathode below the p-region, each one with a doping of $1 \times 10^{17}\,\mathrm{cm}^{-3}$. The rest of the structure specification is done like Listing 4.3 shows.

Listing 4.3: ATLAS syntax example: rest of the structure definition.

```
region num=1 material=Ge  x.min=0 x.max=1   y.min=0   y.max=0.5
region num=2 material=Ge  x.min=0 x.max=1   y.min=0.5   y.max=1

electrode num=1 name=cathode top
electrode num=2 name=anode bottom

doping uniform region=1 n.type conc=1e17
doping uniform region=2 p.type conc=1e17
```

With the structure of the device established, next comes the material and model specification. The Silvaco library itself has already a great number of default values for most semiconductors/insulators, however, it is always advised to specify the most important properties for the materials that are used in the simulation. One of those properties is the refractive index of each material, that has to be defined, be it by using the sopra database that has both n and κ specified, or by a .nk file that can be created by the user. Either way, this must be stated in the .in file.

The models that are implement may vary from simulation to simulation, depending on what the simulation requires. For a solar device to run, the most common models to implement are presented in Table 4.1, in which it is possible to see the name, syntax, and brief description of each model.

Table 4.1: The most important models for solar cell simulation in ATLAS (directly taken from [29]).

Models	Syntax	Description
CARRIER STATISTICS MODELS		
Fermi-Dirac	FERMI	Carrier concentrations in heavily doped regions.
Bandgap Narrowing	BGN	Important in heavily doped regions.
Incomplete Ionization	INCOMPLETE	Accounts for dopant freeze-out.
MOBILITY MODELS		
Concentration Dependent	CONMOB	Simple power law temperature dependence (GaAs only).
Concentration and Temperature Dependent	ANALYTIC	Caughey-Thomas formula (for 77 to 450K).
RECOMBINATION MODELS		
Shockley-Read-Hall	SRH	Uses fixed minority carrier lifetimes.
Auger	AUGER	Direct transition of three carriers.
Optical	OPTR	Band-band recombination (direct materials only).
TUNNELING MODELS		
Band-to-Band (standard)	BBT.STD	Used for direct transitions.
Trap-Assisted Tunneling	TRAP.TUNNEL	Trap-to-band phonon-assisted tunneling effects.

An example of how the models and material specification is done is displayed below in Listing 4.4, in which the property specification for germanium is made, along with all the relevant models employed.

Listing 4.4: ATLAS syntax example: material and models specification.

```
# Refractive index
material material=Germanium    sopra=Ge.nk

# Properties of Ge
material material=Ge ALATTICE=5.658 EG300=0.661 PERMITTIVITY=16.2 \
          \ AFFINITY=4
material material=Ge MUN=3900 MUP=1800
material material=Ge NC300=1.0e19 NV300=5e18
material material=Ge TAUN=1E-3 TAUP=1E-3 AUGN=1e-30 AUGP=1e-30 \
          \ COPT=6.41E-14

# Models statement
models srh auger optr fermi bgn temperature=300
```

The numerical methods utilized are usually the next statement, where there are no contacts or interfaces to be defined. In this work, all the simulations performed resorted to both Newton and Gummel methods for convergence. This is done by adding the line `methods newton gummel` to the program.

Finally, with all the first steps completed, the next and final stage of the .in file is to indicate the desired plots/parameters that are going to be extracted. Since this is a simulation of a solar cell, the definition of a light beam to fall onto the device is also required. The beam can have a specific wavelength defined, or a whole solar spectrum can be appointed to the photon beam, like the AM1.5G or AM0. Silvaco has both spectra in its library that can be called by using the `AM1.5` or `AM0` statements on the `beam` command, or it lets the user to upload a .spec file, with a personalized spectrum. The angle of incidence and the starting and ending wavelength values of the beam can also be defined, along with the number of points desired. This is important since ATLAS will then start `BLAZE` and `LUMINOUS` modules to perform a 2D ray tracing of the power spectrum.

The solution is obtained by using the `solve` statements, firstly by ramping up the beam intensity of incidence on the device, and then by solving for different voltage values, so that the $I - V$ characteristic can be obtained. Lastly, all the significant parameters are extracted from the solution file (.log file), applying the `extract` commands.

An exemplary ATLAS syntax on how to execute the beam and solution commands is presented in Listing 4.5. The simulations that were executed on this thesis follow this structure. The `extract` statements for parameters such as the short-circuit current, I_{sc}, and open-circuit voltage, V_{oc}, were taken by some examples made available by Silvaco for solar devices.

Listing 4.5: ATLAS syntax example: beam and solution statements, along with parameter extraction.

```
# Beam statement
beam num=1 y.o=-0.5 x.o=0.5 angle=90 wavel.start=0.1 wavel.end=3.55
    wavel.num=800 power.file=am0.spec

# Ramping up the beam intensity (for convergence)
solve init
solve b1=1e-02
solve b1=1e-01
solve b1=1

# Solution file
log outf=IV_solarcell.log

# Solving for different voltage values (I-V curve)
solve vanode=0
solve name=anode vstep=0.005 vfinal=0.5

# Extracting parameters from the solution file
extract init infile="IV_solarcell.log"
extract name="JV" curve(v."anode", i."cathode") outfile="
    IV_solarcell.dat"
extract name="Jsc" y.val from curve(v."anode", i."cathode") where
    x.val=0.0
extract name="Voc" x.val from curve(v."anode", i."cathode") where
    y.val=0.0
extract name="Pm" max(curve(v."anode", (v."anode" * i."cathode")))
extract name="Vm" x.val from curve(v."anode", (v."anode"*i."cathode")
    ) where y.val=$"Pm"
extract name="Im" $"Pm" / $"Vm"
extract name="FF" ($"Pm" / ($"Jsc"*$"Voc" ))*100
extract name="Opt_int" max(beam."1")
extract name="Eff" ($"Pm" / $"Opt_int")*100
```

4.2 Material Properties

With focus on simulating III-V MJSC[2] behavior, extensive research had to be made, since these cells have a vast number of different materials. This was quite essential, since the Silvaco library is somewhat limited, not possessing some properties required for the models used in the simulation (refer to section 4.1), and, for some materials, is not updated after the latest published scientific research.

Consulting the Atlas User Manual [29], the properties that have to be specified for good model accuracy are listed below, followed by their notation in Silvaco© ATLAS.

General properties

- Bandgap, E_g at $300\,\mathrm{K}$ (`EG300`);
- Lattice constant, α (`ALATTICE`);
- Electron affinity, χ (`AFFINITY`);
- Relative permittivity, ε_r (`PERMITTIVITY`);
- Electron mobility, μ_n (`MUN`), and hole mobility μ_p (`MUP`);
- Effective conduction, N_C (`NC300`), and valence, N_V (`NV300`), bands density of states at $300\,\mathrm{K}$;
- Refractive coefficient has a function of wavelength, $n(\lambda)$ and $\kappa(\lambda)$ (`.nk files`);

Recombination parameters

- Electron lifetime, τ_n (`TAUN`), and hole lifetime, τ_p (`TAUP`);
- Auger coefficients for electrons, C_n (`AUGN`), and holes C_p (`AUGP`);
- Radiative recombination coefficient, C_{OPT} (`COPT`)

The majority of these values can be encountered in a vast amount of scientific papers. There are some websites from institutes and companies that assemble results that were published, and make their databases available for consultation online, such are the cases of Ioffe Institute at [30] and MatWeb's data at [31].

4.2.1 III-V binary properties

The general properties that were utilized for Ge and the binaries relevant to this work are presented in Table 4.2. Unless stated otherwise, the properties are all at the temperature of $T = 300\,\mathrm{K}$. The refractive indexes are not shown, since they are a function of wavelength, but they will be presented further ahead for the most relevant materials.

[2] multi-junction solar cell

Table 4.2: General properties used for Ge and III-V Phosphides and Arsenides binaries, at $T = 300\,\mathrm{K}$.

Material	**Lattice constant** α [Å]	**Bandgap** E_g [eV]	**Electron Affinity** χ [eV]	**Rel. Permittivity** $\varepsilon_r \left(\frac{\varepsilon}{\varepsilon_0}\right)$	**Electron Mobility** μ_n [$\mathrm{cm^2/(V\,s)}$]	**Hole Mobility** μ_p [$\mathrm{cm^2/(V\,s)}$]	**Conduction band DOS*** N_C [$\mathrm{cm^{-3}}$]	**Valence band DOS*** N_V [$\mathrm{cm^{-3}}$]
Ge	5.658	0.661	4.0	16.2	3900	1900	$1 \cdot 10^{19}$	$5 \cdot 10^{18}$
GaAs	5.653	1.424	4.07	12.9	8500	400	$4.7 \cdot 10^{17}$	$9 \cdot 10^{18}$
InAs	6.0583	0.354	4.9	15.15	$4 \cdot 10^4$	500	$8.7 \cdot 10^{16}$	$6.6 \cdot 10^{18}$
GaP	5.4505	2.26	3.8	11.1	250	150	$1.8 \cdot 10^{19}$	$1.9 \cdot 10^{19}$
InP	5.8687	1.344	4.38	12.5	5400	200	$5.7 \cdot 10^{17}$	$1.1 \cdot 10^{19}$
AlAs	5.6622	2.168	2.62	10.06	200	100	$1.5 \cdot 10^{19}$	$1.7 \cdot 10^{19}$
AlP	5.451	2.45	3.98	9.6	80	450	$2 \cdot 10^{19}$	$1.5 \cdot 10^{19}$

*density of states

Recombination parameters are presented in Table 4.3. All the values presented were from Ioffe's Institute database. Both binaries AlAs and AlP are not shown given the lack of published research on these materials' recombination properties.

Table 4.3: Recombination parameters used for Ge and III-V Phosphides and Arsenides binaries, at $T = 300\,\mathrm{K}$.

Material	**Electron lifetime** τ_n [s]	**Hole lifetime** τ_n [s]	**Auger coefficient** C_{Aug} [$\mathrm{cm^6/s}$]	**Radiative Recombination coefficient** C_{OPT} [$\mathrm{cm^3/s}$]
Ge	$1 \cdot 10^{-3}$	$1 \cdot 10^{-3}$	$1 \cdot 10^{-30}$	$6.41 \cdot 10^{-14}$
GaAs	$5 \cdot 10^{-9}$	$3 \cdot 10^{-6}$	$1 \cdot 10^{-30}$	$7.2 \cdot 10^{-10}$
InAs	$3 \cdot 10^{-8}$	$3 \cdot 10^{-6}$	$2.2 \cdot 10^{-27}$	$1.1 \cdot 10^{-10}$
GaP	$1 \cdot 10^{-7}$	$1 \cdot 10^{-7}$	$1 \cdot 10^{-30}$	$1 \cdot 10^{-13}$
InP	$2 \cdot 10^{-9}$	$3 \cdot 10^{-6}$	$9 \cdot 10^{-31}$	$1.2 \cdot 10^{-10}$

4.2.2 III-V ternary and quaternary properties

Nonetheless, the majority of the materials utilized in the simulation will be III-V ternary and quaternary compounds, and although at the time this work is being written there is quite an extensive literature regarding these alloys, some of the properties have not yet reached consensus in the scientific commu-

nity and thus are not yet available for online consultation in the main databases.

4.2.2.A Interpolation schemes for III-V compounds

Some of the properties will, then, be deduced by employing heuristic methods, such as the rules for property variation of a ternary/quaternary with compositions x and y, stated previously in Chapter 3, section 3.1.5.A. Although it may work for some direct band binaries, such as GaAs, InAs, and InP, these rules do not provide an accurate estimation of parameters for indirect band materials. To overcome this hindrance, the *Vergard's Law* for ternary compounds, which consists in a heuristic approach, will be applied.

One specific example is the bandgap, E_g, that does not vary linearly with composition. For a ternary compound, the Vergard's Law is written as follows

$$E_g^{A_xB_{1-x}C} = xE_g^{AC} + (1-x)E_g^{BC} + C_g(1-x)x, \tag{4.1}$$

where x is the composition, E_g the bandgap and C_g is the empirical bowing parameter, that applies a curvature correction to the interpolation. This method was very useful for the calculation of the $Ga_xIn_{1-x}P$, $Al_xIn_{1-x}As$ and $Al_xIn_{1-x}P$ bandgaps, for which there is limited literature.

4.2.2.B Composition versus lattice-matched alloys

When discussing a lattice-matched monolithic cell structure, it was already asserted the need for the materials to have the nearly same lattice constant. Since the main aim of this work is the simulation of a GaInP/GaInAs/Ge MJSC, it is essential for all the constituent materials of the cell to match the Ge lattice constant, $\alpha_{\mathrm{Ge}} = 5.658\,\text{Å}$. Knowing that the lattice constant α varies linearly with composition (refer to Chapter 3, section 3.1.5.A). Since the objective is simply matching the lattice constants of the ternaries with the Ge lattice constant, $\alpha_{A_xB_{1-x}C} = \alpha_{\mathrm{Ge}}$, applying relation (3.2), one can write

$$\alpha_{A_xB_{1-x}C} = \alpha_{\mathrm{Ge}} = x\alpha_{AC} + (1-x)\alpha_{BC}. \tag{4.2}$$

With this, one can know exactly the ternary compositions required for the lattice-matched approach, given by

$$x = \frac{\alpha_{\mathrm{Ge}} - \alpha_{BC}}{\alpha_{AC} - \alpha_{BC}}. \tag{4.3}$$

Utilizing this expression, it was possible to compute the necessary alloy compositions x, appropriate for the LM[3] GaInP/GaInAs/Ge cell. Those compositions are listed in Table 4.5.

[3]Lattice-matched

Table 4.4: Compositions x for several alloys, lattice-matched to Ge, $\alpha_{\mathrm{Ge}} = 5.658\,\text{Å}$.

Composition	$Al_xGa_{1-x}As$	$Al_xIn_{1-x}P$	$Ga_xIn_{1-x}As$	$Ga_xIn_{1-x}P$
x	0.54	0.50	0.99	0.50

As for the quaternary AlGaInP, the composition was based on the work of Adachi [32], which demonstrates the possible mole fractions for this compound.

Table 4.5: Compositions x for several alloys, lattice-matched to Ge, $\alpha_{\mathrm{Ge}} = 5.658\,\text{Å}$.

Composition	$Al_xGa_{1-x}As$	$Al_xIn_{1-x}P$	$Ga_xIn_{1-x}As$	$Ga_xIn_{1-x}P$
x	0.54	0.50	0.99	0.50

Using the databases and research available, along with Vergard's Law (4.1), one can then compute the general properties of the ternaries that will be utilized for simulation. The values are listed in Table 4.6. Some properties could not be found or deduced accurately, such as the recombination parameters for the ternaries. In this case, the Silvaco ATLAS material library will be resorted to.

Table 4.6: General properties used for III-V ternaries and quaternary, at $T = 300\,\text{K}$.

Material	**Lattice constant** α [Å]	**Bandgap** E_g [eV]	**Electron Affinity** χ [eV]	**Rel. Permittivity** $\varepsilon_r \left(\frac{\varepsilon}{\varepsilon_0}\right)$	**Electron Mobility** $\mu_n\,[\mathrm{cm}^2/(\mathrm{V\,s})]$	**Hole Mobility** $\mu_p\,[\mathrm{cm}^2/(\mathrm{V\,s})]$	**Conduction band DOS*** $N_C\,[\mathrm{cm}^{-3}]$	**Valence band DOS*** $N_V\,[\mathrm{cm}^{-3}]$
AlGaAs	5.658	2.0	3.5644	11.3664	161.448	61.984	$1.71 \cdot 10^{19}$	$1.3 \cdot 10^{19}$
AlInP	5.658	2.53	4.2	11.7	–	–	$1.08 \cdot 10^{20}$	$1.28 \cdot 10^{19}$
GaInP	5.658	1.89	4.09	11.8	1945	141	$1.66 \cdot 10^{19}$	$1.78 \cdot 10^{19}$
GaInAs	5.658	1.41	4.0783	12.9154	8328	400	$1.66 \cdot 10^{19}$	$1.78 \cdot 10^{19}$
AlGaInP	5.653	2.17	4.26	12.2	–	–	$9.13 \cdot 10^{17}$	$7.81 \cdot 10^{18}$

*density of states

4.3 Simulating the State-of-the-Art GaInP/GaInAs/Ge solar cell

In this section, a first approach to the simulation of the LM GaInP/GaInAs/Ge cell will be presented. This cell has been manufactured and investigated by several photovoltaic companies; the two with the best results were Spectrolab and Fraunhofer ISE. This work attempts to simulate the one presented by Spectrolab, Inc., that was demonstrated to achieve an efficiency of 32.0% at $1\,\mathrm{sun}$ (AM1.5G) [14], with the following specific measures: a open-circuit voltage of $V_{OC} = 2.622\mathrm{V}$, a short-circuit current of $J_{SC} = 14.37\,\mathrm{mA\,cm^{-2}}$, a maximum power voltage of $V_{mp} = 2.301\mathrm{V}$ and a fill-factor of $FF = 85\%$.

Even though the published research on this cell has some specific structural information, such as the materials that constitute each layer, it does not contain any details on the doping, thickness, or even the composition of each material, since these specifics are treated as proprietary information of Spectrolab, and therefore are kept confidential.

Having as guide the detailed Ph.D. dissertation of Sharma [33], and having some modifications made in order to best adapt the cell to the one at Spectrolab (refer to Chapter 2, Figure 2.5a), it was possible to put together all the knowledge needed for the simulation. All the material properties used were already demonstrated in section 4.2.

4.3.1 Simulating the subcells

The first step was to simulate each subcell individually, in order to perceive the "role" that each one of them plays in the behavior of the stacked cell. For this, each subcell was simulated separately, and details relative to the $I - V$ characteristic and wavelength response were measured. On a first simulation attempt, all the subcells are simulated under the AM1.5 global spectrum. The cross-section of the cell was admitted to be $1\mu\mathrm{m}^2$ because of simulation times, and only the thickness of each layer was altered.

4.3.1.A The GaInP top cell

Starting from the top of the device, the first cell to be simulated is the GaInP top cell, which schematic and layer structure are presented in Figure 4.8 and Table 4.7, respectively. This cell is responsible for the absorption of high energy photons since it is on its surface that the light beams will fall onto. This is why the GaInP is chosen as the main material for the p–n junction. It has a bandgap of $E_g = 1.89\,\mathrm{eV}$ (for a composition of $x = 0.5$), which is a pretty high bandgap that allows for the high energy photons to be absorbed. In addition to this, two extra layers are added to the cell: a window layer and the BSF (back surface field) layer.

The window layer will act as an absorber layer; it has to have a high bandgap, small thickness, and low series resistance, in order to achieve a high optical output. The material chosen is then the AlInP,

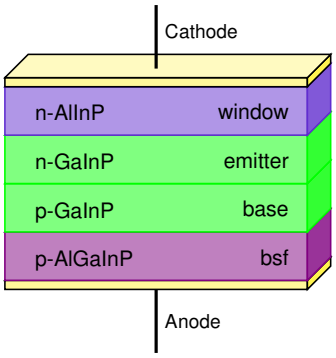

Figure 4.4: Top cell schematic.

Table 4.7: Top GaInP cell layer structure.

Layer	Material	Doping $[\mathrm{cm}^{-3}]$	Thickness $[\mu\mathrm{m}]$
Top cell window	n-$Al_{0.5}In_{0.5}P$	$1 \cdot 10^{19}$	0.03
Top cell emitter	n-$Ga_{0.5}In_{0.5}P$	$5 \cdot 10^{18}$	0.1
Top cell base	p-$Ga_{0.5}In_{0.5}P$	$1 \cdot 10^{17}$	0.75
Top cell bsf	p-$Ga_{0.5}In_{0.5}P$	$5 \cdot 10^{18}$	0.12

since it is capable of high bandgap values, at the same time of lattice matching the rest of the materials.

On the other hand, the BSF layer is a layer that is highly doped and exists to increase the short-circuit current of the cell. This happens because of the sharing of the applied voltage across the n–p and p–p+ junctions that minimizes the reflection of minority carriers and thus decreases the dark current. The material used was the quaternary AlGaInP.

The results obtained are presented in Figure 4.5. In Figure 4.5a is shown the obtained $I - V$ curve, where some of the specific parameters of the cell can be deducted; the cell has a $J_{SC} = 15.9487\mathrm{A}$, a $V_{OC} = 1.3390\mathrm{V}$ and a $FF = 86\%$. In Figure Figure 4.5b, the EQE[4] as well as the Absorption of the cell are presented. As expected, the cell only absorbs photons with higher energy than the bandgap, for which the Absorption is total. The maximum EQE achieved was $\mathrm{EQE}_{\max} = 90.65\%$ for a wavelength of $\lambda = 0.54\,\mu\mathrm{m}$.

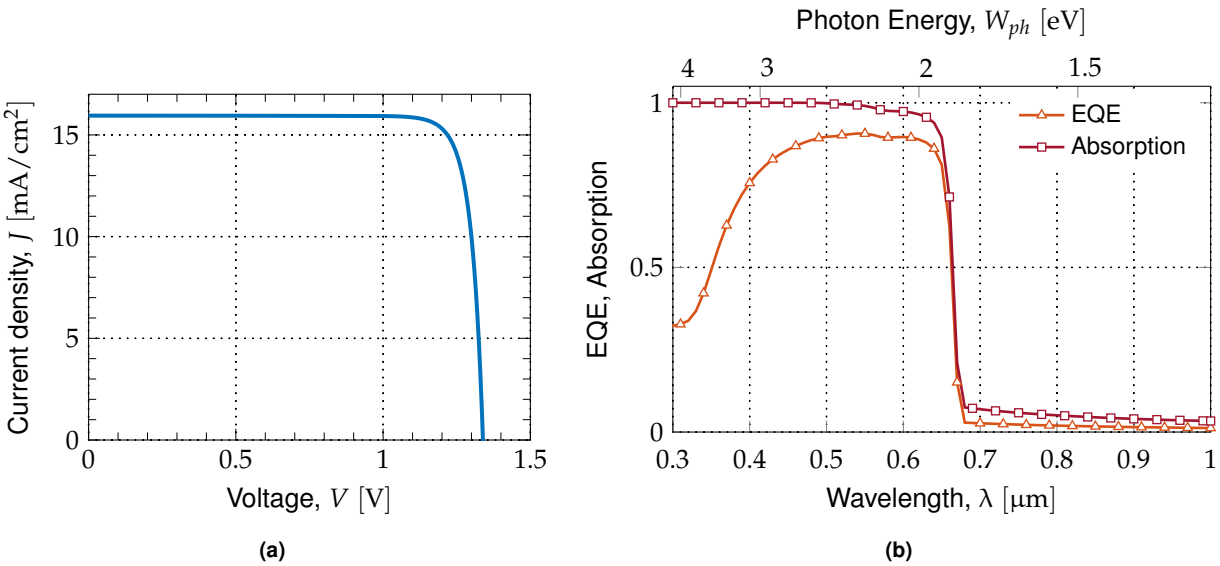

Figure 4.5: Simulation results for the top GaInP cell: (a) $I - V$ characteristic, and (b) EQE and Absorption.

[4]External Quantum Efficiency

4.3.1.B The GaInAs middle cell

The middle subcell has as main material the ternary GaInAs, and its schematic, along with layer structure, are described in Figure 4.6 and Table 4.8, respectively. This subcell is based on the more simple built GaAs solar cell, but given that the main goal is to lattice-match all the components that form the monolithic cell, the compound GaInAs (with composition $x = 0.99$) is chosen since its lattice constant can exact-match germanium's.

Both the window and BSF layers are composed of highly-doped GaInP, given its already discussed high optical properties, lattice-matched to Ge.

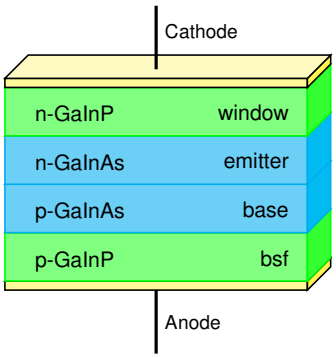

Figure 4.6: Middle cell schematic.

Table 4.8: Middle GaInAs cell layer structure.

Layer	**Material**	**Doping** $[\mathrm{cm}^{-3}]$	**Thickness** $[\mu\mathrm{m}]$
Mid. cell window	n-$Ga_{0.5}In_{0.5}P$	$5 \cdot 10^{19}$	0.03
Mid. cell emitter	n-$Ga_{0.99}In_{0.01}As$	$1 \cdot 10^{17}$	0.08
Mid. cell base	p-$Ga_{0.99}In_{0.01}As$	$1 \cdot 10^{17}$	3.5
Mid. cell bsf	p-$Ga_{0.5}In_{0.5}P$	$1 \cdot 10^{19}$	0.1

The results are shown in Figure 4.7. The middle cell obtained a $J_{SC} = 28.1937\mathrm{A}$, a $V_{OC} = 0.9444\mathrm{V}$ and a $FF = 85\%$, and its $I - V$ curve can be seen in Figure 4.7a. As for the wavelength response, it is illustrated in Figure 4.7b, where it shown the obtained EQE and Absorption. Once again, only photons with higher energy than the bandgap of GaInAs are absorbed. The EQE showed a maximum efficiency of $\mathrm{EQE}_{\max} = 97.29\%$ for a wavelength of $\lambda = 0.67\,\mu\mathrm{m}$.

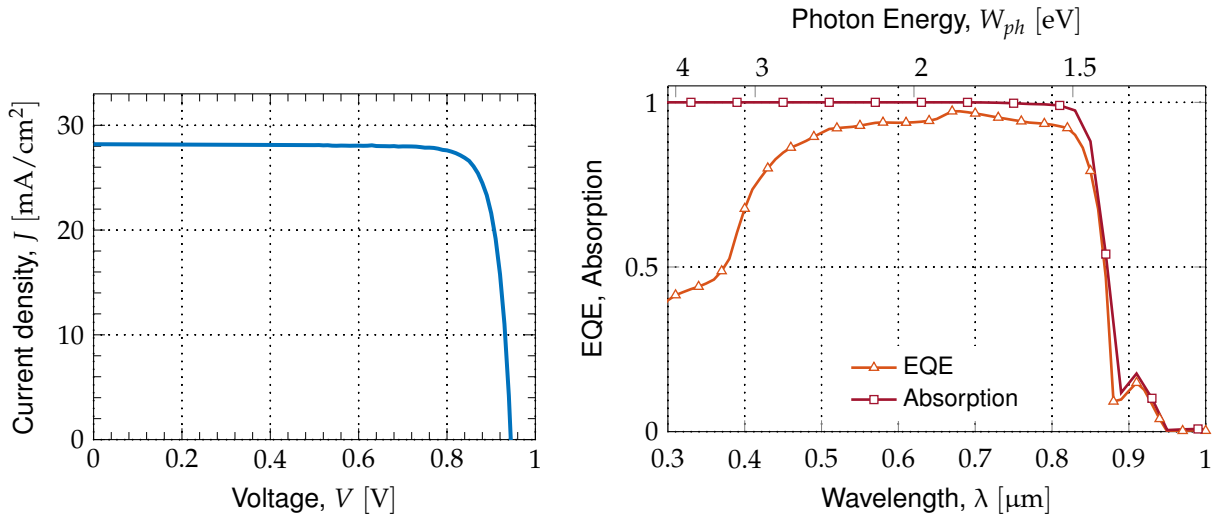

(a) (b)

Figure 4.7: Simulation results for the middle GaInAs cell: (a) $I-V$ characteristic, and (b) EQE and Absorption.

4.3.1.C The Ge bottom cell

Lastly, the bottom cell takes Ge instead of GaAs as the substrate. This has two major advantages, the first one is that Ge is cheaper than GaAs, and since it has a very low bandgap, and thus it is capable of reducing the thickness of the bottom cell for what is around $300\mu m$ for a GaAs substrate, to $170\mu m$ for a Ge substrate.

Besides the window layer, the bottom cell has a buffer layer, which is highly doped in order to reduce the resistive ohmic contacts between the bottom cell and the tunnel junction, given that the n-side of the tunnel diode is made of GaAs. The material used for the buffer is n-GaAs since the mismatch of the lattice constant of Ge and GaAs is about 0.5%.

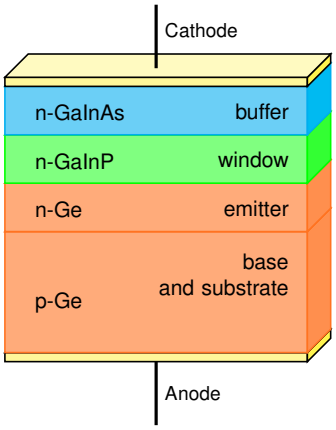

Figure 4.8: Bottom cell schematic.

Table 4.9: Bottom Ge cell layer structure.

Layer	**Material**	**Doping** $[\mathrm{cm}^{-3}]$	**Thickness** $[\mu m]$
Bot. cell buffer	n-$Ga_{0.99}In_{0.01}As$	$2 \cdot 10^{18}$	0.2
Bot. cell window	n-$Ga_{0.5}In_{0.5}P$	$5 \cdot 10^{19}$	0.02
Bot. cell emitter	n-Ge	$1 \cdot 10^{19}$	0.1
Bot. cell base	p-Ge	$2 \cdot 10^{17}$	170

The obtained results are displayed in Figure 4.9. The measures for the bottom cell were: a $J_{SC} = 39.2446\text{A}$, a $V_{OC} = 0.2558\text{V}$ and a $FF = 69\%$, with its $I - V$ characteristic showed in Figure 4.9a. Regarding the EQE measurements, seen in Figure 4.9b, the maximum EQE obtained was $\text{EQE}_{\text{max}} = 79.22\%$ for a wavelength of $\lambda = 1.05\,\mu\text{m}$.

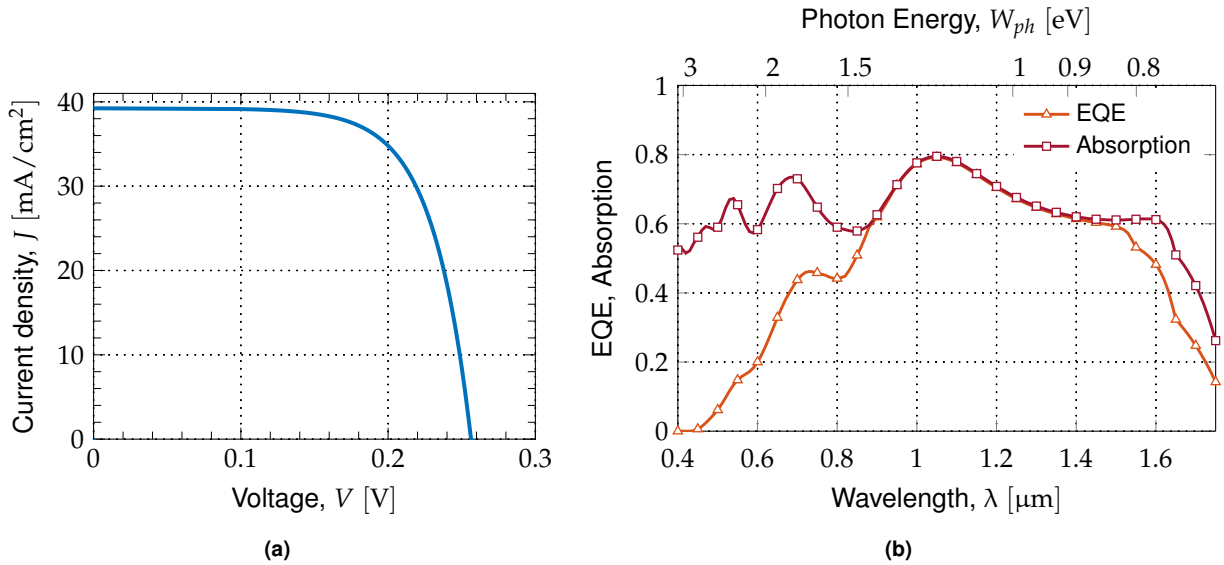

(a) (b)

Figure 4.9: Simulation results for the bottom Ge cell: (a) $I - V$ characteristic, and (b) EQE and Absorption.

4.3.2 Simulating the tunnel junctions

A simulation of the first tunnel junction was also made, in order to make sure that the materials' composition and doping were the appropriate ones. The schematic and layer structure are shown below in Figure 4.10 and Table 4.10, respectively. The two different tunnel junctions (AlGaAs-AlGaAs and AlGaAs-GaAs) were simulated, but given that the results were approximately the same, the results that are going to be presented are just from one tunnel diode, namely the AlGaAs-GaAs one.

This tunnel junction is similar to the GaAs-GaAs one, described in Chapter 6, section 6.1.2, but instead the p-GaAs top layer was replaced by the p-AlGaAs. This substitution was made mainly because

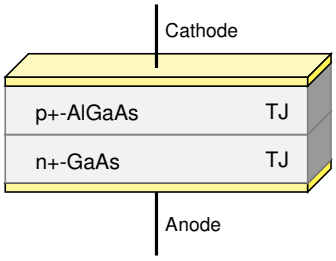

Figure 4.10: AlGaAs-GaAs tunnel junction schematic.

Table 4.10: AlGaAs-GaAs tunnel junction layer structure.

Layer	**Material**	**Doping** $[\text{cm}^{-3}]$	**Thickness** $[\mu\text{m}]$
TJ1 top	p+-$Al_{0.54}Ga_{0.46}As$	$1 \cdot 10^{19}$	0.05
TJ1 bottom	n+-GaAs	$1 \cdot 10^{19}$	0.05

of the capability of this cell to be a concentrator photovoltaic cell and thus has to endure great current densities. For a concentrator cell, this junction has to be doped in the order of magnitude of 10^{20}, but for the sake of $1\ \mathrm{sun}$ simulations, the doping was lowered for the order of 10^{19}.

The dark $I-V$ characteristic of the junction is shown in Figure 4.11, where it is observable a peak tunneling current density of approximately $500\mathrm{mA\,cm^{-2}}$, which, obviously, is more than enough to withstand the total current density of the stacked cell.

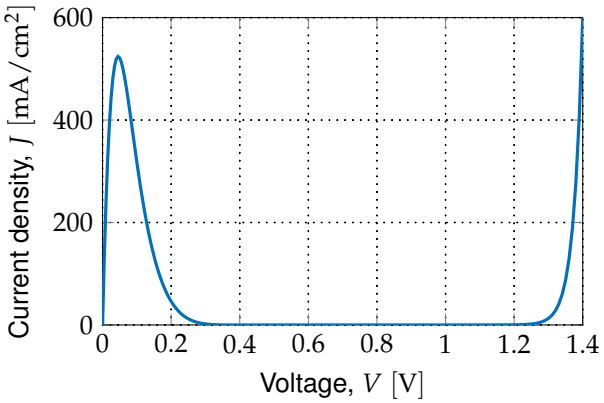

Figure 4.11: Dark $I-V$ characteristic of the AlGaAs-GaAs tunnel junction, with doping concentration of $N_D = 1\cdot 10^{19}\ \mathrm{cm^{-3}}$.

4.3.3 Simulating the stacked GaInP/GaInAs/Ge cell

For the purpose of simulating the stacked cell, one stacks the subcells, previously demonstrated, interconnected by the tunnel diodes. For the simulation to converge, ohmic contacts must be defined between the subcell–tunnel diode and tunnel diode p–n junctions. These contact resistances are nothing more than boundary conditions that are used in order to emulate the resistivity between semiconductor contacts. In Silvaco ATLAS there are several ways of doing this, however, in this work, the method chosen was to create a floating contact with an extremely high resistance $[\Omega\,\mu\mathrm{m}]$, so that the contact voltage across the junctions may be insignificant. For example, for a voltage tolerance of $10^{-5}\mathrm{V}$ and a contact resistance of only $1\cdot 10^{7}\,\Omega\,\mu\mathrm{m}$, a current of $10^{-12}\mathrm{A\,\mu m^{-1}}$ flows through the contact, which is a significant value for the simulations performed in this work. Therefore, the value used for contact resistances was $1\cdot 10^{9}\,\Omega\,\mu\mathrm{m}$.

On a first approach, the stacked cell simulated in ATLAS was simulated without the metal grid on top, with the front and back contacts with the same extension as the rest of the cell layers. The results obtained with this method were artificially high since this method does not take into consideration the contact effects. This approach to solar cell simulation is a 1-D model since the structure only varies in one direction.

The second method utilized was employed to try and simulate the contact effects of the metal grid

(MG). For that, the electrode became smaller in comparison with the rest of the structure, and a cap layer was put below it, as a capping layer for good ohmic contact formation. With this, there is horizontal and vertical variation in layers, and so this model is called the 2-D model.

Having as reference the structure used at Spectrolab, the structure used for simulation in ATLAS was built and is identical to the one depicted in Figure 4.12.

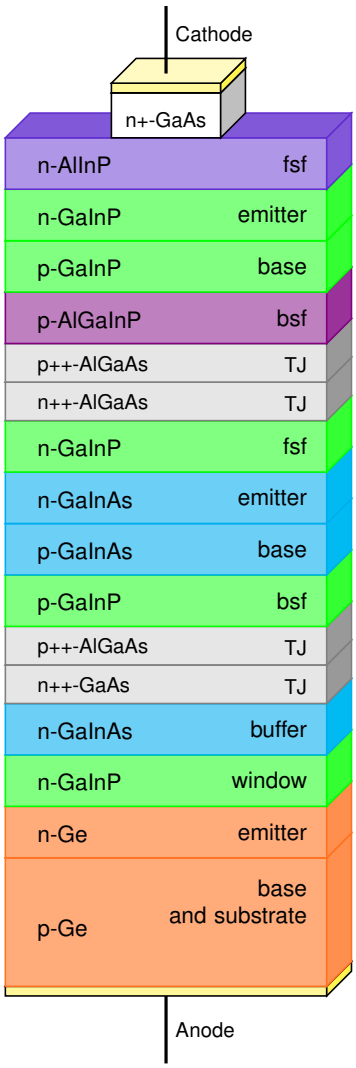

Figure 4.12: Stacked cell schematic.

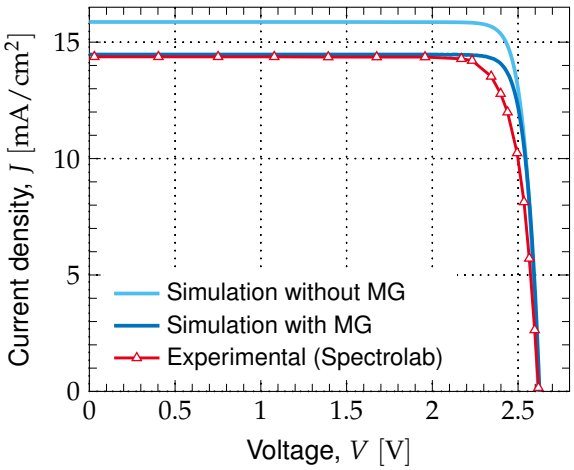

Figure 4.13: $I-V$ characteristics of the stacked cell: simulation results in blue and experimental results [14] in red.

Table 4.11: Comparison of experimental and simulation values for the stacked cell.

	Experimental	**Simulation**	
	(Spectrolab)	without MG*	with MG*
J_{SC} [mA/cm^2]	14.37	15.8771	14.4693
V_{OC} [V]	2.622	2.6296	2.6248
V_{MP} [V]	2.301	2.39	2.38
FF	0.85	0.89	0.88
Eff. [%]	32.0	36.9	33.65

*metal grid

The obtained $I-V$ characteristics for both models, as well as the experimental curve from Spectrolab [14], are illustrated in Figure 4.13. The comparison between measured values between the experimental and simulated curves are shown in Table 4.11. Analyzing the results, it is clear that the most accurate technique to emulate the performance of a real solar cell is the 2-D model, in which some of the device losses are considered, and thus efficiency and short-circuit current are most influenced.

4.3.3.A Mechanic configuration

Regarding the mechanic configuration of the TJ cell, it is apparent that the subcells are series-connected, particularly when interpreting the $I-V$ characteristics of each subcell, with the $I-V$ characteristic of the stacked cell, all shown together in Figure 4.14. It is observable that the stacked cell's open-circuit voltage V_{OC} is approximately the sum of each subcells' open-circuit voltage. On the other hand, the short-circuit current I_{SC} of the whole cell is equal to the lowest short-circuit current verified in the subcells, which is the one from the top GaInP cell.

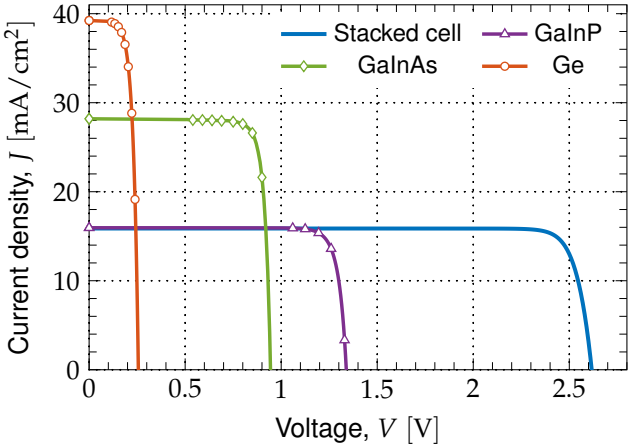

Figure 4.14: Comparison between $I-V$ characteristics of each subcell and stacked cell.

4.3.3.B External Quantum Efficiency

The final analysis was to obtain the EQE from each subcell when stacked. For this simulation to work, one can resort to the optical bias method. This is accomplished by saturating all the subcells simultaneously, except the one under test, so that the saturated junctions will not limit the current, while the cell that is not saturated (the one at study) will dictate the current value, and thus the external quantum efficiency can be computed.

The simulated results, along with the experimental curves from the cell at Spectrolab [34], are presented in Figure 4.15. It is perceptible that each subcell only absorbs in a very specific wavelength interval, which depends mainly on the bandgap of the rest of the subcells. The reason behind this is the spectrum splitting effect by stacked distribution, which was previously mentioned in Chapter 2, section 2.2.1.A. In this approach and for the specific cell at hand, the GaInP top cell will absorb photons with energy $W_{ph} > 1.89\,\text{eV}$, the GaInAs middle cell will then absorb between the range of $1.89 > W_{ph} > 1.41\,\text{eV}$ and, lastly, the Ge bottom cell will absorb $1.41 > W_{ph} > 0.661\,\text{eV}$.

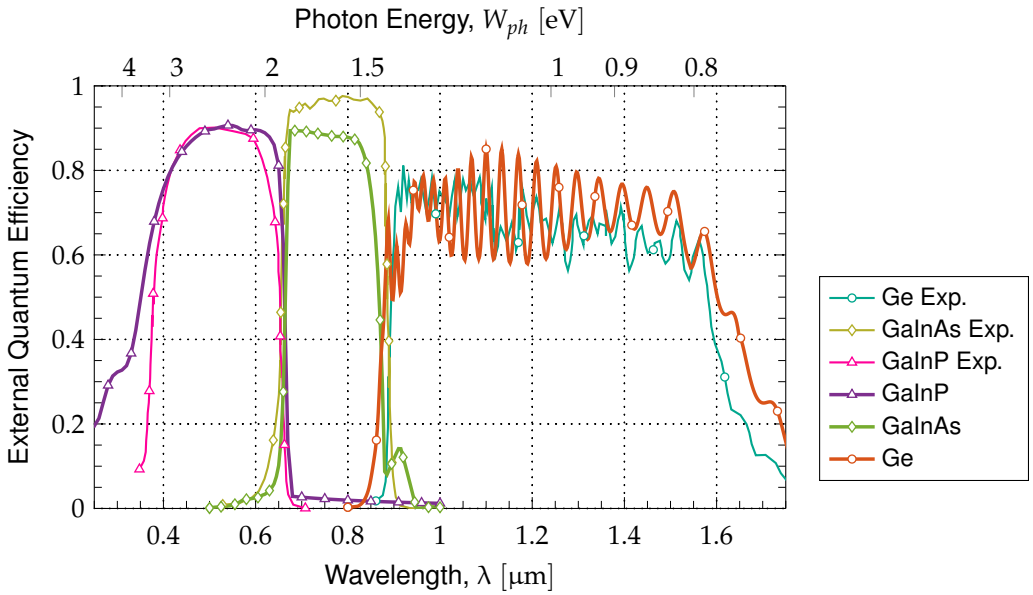

Figure 4.15: External Quantum Efficiencies of each subcells: simulation and experimental results [34].

4.3.4 Temperature Effects

One of the most important factors that has a massive influence on the behavior of semiconductors is, naturally, temperature. Most of the solar cells are designed and tested for a nominal operating cell temperature (NOCT) of $25°\mathrm{C}$, which in absolute temperature values is generally approximated to $T = 300\mathrm{K}$. Although, in reality, terrestrial PV panels can experience temperatures that can normally go from $15°\mathrm{C}$ in colder days, to $65°\mathrm{C}$ in hotter days. The cells under study in this work, however, have to be designed to withstand the high-temperature ranges that only space can bestow. These temperatures can vary from very high temperatures, namely in HIHT[5] missions, and deep-space temperatures like $-170°\mathrm{C}$, which is the cell temperature for Saturn-orbit missions (at 9.54 A.U. from the sun).

Thereby, it makes sense to try and simulate these cells under varied temperature and spectra conditions. Since these circumstances only take place in space, the AM0 spectrum will be utilized.

4.3.4.A High and low temperatures

On a first approach to try and perceive how an increase in temperature would affect solar cell operation, a simulation was run firstly for $T = 300\mathrm{K}$ and then higher temperatures, in intervals of $50\mathrm{K}$, to the final temperature of $T = 500\mathrm{K}$. The obtained $I - V$ curves, along with a plot that shows efficiency and fill-factor variance with temperature, are both shown in Figure 4.16b. This is a result of the bandgap narrowing with temperature (`BGN` model), which was already mentioned in Chapter 3, section 3.2.4.

[5] high intensity high temperature

Besides the response of the tandem cell at high temperatures, it is also pertinent to study these cells at temperatures below $0\,°\mathrm{C}$, given their utility in extreme environments. Even though there are some behavior patterns that can be expected, namely the increase in the open-circuit voltage, V_{OC}, and in the power conversion efficiency, there is some interest in how much these parameters vary for low temperatures.

For these simulations, ATLAS requires more than the `TEMPERATURE` model that specifies the cell NOCT; it also needs an additional model that simulates how the semiconductor mobilities alter with temperature (`KLAASSEN` model). The low-temperature simulations also needed remeshing; the number of lines was increased to achieve convergence.

The extracted $I - V$ characteristics for each temperature range are presented in Figure 4.16. All the simulations are performed under the $1\,\mathrm{sun}$ AM0 spectrum.

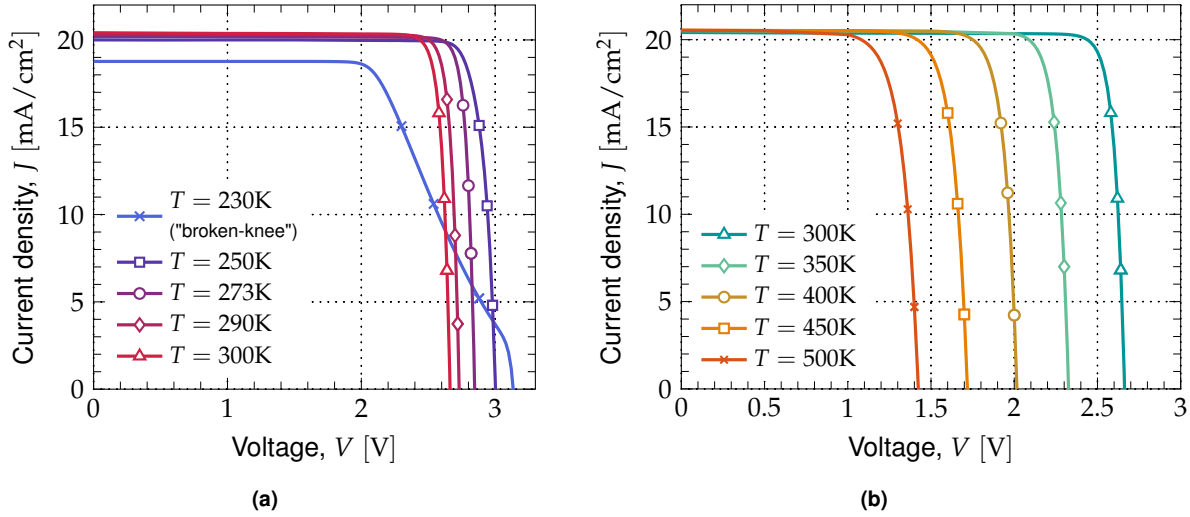

Figure 4.16: Tandem cell's I-V characteristics obtained for two different intervals of temperature: (a) low temperature range, from $T = 250\mathrm{K}$ to $T = 300\mathrm{K}$, and (b) high temperature range, from $T = 300\mathrm{K}$ to $T = 500\mathrm{K}$.

All the relevant values from both graphs of Figure 4.16 are registered in Table 4.12. It is possible to see the variance of both I_{SC} and V_{OC} in relation to the default values of when $T = 300\mathrm{K}$ (4.17a) and how the Fill-Factor and the Efficiency alter with temperature (4.17b).

Regarding the open-circuit voltage and the short-circuit current, the device behaviors as expected, I_{SC} varies insignificantly whereas the V_{OC} decreases as temperature increases.

As for the Efficiency and Fill-factor, they both decrease as temperature rises, however, as the array temperature gets colder, the changes begin to be non-linear, and new problems arise. One of them is the fact that, as temperature decreases, carriers start to enter the state of "freeze-out", in which there is not enough thermal energy for the dopants to be sufficiently ionized, and thus provoking a shortage of charge carriers. Another issue is the phenomenon called "broken-knee" or "double slope", in which the $I - V$ characteristic becomes degraded, greatly reducing FF and efficiency – this is clearly seen in the

Table 4.12: Measured values for both temperature ranges: high and low temperatures, from the respective plots (a) and (b), displayed in Figure 4.16.

	Figure 4.16a					**Figure 4.16b**			
	230K	250K	273K	290K	300K	350K	400K	450K	500K
$J_{SC}[\mathrm{mA/cm^2}]$	18.7692	19.9959	20.2036	20.3397	20.4106	20.5206	20.5199	20.5445	20.5342
$V_{OC}[\mathrm{V}]$	3.1344	3.0021	2.8466	2.7307	2.6627	2.3263	2.0162	1.7189	1.4237
FF	0.64	0.88	0.91	0.90	0.89	0.87	0.85	0.81	0.77
Eff.[%]	27.77	38.79	38.25	36.72	35.73	30.59	25.74	21.05	16.46

curve for $T = 230\mathrm{K}$.

Notwithstanding, colder environments, to a certain extent, are good for solar cells since there is a boost in the overall performance; these results confirm the need for some PV panels to have cooling systems installed so that the power conversion efficiency is maximized.

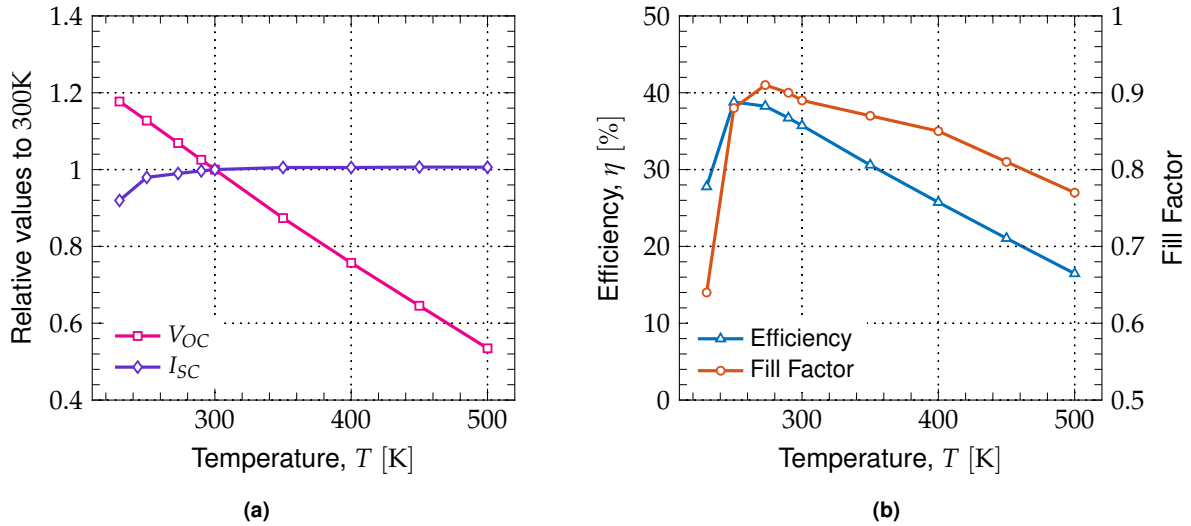

Figure 4.17: Variance of parameters with temperature: (a) short-circuit current and open-circuit voltage, and (b) efficiency and fill-factor.

4.4 Optimization of the LM GaInP/GaInAs/Ge solar cell

In this last section, an overall optimization of the LM GaInP/GaInAs/Ge is attempted; two studies on how thickness and doping affect the overall performance of the cell were made, so that the maximum potential of the cell is reached. In the first study, both top and middle subcells were considered, and so two tests for each cell were made. The properties of the whole cell, unless stated otherwise, were maintained constant, with the default, previously simulated, values.

Given that the solar cell that was simulated until now was optimized for concentrator photovoltaic applications, this optimization will be done for space applications for LEO missions. This way, the spectrum utilized will be the AM0 $(1337\,\mathrm{W/m^2})$, with the intensity of $1\,\mathrm{sun}$ and the cell temperature of $T = 300\mathrm{K}$.

4.4.1 Thickness variation

For the purpose of varying the cell thickness, one must choose which layers are going to be altered. Firstly, given that the photocurrent of the whole cell is highly dependable of the top cell, the layers chosen were the base and emitter GaInP layers. The BSF and FSF layers were not altered, since their values were already at the minimum possible. The main aim of the study is to choose thickness values that establish a compromise between efficiency and size of the cell, since the small the bulkiness of the whole cell the better.

The test consisted of varying both base and emitter thicknesses and evaluate efficiency improvement. The obtained results are displayed in Table 4.13, with the initial thickness values in gray, and the values that achieved the best efficiency in green, with an efficiency of 31.8039%, which in comparison to the initial value of 31.7687% consists in an improvement of $+0.1107\%$.

A graphic display for a better understanding of how thickness variation affects the efficiency is also shown in Figure 4.18. In this, one can observe the basic contour of the obtained results (Figure 4.18a), and a 3D surface computed with the cubic method of Curve Fitting Toolbox of MATLAB©. With the aid from the graphic displays, it is fairly visible that efficiency depends on both base and emitter thicknesses, being clear that higher efficiencies concentrate in a specific area in the center of the thicknesses' scope.

A second test is made to analyze how and if the middle cell thickness affects the whole cell performance. Once again, BSF and FSF layers were not touched, varying only the thickness of p-base and n-emitter GaInAs layers. The top GaInP layers' thicknesses were the initial ones, without employing the optimization of the first test. The results are presented in Table 4.14, with the initial measurements in gray and the best efficiency in green. Alas, in this case, the best-obtained results (in green) correspond to a thickness increase of $0.5\,\mu\mathrm{m}$ in the base thickness. Since a bulkier cell is not the desired outcome, the second-best results that achieved an efficiency of 31.8036% were chosen. This efficiency value corresponds to an improvement of $+0.1098\%$.

Table 4.13: First study, first test: **Top GaInP subcell** thickness variation of the p-base and n-emitter layers.

p-Base Thick. [μm]	n-Emitter Thick. [μm]	Short-circuit current J_{SC} [mA/cm^2]	Open-circuit voltage V_{OC} [V]	Fill-factor FF [%]	Efficiency η [%]	Variation [%]
0.65	0.09	18.5061	2.6257	89.1202	31.7211	−0.1499
0.70	0.09	18.5848	2.6255	88.9124	31.7792	+0.0330
0.75	0.09	18.6750	2.6254	88.4592	31.7687	+0.0000
0.80	0.09	18.7421	2.6250	87.8996	31.6773	−0.2877
0.65	0.10	18.4947	2.6256	89.2353	31.7411	−0.0867
0.70	0.10	18.5960	2.6254	88.8770	31.7839	+0.0477
0.75	0.10	18.6750	2.6251	88.4666	31.7687	0.0000
0.80	0.10	18.7318	2.6248	87.8883	31.6530	−0.3641
0.65	0.11	18.5055	2.6256	89.2165	31.7530	−0.0493
0.70	0.11	18.5956	2.6254	88.9332	31.8039	+0.1107
0.75	0.11	18.6979	2.6252	88.4535	31.8036	+0.1098
0.80	0.11	18.7311	2.6249	87.9413	31.6721	−0.3039
0.65	0.12	18.5174	2.6259	89.0013	31.7003	−0.2153
0.70	0.12	18.5954	2.6257	88.7979	31.7583	−0.0327
0.75	0.12	18.6631	2.6254	88.4606	31.7492	−0.0613
0.80	0.12	18.7421	2.6251	87.6656	31.5932	−0.5524

Similarly to the first test, graphic displays of the results of the second test are illustrated in Figure 4.19, with the contour and the 3D fitted surface. Analyzing these plots, it is understandable that the higher the middle cell's base thickness, the higher the efficiency. Unlike the first test, the middle cell base thickness is predominant when discussing how the efficiency is affected.

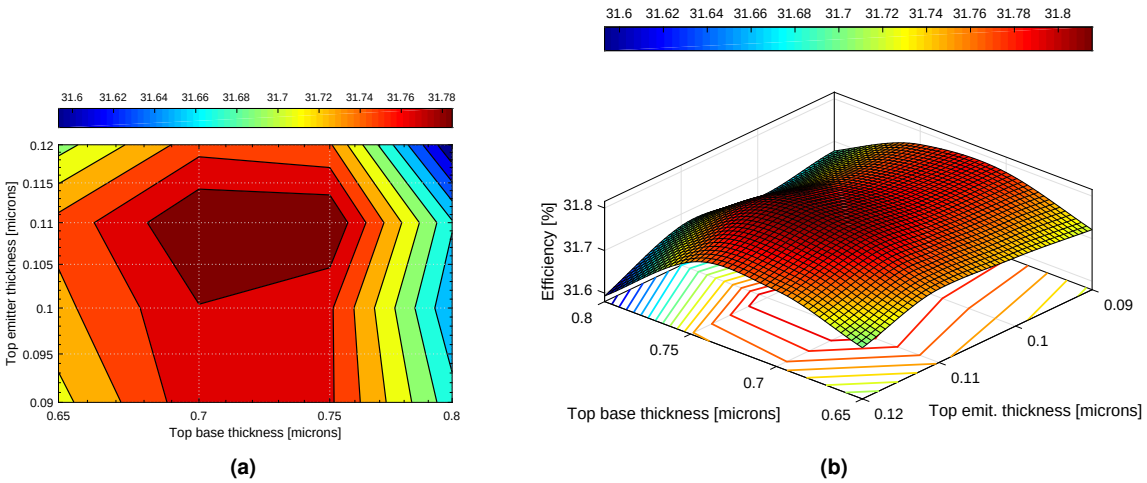

(a) **(b)**

Figure 4.18: Graphic display of the results of the first test (Table 4.13): (a) basic contour, and (b) 3D fitted surface with cubic method (MATLAB©).

Table 4.14: First study, second test: **Middle GaInAs subcell** thickness variation of the p-base and n-emitter layers.

p-Base Thick. [μm]	n-Emitter Thick. [μm]	Short-circuit current J_{SC} [mA/cm^2]	Open-circuit voltage V_{OC} [V]	Fill-factor FF [%]	Efficiency η [%]	Variation [%]
3.25	0.07	18.6862	2.6239	88.4002	31.7491	−0.0616
3.50	0.07	18.6750	2.6251	88.4540	31.7639	−0.0150
3.75	0.07	18.6744	2.6262	88.4688	31.7817	+0.0408
4.00	0.07	18.6744	2.6273	88.4350	31.7825	+0.0434
3.25	0.08	18.6754	2.6239	88.4956	31.7650	−0.0115
3.50	0.08	18.6750	2.6251	88.4666	31.7687	0.0000
3.75	0.08	18.6750	2.6262	88.4677	31.7817	+0.0408
4.00	0.08	18.6744	2.6272	88.5086	31.8074	+0.1220
3.25	0.09	18.6862	2.6239	88.3999	31.7491	−0.0616
3.50	0.09	18.6750	2.6251	88.5097	31.7836	+0.0468
3.75	0.09	18.6861	2.6262	88.4744	31.8036	+0.1098
4.00	0.09	18.6742	2.6272	88.4387	31.7825	+0.0434
3.25	0.10	18.6754	2.6239	88.4520	31.7491	−0.0616
3.50	0.10	18.6750	2.6251	88.4964	31.7788	+0.0318
3.75	0.10	18.6977	2.6262	88.3479	31.7777	+0.0284
4.00	0.10	18.6742	2.6273	88.4346	31.7825	+0.0434

Lastly, the best results from both tests were applied in simulation, so that both subcell optimizations could be taken into account. The obtained parameters were: $J_{SC} = 18.5943\,\mathrm{mA/cm^2}$, $V_{OC} = 2.6276\,\mathrm{V}$,

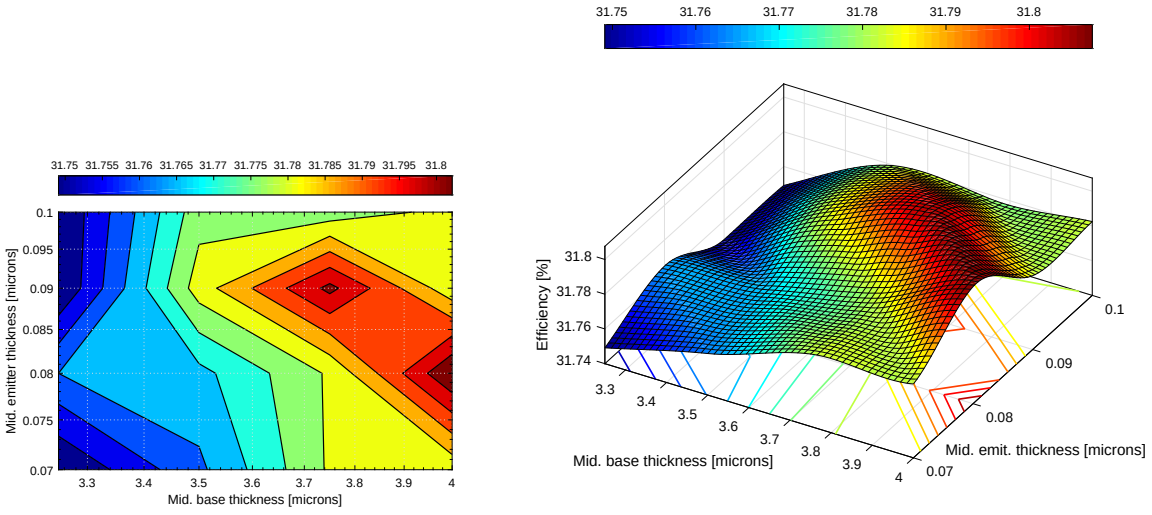

(a) **(b)**

Figure 4.19: Graphic display of the results of the second test (Table 4.14): (a) basic contour, and (b) 3D fitted surface with cubic method (MATLAB©).

$FF = 88.98\%$ and an efficiency of $\eta = 31.8431\%$, which translates in an improvement of 0.2343%, in comparison with the initial value.

4.4.2 Doping variation

The second and final study is to evaluate how doping alters the performance of the cell. The simulation is run with the best thickness values obtained in the first study (section 4.4.1). Only the top cell's base and emitter are going to be contemplated in this study, since varying the doping of the middle cell layers seem to have little impact in the power conversion efficiency of the cell.

The obtained results are shown in Table 4.15, with the default values highlighted in gray (the first study reached an overall optimization of 0.2343%), and the best result highlighted in green. The best efficiency obtained was 33.0194%, which corresponds to a total improvement of 3.9368% of the initial value that was $\eta = 31.7687\%$.

The values chosen for doping were chosen with caution, given that higher doping values decrease

Table 4.15: Second study: doping variation of the p-base and n-emitter layers in the top subcell.

p-Base Dop. $[\mathrm{cm}^{-3}]$	n-Emitter Dop. $[\mathrm{cm}^{-3}]$	Short-circuit current J_{SC} $[\mathrm{mA/cm}^2]$	Open-circuit voltage V_{OC} [V]	Fill-factor FF [%]	Efficiency η [%]	Variation [%]
5.00×10^{16}	5.00×10^{17}	18.6589	2.6146	88.5849	31.6566	-0.3528
1.00×10^{17}	5.00×10^{17}	18.6468	2.6274	88.8988	31.9033	$+0.4236$
5.00×10^{17}	5.00×10^{17}	18.6583	2.6586	89.8205	32.6373	$+2.7341$
1.00×10^{18}	5.00×10^{17}	18.6468	2.6399	89.8302	32.3909	$+1.9585$
2.00×10^{18}	5.00×10^{17}	18.6808	2.6527	88.6413	32.1756	$+1.2808$
5.00×10^{16}	1.00×10^{18}	18.6366	2.6147	88.5956	31.6232	-0.4579
1.00×10^{17}	1.00×10^{18}	18.6252	2.6273	88.9295	31.8759	$+0.3373$
5.00×10^{17}	1.00×10^{18}	18.6371	2.6378	89.6146	32.2704	$+1.5792$
1.00×10^{18}	1.00×10^{18}	18.6371	2.6805	90.2328	33.0194	$+3.9368$
2.00×10^{18}	1.00×10^{18}	18.6477	2.6171	88.5709	31.6619	-0.3362
5.00×10^{16}	5.00×10^{18}	18.5950	2.6148	88.7140	31.5961	-0.5432
1.00×10^{17}	5.00×10^{18}	18.5943	2.6276	88.9757	31.8431	$+0.2343$
5.00×10^{17}	5.00×10^{18}	18.6068	2.6356	89.8876	32.2888	$+1.6371$
1.00×10^{18}	5.00×10^{18}	18.6068	2.6572	90.4562	32.7603	$+3.1213$
2.00×10^{18}	5.00×10^{18}	18.5949	2.5816	86.9694	30.5813	-3.7376
5.00×10^{16}	1.00×10^{19}	18.5969	2.6148	88.6452	31.5749	-0.6099
1.00×10^{17}	1.00×10^{19}	18.5969	2.6274	88.9426	31.8334	$+0.2038$
5.00×10^{17}	1.00×10^{19}	18.5857	2.6462	90.1230	32.4665	$+2.1967$
1.00×10^{18}	1.00×10^{19}	18.5857	2.6694	88.6655	32.2221	$+1.4272$
2.00×10^{18}	1.00×10^{19}	18.5288	2.5659	90.3956	31.4806	-0.9068

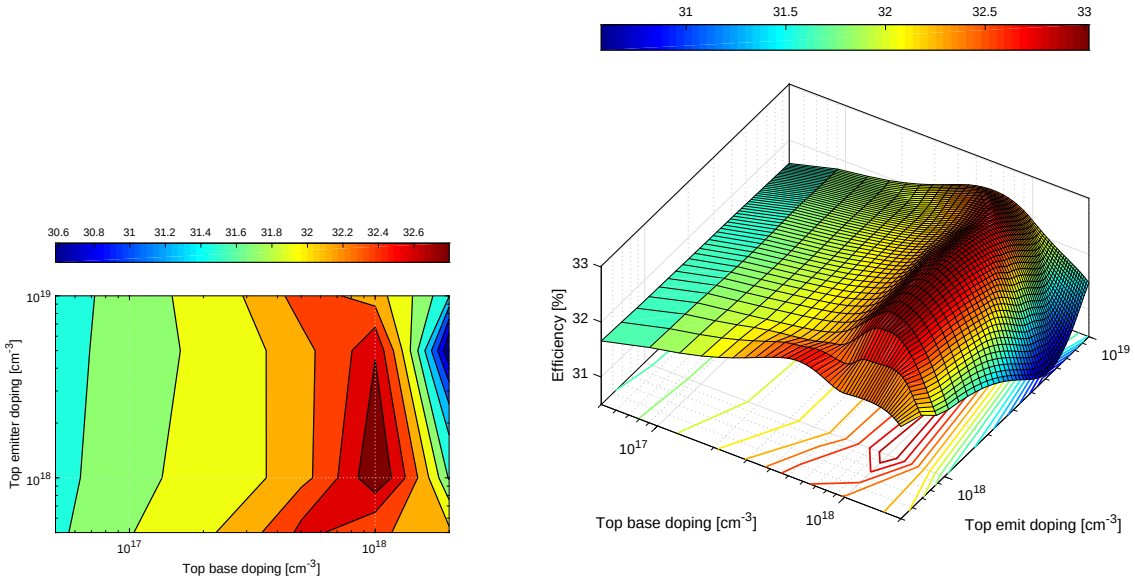

Figure 4.20: Graphic display of the results of the second study (Table 4.15): (a) basic contour, and (b) 3D fitted surface with cubic method (MATLAB©).

the potential barrier (voltage potential, V_0, in Appendix 6, section 6.1.1) and thus make higher efficiency values possible to achieve. However, this increase is not indefinite, since the minority carrier lifetime and diffusion length decrease with doping increase [35]. This results in a search for the optimum doping value that increases efficiency but does not degrade the electronic properties of the semiconductor. No doping values past $2.00 \times 10^{18}\,\mathrm{cm}^{-3}$ for the base and $1 \times 10^{19}\,\mathrm{cm}^{-3}$ for the emitter were chosen, since a deterioration in the $I - V$ curve is observed for values higher than these.

Similarly to the first study, the contour and the 3D fitted cubic surface of the obtained results are provided in Figure 4.20. It is clear that base doping plays a major role in efficiency; as base doping values increase, efficiency slowly improves, reaching a region of values on which the efficiency is the highest possible. Beyond those values, there is an abrupt drop in the short-circuit current and open-circuit voltage, and thus resulting in efficiency reduction.

In conclusion, the cell is then optimized for the AM0 spectrum, at the temperature of $300\mathrm{K}$. Of course, as it was already stated in previous chapters, the temperature in space can oscillate from very low to very high temperatures, and so each array of solar cells must be optimized in accordance with the conditions it is going to operate into.

CHAPTER 5

Conclusions

5.1 Discussion of Results

The main aim of this thesis is to create a model so that a triple-junction state-of-the-art solar cell could be analyzed with accuracy, and without the need to resort to more advanced, and expensive, technologies of simulation.

Comparing the simulated results with the actual experimental results by Spectrolab, Inc. one could say that the goal was achieved, and the cell was emulated successfully, to some extent. Both the open-circuit voltage and short-circuit current were fairly replicated, which means that the region materials, thickness, and doping were correctly modeled.

However, both the fill-factor and efficiency were not consistent with their experimental counterparts; this may have to do with the fact that losses were not properly accounted in the modeled cell since the only loss mechanism present were the metal grid, back and front contacts, and the use of a complex refractive index. This may have been because experimental values are calculated by appropriate measuring devices, such as a multimeter, connecting them in series/parallel to a resistor, which in turn is connected to both terminals of the cell. This results in part of the losses not being accounted for in the simulation.

Other relevant differences are the external quantum efficiencies obtained for each subcell, in contrast with the experimental curves. This is due mainly to the use of refractive indexes that do not correspond to the exact composition of a certain material. For instance, the most obvious difference is between the simulated and experimental frequency responses in the middle cell; this discrepancy may reside in the fact that the only refractive index available is not a rigorous match for the composition of $x = 0.99$ in $Ga_0.99In_{0.01}As$. This explanation is valid for other ternaries used as well.

Bearing in mind that temperature plays a significant part in semiconductor performance, a test to

evaluate how temperature influences the cell was also conducted. Most of the published research on how the GaInP/GaInAs/Ge solar cell behaves under different temperatures only has into consideration the higher range of temperature, given its paramount utilization in concentrator photovoltaic systems. With spacecraft implementation on sight, it was thought to be relevant to verify how the cell behaviors at low temperatures. Even though some plausible results were obtained, simulations in temperatures below $230\mathrm{K}$ did not obtain convergence, since the cell's design was not prepared for such low-temperature environments.

Finally, an optimization of the GaInP/GaInAs/Ge LM cell was also conducted. In this, the cell was tweaked so it could reach its maximum potential for a $1\,\mathrm{sun}$ AM0 incidence. This could prove of some value for the photovoltaic industry dedicated to the fabrication of solar cells for space applications, given that the doping can significantly boost the cell's efficiency.

Regarding the simulation times, depending on the mesh fineness and the voltage step that is being utilized at the time, the whole cell takes roughly six minutes to simulate with Newton's method. This may be an advantage over more complex and detailed ways of simulation that are more time-consuming if the main objective is simply to obtain the major key aspects of the cell.

5.2 Future Work

Given the lack of time and space in this thesis, some tests and simulations that were considered interesting to attempt were left for future work. Since the main focus of this work has been the simulation of the TJ cell, advanced techniques used for optimizing the cell have been left aside. These simulations would require further investigation on the material properties, on different spectrum intensities, and sophisticated methods of solar cell design. The proposed ideas would be the following:

1. It would be relevant to simulate the already mentioned metamorphic GaInP/GaInAs/Ge cell and see what major differences are observed when comparing it to its lattice-matched counterpart. While the LM cells are still the state-of-the-art for space missions, the metamorphic one has been achieving noteworthy efficiencies in the photovoltaic community, simply because new bandgap values for the top and middle subcells are being tested. This would then translate into a test to examine how cell performance is affected by the top and middle subcell bandgaps.

2. From a design point-of-view, an attractive way of further optimizing the cell is to use an algorithm that takes into account all the layers of the cell. One example is the genetic algorithm for layer thicknesses, that unlike the method that was used for optimization in this work, takes into account all the layers by performing a metaheuristic parameter sweep [36], capable of achieving faster and better results when compared to "hard-coded" methods.

3. The third idea would be to explore the difference in spectrum intensity LILT[1] space missions. While there were several attempts to simulate the LM cell in an environment with $0.03\,\mathrm{AM0}$ solar intensity, and at a temperature below $100\mathrm{K}$, the simulations did not converge and no results could be obtained. One of the main reasons of why this happened may be because the design of the cell was not adapted to such extreme conditions and certain features, such as an ARC or low-doping levels of the base layers [37], were not applied. Tweaking the cell would then be necessary for LILT missions simulation.

While the third idea would be possible to implement in Silvaco ATLAS, the other two might need different, more advanced, software. The first idea has to have the same materials with different compositions present at the same time in the cell structure. Silvaco ATLAS may not be the best software for doing this, since multiple refractive indexes would be defined for the same material. A suggestion would be Thesaurus TCAD by Synopsys since it provides more options to the user and has an integrated library of materials that is well updated with the latest research while providing more complex tools for solar cell analysis.

[1] low intensity low temperature

Bibliography

[1] J. Khan and M. H. Arsalan, "Solar power technologies for sustainable electricity generation – A review," *Renewable and Sustainable Energy Reviews*, vol. 55, pp. 414–425, 2016. [Online]. Available: http://dx.doi.org/10.1016/j.rser.2015.10.135

[2] R. Castro, *Uma Introdução às Energias Renováveis: Eólica, Fotovoltaica e Mini-Hídrica*, 1st ed. IST Press, 2011.

[3] P. Chiu, D. Law, R. Woo, S. Singer, D. Bhusari, W. Hong, A. Zakaria, J. Boisvert, S. Mesropian, R. King, and N. Karam, "35.8% space and 38.8% terrestrial 5J direct bonded cells," pp. 35–37, 2014.

[4] M. A. Green, Y. Hishikawa, E. D. Dunlop, D. H. Levi, J. Hohl-Ebinger, M. Yoshita, and A. W. Ho-Baillie, "Solar cell efficiency tables (Version 52)," *Progress in Photovoltaics: Research and Applications*, vol. 27, no. 1, pp. 3–12, 2019.

[5] J. M. Olson, D. J. Friedman, and S. Kurtz, "High-Efficiency III-V Multijunction Solar Cells," in *Handbook of Photovoltaic Science and Engineering*, 1st ed., A. Luque and S. Hegedus, Eds. Wiley, 2003, ch. 9, pp. 359 – 407.

[6] S. P. Philipps, F. Dimroth, and A. W. Bett, *High-Efficiency III-V Multijunction Solar Cells*, 3rd ed. Academic Press – Elsevier, 2018, pp. 439 – 463.

[7] A. W. Bett, F. Dimroth, G. Stollwerck, and O. V. Sulima, "III-V compounds for solar cell applications," *Applied Physics A: Materials Science and Processing*, vol. 69, no. 2, pp. 119–129, 1999.

[8] F. Dimroth, C. Baur, A. Bett, M. Meusel, and G. Strobl, "3-6 Junction Photovoltaic Cells for Space and Terrestrial Concentrator Applications," no. May 2014, pp. 525–529, 2005.

[9] K. M. Edmondson, D. C. Law, G. Glenn, A. Paredes, R. R. King, and N. H. Karam, "Flexible III-V multijunction solar blanket," *Conference Record of the 2006 IEEE 4th World Conference on Photovoltaic Energy Conversion, WCPEC-4*, vol. 2, no. June, pp. 1935–1938, 2007.

[10] S. Bailey and R. Raffaelle, “Space Solar Cells and Arrays,” in *Handbook of Photovoltaic Science and Engineering*, 1st ed., A. Luque and S. Hegedus, Eds. Wiley, 2003, ch. 10, pp. 413 – 446.

[11] G. Landis, “Review of solar cell temperature coefficients for space,” *Proceedings of the 13th Space Photovoltaic Research and Technology Conference*, no. 2, pp. 385–399, 1994. [Online]. Available: http://adsabs.harvard.edu/abs/1994sprt.nasa..385L

[12] D. C. Law, K. M. Edmondson, N. Siddiqi, A. Paredes, R. R. King, G. Glenn, E. Labios, M. H. Haddad, T. D. Isshiki, and N. H. Karam, “Lightweight, flexible, high-efficiency III-V multijunction cells,” *Conference Record of the 2006 IEEE 4th World Conference on Photovoltaic Energy Conversion, WCPEC-4*, vol. 2, pp. 1879–1882, 2007.

[13] R. R. King, D. Bhusari, D. Larrabee, X. Liu, E. Rehder, K. Edmondson, H. Cotal, R. K. Jones, J. H. Ermer, C. M. Fetzer, D. C. Law, and N. H. Karam, “Solar cell generations over 40% efficiency,” *Prog. Photovolt: Res. Appl.*, 2012.

[14] R. R. King, C. M. Fetzer, D. C. Law, K. M. Edmondson, H. Yoon, G. S. Kinsey, D. D. Krut, J. H. Ermer, P. Hebert, B. T. Cavicchi, and N. H. Karam, “Advanced III-V multijunction cells for space,” *Conference Record of the 2006 IEEE 4th World Conference on Photovoltaic Energy Conversion, WCPEC-4*, vol. 2, pp. 1757–1762, 2007.

[15] A. W. Bett, F. Dimroth, W. Guter, R. Hoheisel, E. Oliva, S. P. Philipps, J. Schöne, G. Siefer, M. Steiner, A. Wekkeli, E. Welser, M. Meusel, W. Köstler, G. Strobl, and F. Ise, “Highest efficiency multi-junction solar cell for terrestrial and space applications,” *24th European Photovoltaic Solar Energy Conference*, no. January, 2009.

[16] H. Cotal, C. Fetzer, J. Boisvert, G. Kinsey, R. King, P. Hebert, and H. Yoon, “III V multijunction solar cells for concentrating photovoltaics,” *Energy & Environmental Science*, no. December, 2008.

[17] M. Steiner, S. P. Philipps, M. Hermle, A. W. Bett, and F. Dimroth, “Validated front contact grid simulation for GaAs solar cells under concentrated sunlight,” *Prog. Photovolt: Res. Appl.*, vol. 19, no. May, pp. 73–83, 2011.

[18] I. Griffin, “Periodic Table source code example in LaTeX,” http://www.texample.net/tikz/examples/periodic-table-of-chemical-elements/.

[19] I. Institute, “GaInAs – Element specifics,” http://www.ioffe.ru/SVA/NSM/Semicond/GaInAs/.

[20] Yong-gang Zhang and Yi Gu, *Al(Ga)InP-GaAs Photodiodes Tailored for Specific Wavelength Range*, 1st ed. Intech Open, 2012, pp. 261 – 287. [Online]. Available: https://www.intechopen.com/books/photodiodes-from-fundamentals-to-applications/al-ga-inp-gaas-photodiodes-tailored-for-specific-wavelength-range

[21] A. C. Baptista, C. F. Fernandes, J. T. Pereira, and J. J. Paisana, *Fundamentos de Eletrónica*, 1st ed. Rua D. Estefânia, 183, r/c Dto. 1049-057 Lisboa, Portugal: LIDEL – edições técnicas, lda, 2012.

[22] J. L. Gray, "The Physics of the Solar Cell," in *Handbook of Photovoltaic Science and Engineering*, 1st ed., A. Luque and S. Hegedus, Eds. Wiley, 2003, ch. 3, pp. 62 – 111.

[23] M. Sotoodeh, A. H. Khalid, and A. A. Rezazadeh, "Empirical low-field mobility model for III-V compounds applicable in device simulation codes," *Journal of Applied Physics*, vol. 87, no. 6, pp. 2890–2900, 2000.

[24] P. Y. Yu and M. Cardona, *Fundamentals of Semiconductors – Physics and Materials Properties*, 4th ed. Springer, 2010.

[25] S. S. Li and W. R. Thurber, "The dopant density and temperature dependence of electron mobility and resistivity in n-type silicon," *Solid State Electronics*, vol. 20, pp. 609–616, 1977.

[26] PVEducation, "Absorption coefficients of varied semiconductor materials," http://www.pveducation.org/pvcdrom/pn-junctions/absorption-coefficient.

[27] NREL, "Data for the different sunlight spectra," https://www.nrel.gov/grid/solar-resource/spectra.html.

[28] K. . Zonen, "Information about the different wavelength ranges," https://www.kippzonen.com/Knowledge-Center/Theoretical-info/Solar-Radiation.

[29] Silvaco, *ATLAS User's Manual – Device Simulation Software*, 2nd ed. SILVACO International, 4701 Patrick Henry Drive, Bldg. 1, Santa Clara, CA 95054: SILVACO International, 2004, no. October.

[30] I. Institute, "Ioffe Institute's Database for semiconductors," http://www.ioffe.ru/SVA/.

[31] MatWeb, "MatWeb's Database for semiconductors," http://www.matweb.com/.

[32] S. Adachi, "III-V Ternary and Quaternary Compounds," *Springer Handbook of Electronic and Photonic Materials*, pp. 725–741, 2017.

[33] P. Sharma, "Modeling, optimization, and characterization of high concentration photovoltaic systems using multijunction solar cells," Ph.D. dissertation, School of Electrical Engineering and Computer Science, University of Ottawa, 2017.

[34] R. King, D. Law, K. Edmondson, C. Fetzer, G. Kinsey, Y. Hojun, D. Krut, J. Ermer, R. Sherif, and N. Karam, "Advances in high-efficiency iii-v multijunction solar cells," *Advances in OptoElectronics*, 12 2007.

[35] J. Dugas and J. Oualid, “Modelling of base doping concentration influence in polycrystalline silicon solar cells,” *Solar Cells*, vol. 20, no. 2, pp. 145–154, 1987.

[36] P. Vincent, G. C. Sergio, J. Jang, I. M. Kang, J. Park, H. Kim, M. Lee, and J. H. Bae, “Application of genetic algorithm for more efficient multi-layer thickness optimization in solar cells,” *Energies*, vol. 13, no. 7, pp. 1–13, 2020.

[37] G. Strobl, P. Uegele, R. Kern, K. Roy, C. Flores, R. Campesato, C. Signorini, and K. Bogus, “Development of advanced Si and GaAs solar cells for interplanetary missions,” in *14th Space Photovoltaic Research and Technology Conference (SPRAT 14)*, Oct. 1995, p. 6.

[38] B. Sciana, I. Zborowska-Lindert, D. Radziewicz, D. Pucicki, M. Panek, J. Jurenczyk, W. Dawidowski, M. Badura, and M. Tlaczala, “Tunnel junction technology for multijunction solar cell applications,” *ASDAM 2012 - Conference Proceedings: The 9th International Conference on Advanced Semiconductor Devices and Microsystems*, vol. 3, pp. 243–246, 2012.

CHAPTER 6

Appendix A

6.1 Semiconductor junctions

In this section, an overview of semiconductor junctions applied to solar cell production will be presented. The types of junctions that are pertinent for the completion of this work are the *p–n junctions* or *metal-semiconductor junctions* (also referred to as M–S junctions).

6.1.1 The p–n junction

The p–n junction is a widely known type o semiconductor junction, consisting of a block of a p-type semiconductor in contact with another block of an n-type.

When these two blocks are put in contact, both majority carriers from each side begin to move in the direction of the opposite side, by means of diffusion. This means that holes from the p-type move into the n-type block and, analogously, electrons move into the p-type. This transit of majority carriers translates in a diffusion current, I_{diff}, being created alongside the junction.

Consequently, as holes and electrons pass through the junction, they will recombine with the respective carriers on the other side and both particles will "disappear", ionizing the impurity atoms on each side; the donors will be positively charged whilst the acceptors will be negatively charged. The region where here the carriers recombine is given the name of *depletion region* (also known as *space charge region*), given that there is a great depletion of carriers in the area.

The depletion region is then characterized by a negatively charged zone in the p-type side and a positively charged zone in the n-type side. These two zones will create an electric field $\vec{E}$ near the junction. The direction of the electric field is contrary to the movement of carriers as a result of diffusion, leading the mobile charges on each side away from the junction. This transit of carriers ends up generating a

drift current of low intensity, I_{drift}, opposing the diffusion current.

These two processes counteract each other, diffusion tending to increase the depletion region while having the drift phenomenon resisting the expansion of the space charge. Over time, the drift current increases, while the diffusion current decreases, reaching equilibrium when both values are equal. When $I_{\text{diff}} = I_{\text{drift}}$, the flux of the mobile carriers is zero, since both processes negate each other.

When in this state of equilibrium, the Fermi levels of both materials will become uniform throughout the junction. For the p-type material, the Fermi level will lie just above the valence band, and for the n-type, just below the conduction band. The schematic of a p–n junction in equilibrium along with its energy band diagram are illustrated in Figure 6.1.

In the junction, a voltage differential V_0 is formed as a result of the charge difference between the two sides. This value depends on the material used, for Si is 0.7V and for Ge is 0.3V. For the junction to

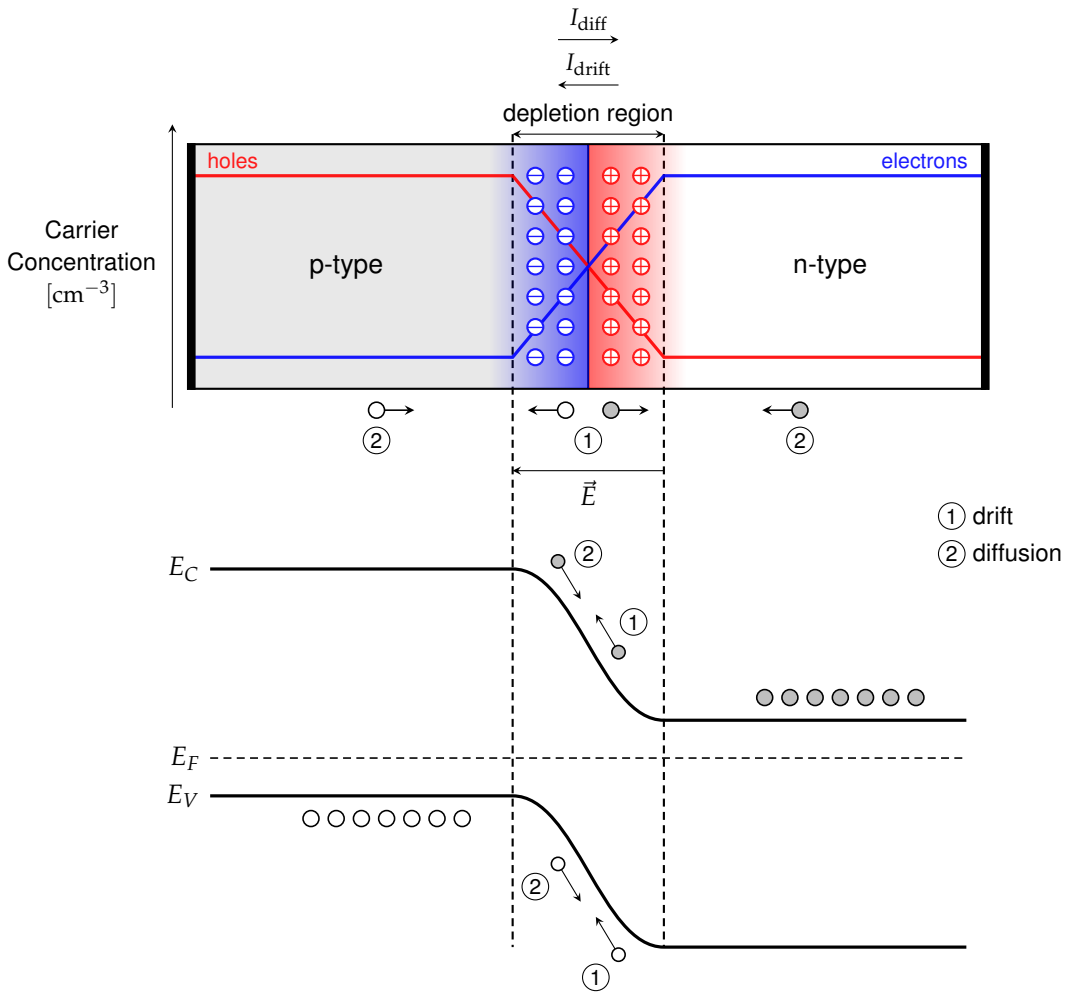

Figure 6.1: Schematic and energy band diagram of a p–n junction with zero applied bias voltage. Holes are represented in white, electrons in gray. Red zones are positively charged, blue zones are negatively charged. The concentration curves are merely indicative of concentration behavior in each zone.

conduct, this voltage differential must be overcome, and so an external voltage source is normally used.

6.1.1.A Forward biased

When an external voltage is applied to the junction, one says that it is biased. If the p-side is connected to the positive terminal and the n-side to the negative, one says that the junction is *forward biased*.

In this context, holes are being injected in the p-side and electrons in the n-side. This means that both sides are being supplied with majority carriers, that will diffuse towards the junction, nullifying the charge in the depletion region, hence reducing it. In this way, the barrier voltage V_0 will decrease, increasing the current by diffusion substantially I_{diff}. In equilibrium, the current will be given by $I = I_{\text{diff}} - I_{\text{drift}} \simeq I_{\text{diff}}$. The representation of the forward biased junction, along with its band diagram are represented in Figure 6.2.

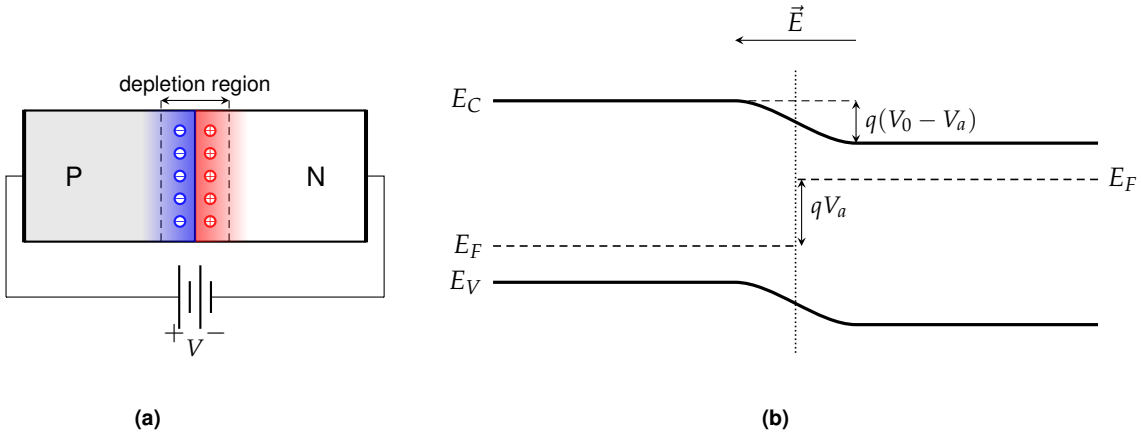

Figure 6.2: Representation of the forward biased p–n junction: (a) schematic representation, and (b) energy band diagram. Red zones are positively charged, blue zones are negatively charged.

6.1.1.B Reverse biased

There is also the opposite case when the p-side is connected to the negative terminal and the n-side to the positive terminal, meaning that the junction is *reverse biased*.

In this instance, holes will be attracted to the negative terminal, and electrons will be attracted to the positive terminal. This means that the source will attract majority carriers from both sides away from the junction, creating disequilibrium in charges in the depletion region and thus increasing it, making it difficult for the carriers to cross the junction. The barrier voltage V_0 will increase, reducing the diffusion current I_{diff}. At equilibrium, the current will be given by $I = I_{\text{diff}} - I_{\text{drift}} \simeq I_{\text{drift}}$. The representation of the reverse-biased junction, along with its energy band diagram are represented in Figure 6.6.

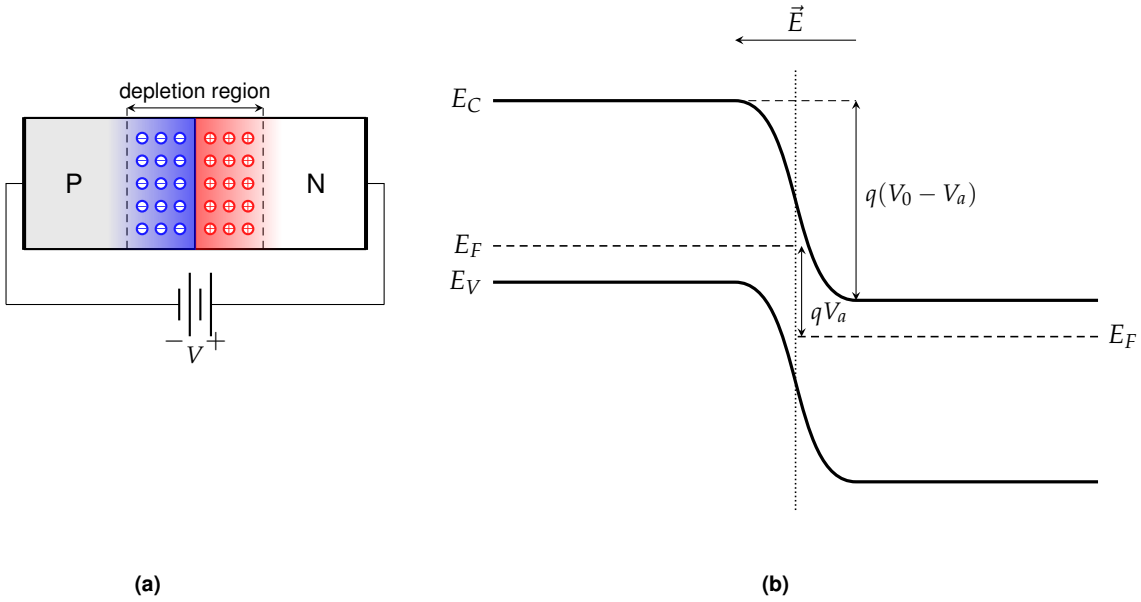

Figure 6.3: Representation of the reverse biased p–n junction: (a) schematic representation, and (b) energy band diagram. Red zones are positively charged, blue zones are negatively charged.

6.1.1.C The p–n diode

Adding an external source to both terminals of the p–n junction creates a semiconductor device capable of letting current pass or blocking it, commonly called as the *P–N Junction Diode*, represented in Figure 6.4. The diode lets current pass in one direction only and has a non-linear characteristic $I - V$ curve.

If the junction is forward biased, the current increases insignificantly up until it approaches the value of the barrier voltage V_0 (also called as "knee" voltage or threshold voltage, for Si: $V_0 = 0.7\text{V}$, and for Ge: $V_0 = 0.3\text{V}$). After this value, the current grows exponentially, and increasing the applied voltage beyond the threshold voltage may damage the device. The characteristic curve for the forward-biased diode is shown in Figure 6.5a.

In the case of the reverse-biased diode, the only current taken into consideration will be the drift current I_{drift}, which is in the order of magnitude of the nA, for a silicon diode. After what is called the *reverse breakdown voltage*, (for a Si diode the breakdown voltage may take values from 50V to hundreds of Volts) the reverse current will increase massively, destroying the device unless there is some kind of device limiting the current. The characteristic curve for the reverse-biased diode is shown in Figure 6.5b.

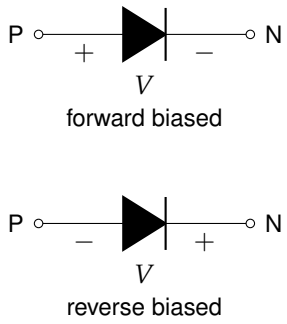

Figure 6.4: Schematics of the p–n junction diode.

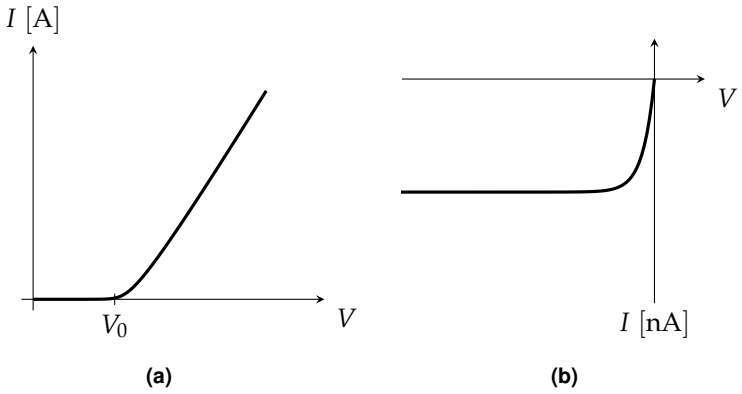

Figure 6.5: Characteristic $I - V$ curves for: (a) forward biased junction, and (b) reverse biased junction.

6.1.2 Tunnel junctions

The *tunnel junctions* (also denominated tunnel diodes) serve as interconnections between the p–n junctions that form a multi-junction cell. These junctions are quite necessary, since stacking p–n junctions on top of each other would mean the formation of p–n diodes between the subcells, creating a current blockage between subcells.

At the moment, III-V MJSCs are connected via Esaki interband tunnel diodes, which consist of a highly doped, narrow p–n junction junctions that are placed between two consecutive subcells. These interconnections need to fill several requirements: they need to possess a low electrical resistivity so they do not impact the solar cell's resistance, a high optical transmissivity coefficient (refer to Chapter 3.2, section 3.2.2 for a synopsis on optical properties) so photons can be transmitted to the subcells below and a peak tunneling current higher than the short-circuit current of the multi-junction solar cells (MJSCs).

Because of the high doping values, the Fermi level on both sides of the junction shifts; on the p-side, the E_F goes into the valence band E_V, and on the n-side, the E_F relocates into the conduction band E_C. In the event of a small positive bias voltage is applied to the junction, then full energy states on the n-side become aligned with empty states on the p-side, allowing charge carriers to move through the barrier as a result of the band-to-band tunneling effect. A band diagram of a p++/n++ GaAs tunnel junction is illustrated in Figure 6.6a.

In Figure 6.6b is shown the $I - V$ characteristic of a GaAs tunnel junction isolated from the cell, as can be consulted in the work of Sciana et al. [38]. For low voltages, the current rises as voltage increases, until it hits the peak, after that, the current decreases abruptly. This is due to the fact after the voltage at which the peak current is reached, let it be called V_{p}, the full states on the n-side and the empty states on the p-side are no longer aligned. From this point onwards, the tunnel junction behaves

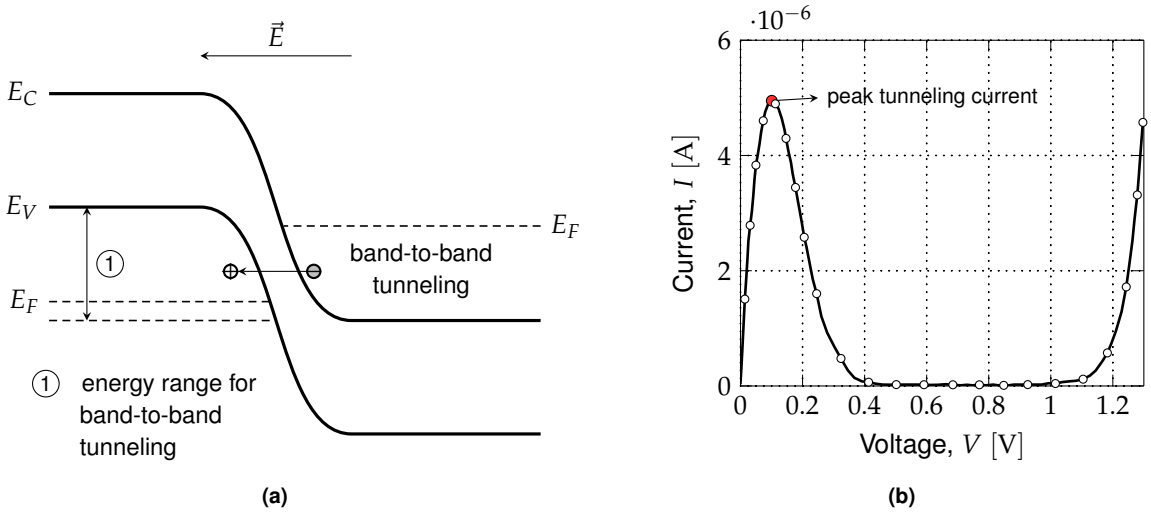

Figure 6.6: Tunnel junction representations: (a) energy band diagram of a tunnel diode, and (b) Simulated $I - V$ characteristic of a GaAs p++/n++ tunnel junction [38].

like a normal forward-biased p–n junction. The target operating scope of the tunnel diode is then from $0\mathrm{V}$ to V_p, when it hits the peak tunneling current. As it was already stated, peak tunneling current values are quite important when deciding on the tunnel junction for a MJSC, since they have to be suitably high to withstand the short-circuit current of the cell, particularly when designing concentrator solar cells.

CHAPTER 7

Appendix B

7.1 Silvaco ATLAS Source Code

The most important parts of the code used for simulating the cell in Silvaco ATLAS and obtaining its figures of merit are presented in this chapter.

In this section, an exemplary code for simulating the LM GaInP/GaInAs/Ge is presented. This part of the code has the purpose of extracting the major figures of merit of the cell, together with the $I-V$ curve. The complete code is provided, divided into sections for easy reading.

7.1.1 Assigning variables

Listing 7.1: ATLAS code: setting up the variables values.

```
# Master Thesis in Electrical and Computer Engineering
# Instituto Superior Tecnico, Lisbon
# "Characterization and Design of PV solar cells that absorb
    Ultraviolet, Visible and Infrared light"
# Author: Sara Bernardes, 79665
#       sarabernardes@tecnico.ulisboa.pt
# December, 2019

go atlas

set top_base_dop=5e16
set top_emit_dop=5e17

set width=1
set height=1
```

```
15
16 set top_bsfThick=0.12
17 set top_baseThick=0.7
18 set top_emitterThick=0.11
19 set top_fsfThick=0.03
20 set topcell=$top_fsfThick + $top_emitterThick + $top_baseThick +
     $top_bsfThick
21
22 set TJ1_emit=0.02
23 set TJ1_base=0.02
24 set TJ1_Thick=$TJ1_base+$TJ1_emit
25
26 set aux1=$topcell + $TJ1_emit + $TJ1_base
27
28 set mid_bsfThick=0.1
29 set mid_baseThick=4
30 set mid_emitterThick=0.08
31 set mid_fsfThick=0.03
32 set midcell=$mid_fsfThick + $mid_emitterThick + $mid_baseThick +
     $mid_bsfThick
33
34 set aux=$topcell + $TJ1_emit + $TJ1_base + $midcell
35
36 set TJ2_emit=0.05
37 set TJ2_base=0.05
38 set TJ2_Thick=$TJ2_base+$TJ2_emit
39
40 set aux2=$aux + $TJ2_emit + $TJ2_base
41
42 set bot_baseThick=170
43 set bot_emitterThick=0.1
44 set bot_fsfThick=0.02
45 set bot_bufferThick=0.2
46 set botcell=$bot_bufferThick + $bot_fsfThick + $bot_baseThick +
     $bot_emitterThick
47
48 # --- MESH VARIABLES --- #
49
50 set top_Lo=0
51 set top_fsf_Hi=$top_fsfThick
52 set top_emit_Hi=$top_fsf_Hi+$top_emitterThick
53 set top_base_Hi=$top_emit_Hi+$top_baseThick
54 set top_bsf_Hi=$top_base_Hi+$top_bsfThick
55
56 set TJ1_Lo=$top_bsf_Hi
57 set TJ1_Mid=$TJ1_Lo+$TJ1_Thick/2
58 set TJ1_Hi=$TJ1_Lo+$TJ1_Thick
59
```

```
set mid_Lo=$TJ1_Hi
set mid_fsf_Hi=$mid_Lo+$mid_fsfThick
set mid_emit_Hi=$mid_fsf_Hi+$mid_emitterThick
set mid_base_Hi=$mid_emit_Hi+$mid_baseThick
set mid_bsf_Hi=$mid_base_Hi+$mid_bsfThick

set TJ2_Lo=$mid_bsf_Hi
set TJ2_Mid=$TJ2_Lo+$TJ2_Thick/2
set TJ2_Hi=$TJ2_Lo+$TJ2_Thick

set bot_Lo=$TJ2_Hi
set bot_buf_Hi=$bot_Lo+$bot_bufferThick
set bot_fsf_Hi=$bot_buf_Hi+$bot_fsfThick
set bot_emit_Hi=$bot_fsf_Hi+$bot_emitterThick
set bot_base_Hi=$bot_emit_Hi+$bot_baseThick

set nrdiv=20
set grid_w=0.15
set grid_h=0.4
```

7.1.2 Mesh definition

Listing 7.2: ATLAS code: defining the mesh for the all the regions of the cell.

```
# --- MESH DEFINITION --- #

mesh width=$height

x.m loc=0.0     s=$width/4
x.m loc=$width/2  s=$width/10
x.m loc=$width    s=$width/4

# TOP SUBCELL

# Grid
y.mesh loc=-$grid_h   spac=0.0003
y.mesh loc=0      spac=$grid_h/$nrdiv
# FSF
y.mesh loc=$top_fsf_Hi    spac=$top_fsfThick/$nrdiv
# Emitter
y.mesh loc=$top_emit_Hi   spac=$top_emitterThick/$nrdiv
# Base
y.mesh loc=$top_base_Hi   spac=$top_baseThick/$nrdiv
# BSF
y.mesh loc=$top_bsf_Hi    spac=$top_bsfThick/($nrdiv+10)
```

```
22
23 # TUNNEL JUNCTION 1
24
25 # Tunnel Emitter
26 y.mesh loc=$TJ1_Mid     spac=$TJ1_emit/100
27 # Tunnel Base
28 y.mesh loc=$TJ1_Hi    spac=$TJ1_base/100
29
30 # MIDDLE SUBCELL
31
32 # FSF
33 y.mesh loc=$mid_fsf_Hi    spac=$mid_fsfThick/($nrdiv+10)
34 # Emitter
35 y.mesh loc=$mid_emit_Hi    spac=$mid_emitterThick/$nrdiv
36 # Base
37 y.mesh loc=$mid_base_Hi    spac=$mid_baseThick/($nrdiv)
38 # BSF
39 y.mesh loc=$mid_bsf_Hi    spac=$mid_bsfThick/($nrdiv+10)
40
41 # TUNNEL JUNCTION 2
42
43 # Tunnel Emitter
44 y.mesh loc=$TJ2_Mid     spac=$TJ2_emit/100
45 # Tunnel Base
46 y.mesh loc=$TJ2_Hi    spac=$TJ2_base/100
47
48 # BOTTOM SUBCELL
49
50 # Window
51 y.mesh loc=$bot_buf_Hi    spac=$bot_bufferThick/($nrdiv+10)
52 # Emitter
53 y.mesh loc=$bot_fsf_Hi    spac=$bot_fsfThick/($nrdiv)
54 # Base
55 y.mesh loc=$bot_emit_Hi    spac=$bot_emitterThick/($nrdiv)
56 # BSF
57 y.mesh loc=$bot_base_Hi    spac=$bot_baseThick/($nrdiv)
```

7.1.3 Region, Electrode and Contact definition

Listing 7.3: ATLAS code: region, electrode and contacts definition.

```
1 # --- REGIONS DEFINITION--- #
2
3 region num=1 material=Vacuum  x.min=0 x.max=$width/2-$grid_w/2  y.min
    =-$grid_h y.max=0
```

```
region num=2 material=GaAs  x.min=$width/2-$grid_w/2 x.max=$width/2+$grid_w/2   y.min=-$grid_h y.max=0
region num=3 material=Vacuum  x.min=$width/2+$grid_w/2 x.max=$width  y.min=-$grid_h  y.max=0

region num=4 material=AlInP   x.min=0 x.max=$width  y.min=$top_Lo  y.max=$top_fsf_Hi   x.comp=0.5
region num=5 material=InGaP   x.min=0 x.max=$width  y.min=$top_fsf_Hi  y.max=$top_emit_Hi  x.comp=0.5
region num=6 material=InGaP   x.min=0 x.max=$width  y.min=$top_emit_Hi  y.max=$top_base_Hi  x.comp=0.5
region num=7 material=InAlGaP   x.min=0 x.max=$width  y.min=$top_base_Hi  y.max=$top_bsf_Hi

region num=8 material=AlGaAs  x.min=0  x.max=$width   y.min=$TJ1_Lo  y.max=$TJ1_Mid  x.comp=0.54
region num=9 material=AlGaAs    x.min=0  x.max=$width   y.min=$TJ1_Mid  y.max=$TJ1_Hi   x.comp=0.54

region num=10 material=InGaP  x.min=0 x.max=$width  y.min=$mid_Lo  y.max=$mid_fsf_Hi  x.comp=0.5
region num=11 material=InGaAs   x.min=0 x.max=$width  y.min=$mid_fsf_Hi  y.max=$mid_emit_Hi   x.comp=0.01
region num=12 material=InGaAs   x.min=0 x.max=$width  y.min=$mid_emit_Hi y.max=$mid_base_Hi   x.comp=0.01
region num=13 material=InGaP    x.min=0 x.max=$width  y.min=$mid_base_Hi y.max=$mid_bsf_Hi  x.comp=0.5

region num=14 material=AlGaAs x.min=0  x.max=$width   y.min=$TJ2_Lo  y.max=$TJ2_Mid  x.comp=0.54
region num=15 material=GaAs   x.min=0  x.max=$width   y.min=$TJ2_Mid  y.max=$TJ2_Hi

region num=16 material=InGaAs x.min=0 x.max=$width  y.min=$bot_Lo  y.max=$bot_buf_Hi x.comp=0.01
region num=17 material=InGaP  x.min=0 x.max=$width  y.min=$bot_buf_Hi  y.max=$bot_fsf_Hi x.comp=0.5
region num=18 material=Germanium x.min=0 x.max=$width   y.min=$bot_fsf_Hi  y.max=$bot_emit_Hi
region num=19 material=Germanium x.min=0 x.max=$width   y.min=$bot_emit_Hi y.max=$bot_base_Hi

electrode num=1 name=cathode x.min=$width/2-$grid_w/2 x.max=$width/2+$grid_w/2

#electrode num=2 name=grid material=GaAs x.min=$width/2-$grid_w/2 x.max=$width/2+$grid_w/2 y.min=-$grid_h y.max=0

```

```
electrode num=2 name=TJ1_top material=AlGaAs  y.min=$topcell   y.max=
    $topcell + $TJ1_emit
electrode num=3 name=TJ1_bot material=AlGaAs  y.min=$topcell +
    $TJ1_emit  y.max=$topcell + $TJ1_emit + $TJ1_base

electrode num=4 name=TJ2_top material=AlGaAs  y.min=$aux  y.max=$aux
    + $TJ2_emit
electrode num=5 name=TJ2_bot material=GaAs  y.min=$aux + $TJ2_emit
    y.max=$aux + $TJ2_emit +$TJ2_base

electrode num=6 name=anode bottom

contact name=TJ1_top  resistance=1e9
contact name=TJ1_bot  resistance=1e9
contact name=TJ2_top  resistance=1e9
contact name=TJ2_bot  resistance=1e9
```

7.1.4 Doping definition

Listing 7.4: ATLAS code: assigning doping values for each region.

```
# --- DOPING DEFINITION --- #

# Metal grid
doping uniform region=2 n.type conc=1e20

# GaInP subcell
doping uniform region=4 n.type conc=1e19
doping uniform region=5 n.type conc=$top_emit_dop
doping uniform region=6 p.type conc=$top_base_dop
doping uniform region=7 p.type conc=5e18

# Tunnel junction 1
doping uniform region=8 p.type conc=6e20
doping uniform region=9 n.type conc=3e20

# GaInAs subcell
doping uniform region=10 n.type conc=5e19
doping uniform region=11 n.type conc=1e17
doping uniform region=12 p.type conc=1e17
doping uniform region=13 p.type conc=1e19

# Tunnel junction 2
doping uniform region=14 p.type conc=4e20
doping uniform region=15 n.type conc=1e20
```

```
25
26 # Ge subcell
27 doping uniform region=16 n.type conc=2e18
28 doping uniform region=17 n.type conc=5e19
29 doping uniform region=18 n.type conc=1e19
30 doping uniform region=19 p.type conc=2e17
```

7.1.5 Material properties definition

Listing 7.5: ATLAS code: material properties, presented and calculated in 4.2.

```
1 # --- MATERIALS --- #
2 # Refractive indexes
3 material material=Vacuum  real.index=3.3 imag.index=0
4
5 material material=InGaP   index.file=GaInP.nk
6 material material=InAlGaP   index.file=GaInP.nk
7 material material=AlInP   sopra=Againp10.nk
8 material material=Germanium   sopra=Ge.nk
9 material material=InGaAs  sopra=Ringas0.nk
10 material material=AlGaAs      sopra=Algaas5.nk
11 material material=GaAs        sopra=Gaas.nk
12
13 # Ge
14 material material=Ge ALATTICE=5.658 EG300=0.661 PERMITTIVITY=16.2
     AFFINITY=4
15 material material=Ge MUN=3900 MUP=1800
16 material material=Ge NC300=1.0e19 NV300=5e18
17 material material=Ge TAUN=1E-3 TAUP=1E-3 AUGN=1e-30 AUGP=1e-30 COPT=6
     .41E-14
18
19 # GaAs
20 material material=GaAs ALATTICE=5.653 EG300=1.424 AFFINITY=4.07
     PERMITTIVITY=12.9
21 material material=GaAs MUN=8500 MUP=400
22 material material=GaAs NC300=4.7e17 NV300=9e18
23 material material=GaAs TAUN=5E-9 TAUP=3E-6 AUGN=1e-30 AUGP=1e-30 COPT
     =7.2E-10
24
25 # InGaAs
26 material material=InGaAs ALATTICE=5.658 EG300=1.41 AFFINITY=4.0783
     PERMITTIVITY=12.9154
27 material material=InGaAs MUN=8328 MUP=400
28 material material=InGaAs NC300=1.66E19 NV300=1.78E19
29
```

```
30 # InGaP
31 material material=InGaP ALATTICE=5.658 EG300=1.89 AFFINITY=4.09
       PERMITTIVITY=11.8
32 material material=InGaP MUN=1945 MUP=141
33 material material=InGaP NC300=1.66e19 NV300=1.78e19
34
35 # AlInP
36 material material=AlInP ALATTICE=5.658 EG300=2.53 AFFINITY=4.2
       PERMITTIVITY=11.7
37 material material=AlInP NC300=1.08e20 NV300=1.28e19
38
39 # InAlGaP
40 material material=InAlGaP ALATTICE=5.653 EG300=2.1744 PERMITTIVITY=12
       .16 AFFINITY=4.26
41 material material=InAlGaP NC300=9.13e17 NV300=7.81E18
42
43 # AlGaAs
44 material material=AlGaAs  ALATTICE=5.658 EG300=2.0 PERMITTIVITY=11
       .3664 AFFINITY=3.5644
45 material material=AlGaAs MUN=161.448 MUP=61.984
46 material material=AlGaAs NC300=1.71e19 NV300=1.3E19
```

7.1.6 Models, Beam, Solve and Extract statements

Listing 7.6: ATLAS code: obtaining the $I-V$ curve and extracting parameters.

```
1 models srh auger optr ni.fermi fermi bgn conmob trap.tunnel bbt.kl
2
3 beam num=1 y.o=-3 angle=90 wavel.start=0.1 wavel.end=3 wavel.num=500
       AM0
4
5 solve init
6 solve b1=1e-01
7 solve b1=1
8
9 log outf=IV_solarcell.log
10
11 solve vanode=0
12 solve vanode=0.5
13 solve vanode=1
14 solve vanode=1.5
15 solve vanode=2
16 solve name=anode vstep=0.01 vfinal=2.7
17
18 extract init infile="IV_solarcell.log"
```

```
19 extract name="JV" curve(v."anode", i."cathode") outfile="
     IV_solarcell.dat"
20 extract name="Jsc" y.val from curve(v."anode", i."cathode") where
     x.val=0.0
21 extract name="Jsc_mA_cm2" $"Jsc"*1e11/($height*$width)
22 extract name="Voc" x.val from curve(v."anode", i."cathode") where
     y.val=0.0
23 extract name="Pm" max(curve(v."anode", (v."anode" * i."cathode")))
24 extract name="Pm_cm2" $"Pm"*1e8/($height*$width)
25 extract name="Vm" x.val from curve(v."anode", (v."anode"*i."cathode")
     ) where y.val=$"Pm"
26 extract name="Im" $"Pm" / $"Vm"
27 extract name="FF" ($"Pm" / ($"Jsc"*$"Voc" ))*100
28 extract name="Opt_int" max(beam."1")
29 extract name="Eff" ($Pm_cm2 / $Opt_int)*100
30
31 quit
```